

**MASS TRANSFER IN BACK TO BACK ELBOWS  
ARRANGED IN AN OUT OF PLANE  
CONFIGURATION UNDER SINGLE &  
ANNULAR TWO-PHASE FLOW CONDITIONS**

MASS TRANSFER IN BACK TO BACK ELBOWS  
ARRANGED IN AN OUT OF PLANE CONFIGURATION  
UNDER SINGLE & ANNULAR TWO-PHASE FLOW  
CONDITIONS

By

THUAN LE, B.ENG.

B. Eng. (McMaster University, Ontario, Canada)

A Thesis

Submitted to the School of Graduate Studies

In Partial Fulfillment of the Requirements

For the Degree

Master of Applied Science

McMaster University

© Copyright by Thuan Le, September 2013

Master of Applied Science (2013)

McMaster University

(Mechanical Engineering)

Hamilton, Ontario

TITLE: Mass Transfer in Back to Back Elbows arranged in an Out of Plane Configuration under Single & Annular Two-Phase Flow Conditions

AUTHOR: Thuan Le, B.Eng. (McMaster University)

SUPERVISOR(S): Professor Chan. Y. Ching,

NUMBER OF PAGES: xiv, 111

# Abstract

Flow-Accelerated Corrosion (FAC) is a pipe wall thinning mechanism affecting carbon steel piping systems in power generation plants. Mass transfer is the rate limiting factor, even though chemistry and materials determine the overall potential for FAC. Different localized thinning rates in back to back elbow configurations between the first and second elbow have been noted at nuclear power plants, and this difference depends on the length of pipe between the elbows, flow conditions, and the configuration of the back to back elbows (e.g. S, C, or out of plane). In this thesis, mass transfer measurements in back to back elbows arranged in an out of plane configuration under single and annular two-phase flow conditions are presented.

The mass transfer measurements were performed using a wall dissolving technique with bend sections cast from gypsum. The diffusivity of gypsum in water is similar to the diffusivity of iron from the magnetite layer of carbon steel pipe in water, thus providing analogous mass transfer conditions to FAC in power generation plants. The wall dissolution of gypsum allows the surface roughness to develop due to the flow. The mass transfer is determined by passing water through the gypsum test sections in a flow loop system. The test sections are then sectioned into two halves to expose the worn surface. The surface topology is measured using a three dimensional laser scanner. The wear progression of the surface with time provides local mass transfer rates, locations of high mass transfer and local surface roughness.

The single-phase flow experiments were performed at a Reynolds number of 70,000 for different lengths of pipe (0, 1, 2 and 5 pipe diameters) between the elbows. The mass transfer results show regions of higher mass transfer in the second elbow in comparison to the first elbow. The maximum mass transfer rate in the second elbow decreases when the length of the pipe between the elbows was increased from 0 to 5 pipe diameters. Surface features corresponding to flow streaks on the second elbow surface indicated swirling flow, and its strength decreases with increasing separation distance between the elbows. The surface roughness was found to be higher in the regions of high mass transfer and decreases with increasing elbow separation distance.

The effect of air and water superficial velocities on the mass transfer for the bends with a separation distance of 0 pipe diameters was measured under two-phase air-water annular flow. In addition, the effect of separation distance of 0, 1 and 5 pipe diameters in length between the elbows was studied for one annular flow condition. The highest mass transfer was found on the outer wall of the first elbow for all cases. The maximum mass transfer in the second elbow was found to be approximately 60 percent of the maximum value in the first elbow, and was not affected significantly when the elbow separation distance was increased from 0 to 1 and 5 pipe diameters. The separation distance between the elbows did not affect the maximum mass transfer on the outer wall of the first elbow. The mass transfer increased with an increase in either the water or air superficial velocity, with the air velocity having a greater effect. The mass transfer enhancement factor relative to that in a straight pipe only increases significantly with increasing air superficial

velocity. The roughness development in the pipe was modest, but increases significantly in the high mass transfer region of the first and second elbow.

# Acknowledgements

I would like to express my appreciation to my supervisor Dr. Chan. Y. Ching for giving me the opportunity to work with him in this project. Dr. Ching's enthusiasm and motivation has been tremendous during my time at McMaster University. I was motivated and encouraged to perform at my best and sometimes beyond. Without Dr. Ching's support, motivation and guidance, the completion of this work might not be possible. Dr. Ching is not only a supervisor, a mentor but is truly a great friend. His attitude and personality creates a friendly and exciting learning/working environment at the Thermal Management Research Laboratory (TMRL).

I would also like to thank Dr. Ewing for his advice and guidance throughout the project. His valuable advices have accelerated the data analysis and other aspects of the project. I admire Dr. Ewing for his dedication, enthusiasm and high expectations in research. His discussions are always helpful and inspired deeper thoughts than what I initially had in mind and I am grateful for that.

I would also like to thank Dr. Cotton and members of the TMRL group for their constructive comments during our weekly meetings. The help from the mechanical engineering department technicians with machining and sectioning of test sections is greatly appreciated. Lastly, I would like to thank my grandma, mother and family for the support and encouragement in everything I do.

# Table of Contents

<b>Abstract.....</b>	<b>ii</b>
<b>Acknowledgements .....</b>	<b>v</b>
<b>List of Tables .....</b>	<b>viii</b>
<b>List of Figures.....</b>	<b>ix</b>
<b>Nomenclature .....</b>	<b>xiii</b>
<b>Chapter 1 Introduction.....</b>	<b>1</b>
1.1 Introduction .....	1
1.2 Sequence of Chapters .....	9
<b>Chapter 2 Literature Review .....</b>	<b>11</b>
2.1 Single-phase Flow .....	15
2.2 Two-phase Flow .....	22
<b>Chapter 3 Experimental Facility .....</b>	<b>28</b>
3.1 Experimental Facility .....	28
3.2 Experimental Methodology.....	30
3.3 Data Reduction .....	37
3.4 Uncertainty analysis .....	50
3.5 Mass Transfer Erosion Test.....	51

<b>Chapter 4 Results and Discussion .....</b>	<b>55</b>
4.1 Single-phase Flow Results .....	55
4.2 Two-phase Flow Results .....	65
<b>Chapter 5 Conclusions and Recommendations.....</b>	<b>80</b>
5.1 Conclusions .....	80
5.2 Recommendations .....	83
<b>List of References.....</b>	<b>85</b>
<b>Appendix.....</b>	<b>91</b>

# List of Tables

Table 3.1: Single-phase flow test matrix for $Re = 70,000$ , $Sc = 1280$ .....	34
Table 3.2: Annular two-phase flow test matrix.....	35
Table 4.1: Relative roughness level in the different regions for all elbow separation distances .....	65
Table 4.2: Comparison of fully developed pipe mass transfer to heat transfer correlations for different annular two-phase flow conditions.....	76
Table 4.3: Relative roughness of different location for the different annular two-phase flow conditions.....	79

# List of Figures

Figure 1.1: Typical worn surface characteristic of carbon steel pipe under single-phase flow [Dooley, 2008].....	3
Figure 1.2: ‘Tiger striped’ surface characteristic of carbon steel pipe under two-phase flow [Thebault et al., 2008].....	4
Figure 2.1: Schematic of the mechanism of flow accelerated corrosion [Dooley, 2008]..	12
Figure 2.2: Dimensionless mass transfer coefficient for different roughness height [Dawson and Trass, 1972] .....	17
Figure 2.3: velocity profile in the second elbow of the out of plane configuration [Yuki et al., 2011] .....	21
Figure 2.4: Effect of superficial gas and liquid velocities on maximum mass transfer coefficients (K) and enhancement at bends in two phase flow [Poulson, 1993] .....	23
Figure 2.5: Effect of water superficial velocity on the Sherwood number distribution in a 90 degree bend for $V_G = 30.2$ m/s, $V_L = 0.18, 0.29$ and $0.41$ m/s [Mazhar et al., 2013] ....	24
Figure 2.6: Schematic diagram of two-phase flow structure in a bend [Maddock et al., 1974] .....	27
Figure 3.1: Schematic layout of all components in the experimental facility.....	29
Figure 3.2: Schematic of casting mold for the out of plane configuration with different elbow separation distances.....	31
Figure 3.3: (a) out of plane mould with straight pipe core inserted (b) out of plane configuration test section .....	32

Figure 3.4: Typical test sections drying time measured by weight for $L/D = 0$ configuration .....	33
Figure 3.5: (a) scanned image (b) final pipe surface .....	36
Figure 3.6: Algorithm for the alignment process of worn sections .....	39
Figure 3.7: Radius profiles of the upstream pipe of an unworn section at different streamwise $z/D$ locations from the pipe entrance .....	40
Figure 3.8: Offset of the coordinate system based on axisymmetric flow in the upstream pipe (a) $x$ shift, $y$ rotation (b) $y$ shift, $x$ rotation .....	40
Figure 3.9: Two dimensional schematic diagram of volume of a grid cell for (a) straight pipe (b) extrados half of a bend .....	43
Figure 3.10: Typical concentration difference ( $\circ$ ) and water temperature ( $\square$ ) of the system during the experiment .....	45
Figure 3.11: Typical local mass transfer removed at different streamwise location for $\theta$ at 90 degree of the $L/D = 0$ configuration.....	46
Figure 3.12: Comparison of the overall mass removed of the laser scanner measurement data reduction (filled symbols) and the weight measurement before and after test (open symbols) to the conductivity increase in the system. $\blacksquare L/D = 0$ , $\bullet L/D = 1$ , $\blacktriangle L/D = 2$ and $\blacklozenge L/D = 5$ .....	49
Figure 3.13: Calibration data of mass of gypsum removed and electrical conductivity.....	50
Figure 3.14: Concentration difference of wall and the bulk water flow for $\blacktriangle 0$ g/l and $\bullet 1.2$ g/l initial bulk concentration. $V_L = 0.31$ m/s and $V_G = 28.82$ m/s .....	53

Figure 3.15: Maximum Sherwood number in the first elbow outer wall for: – 1.2g/l - - 0 g/l at different angles along the bend (black:  $\Phi = 40^\circ$  and blue:  $\Phi = 45^\circ$ ) .....53

Figure 4.1: Distribution of the Sherwood number on (a) outer wall region and (b) inner wall region for  $90^\circ$  out of plane configuration with separation distances  $L/D = 0, 1, 2$  and  $5$  between the elbows for  $Re = 70,000$  and  $Sc = 1280$  .....56

Figure 4.2: Typical azimuthal Sherwood number profiles in the upstream pipe for  $Re = 70,000$  and  $Sc = 1280$ . +  $z/D = -1$ , -  $z/D = -4$ , red  $L/D = 0$ , green  $L/D = 1$ , black  $L/D = 2$ , magenta  $L/D = 5$ .....58

Figure 4.3 Azimuthal Sherwood number profiles along the second elbow curvature for (a)  $L/D = 0$  (b)  $L/D = 1$  (c)  $L/D = 2$  (d)  $L/D = 5$  at  $Re = 70,000$  and  $Sc = 1280$ .....61

Figure 4.4: Maximum enhancement factor in the elbow relative to the upstream pipe Sherwood number for different elbow separation distances. o Region III, □ highest region downstream of first elbow .....62

Figure 4.5: Typical surface topology of the second elbow for (a)  $L/D = 0$ , time = 80 minutes (b)  $L/D = 5$ , time = 80 minutes.....64

Figure 4.6: Typical relative roughness level of the second elbow inner side wall for (a)  $L/D = 0$ , time = 80 minutes (b)  $L/D = 5$ , time = 80 minutes.....64

Figure 4.7: Effect of (a) water superficial velocity (b) air superficial velocity on the Sherwood number distribution.....66

Figure 4.8: Azimuthal profiles of Sherwood number along the first and second elbow for increasing water superficial velocity: -  $V_L = 0.19$  m/s,  $V_G = 29.71$  m/s; --  $V_L = 0.31$  m/s,  $V_G = 28.82$  m/s; ...  $V_L = 0.44$  m/s,  $V_G = 27.96$  m/s.....67

Figure 4.9: Azimuthal Sherwood number profile along the first and second elbow for increasing gas superficial velocity: -  $V_L = 0.31\text{m/s}$ ,  $V_G = 21.58\text{ m/s}$ ; --  $V_L = 0.31\text{m/s}$ ,  $V_G = 23.88\text{ m/s}$ ; ...  $V_L = 0.31\text{ m/s}$ ,  $V_G = 28.82\text{ m/s}$  .....68

Figure 4.10: Effect of water and air superficial velocities on the mass transfer enhancement factor at (a) the line of sight in first elbow, (b) narrow peak in first elbow and (c) second elbow for separation distance  $L/D = 0$ .....72

Figure 4.11: Effect of elbow separation distance  $L/D$  on the Sherwood number distribution .....74

Figure 4.12: Azimuthal profiles of Sherwood number along the first and second elbow at  $V_L = 0.31\text{ m/s}$ ,  $V_G = 28.82\text{ m/s}$  for elbow separation distance  $L/D$  of - 0; -- 1; ... 5 ( $z/D$  is the distance downstream of exit of first elbow).....75

Figure 4.13: Typical surface relative roughness of (a) upstream pipe (b) first elbow outer wall.....78

# Nomenclature

$A$	Instantaneous local surface area [m <sup>2</sup> ]
$C$	Concentration [g/l]
$d$	Gypsum diffusivity in water at 25° C [m <sup>2</sup> /s]
$D$	Pipe inner diameter [m]
$e$	Roughness height [m]
$e/D$	Relative roughness
$e^+$	Relative roughness scale
$h$	Mass transfer coefficient [m/s]
$L/D$	Dimensionless elbows separation distance
$m$	Mass removed [kg]
$Pr$	Prandtl number
$r$	Pipe radius [m]
$R_c$	Elbow radius of curvature
$Re$	Reynolds number
$Sc$	Schmidt number
$Sh$	Sherwood number
$t$	Experimental time [s]
$u^*$	Friction velocity [m/s]
$V$	Superficial velocity [m/s]
$z/D$	Dimensionless streamwise distance

### **Symbols**

$\Phi$	Curvature angle along elbow [degree]
$\rho$	Gypsum density [kg/m <sup>3</sup> ]
$\nu$	Kinematic viscosity [m <sup>2</sup> /s]
$\theta$	Pipe circumferential angle [degree]
$\delta$	Local instantaneous pipe surface wear [mm]
$\forall$	Volume [m <sup>3</sup> ]
$\tau$	Modified time [s]
$\Delta$	Difference

### **Subscripts**

$1$	first elbow
$2$	second elbow
$b$	Bulk flow
$o$	Initial
$w$	Wall
$G$	Air
$L$	water

# Chapter 1 Introduction

## 1.1 Introduction

Flow accelerated corrosion (FAC) is a pipe wall thinning mechanism affecting carbon steel piping systems of power generation plants. FAC occurs in both single and two-phase flow of water and steam-water due to the dissolution of iron from the magnetite layer of the piping into the bulk flowing fluid. The development of FAC is basically a three stage process: (1) electrochemical oxidation reactions at the metal-oxide interface to form ferrous ions, (2) diffusional mass transfer of the ferrous ions and dissolution of the oxide layer, (3) convective mass transfer of the ferrous ions into the bulk flowing fluid. While FAC depends on many factors such as water chemistry, pH level, flow velocity, temperature, and material composition of the pipe, the rate limiting factor is mass transfer to the flow. The mass transfer is affected by local turbulence, surface roughness, piping geometry and also flow regime, void fraction, slip ratio, and droplet size in two-phase flow applications. Abrupt changes in the flow can result in high turbulence levels and significantly increase the mass transfer rates, such as in flow downstream of orifices, T junctions and bend components [Dooley, 2008], with potential for abrupt failure of the piping system.

The importance of FAC has continued to grow in the past 30 years, particularly in the power generation and oil and gas industries. The potential of piping rupture in older power generation plants poses strong risk to operation. Abrupt failure due to FAC is expensive and unfortunately has led to fatalities on several occasions. A pipeline outage can take several days to repair, costing up to millions of dollar. Several fatalities have been reported at nuclear power plants in the United States and Japan due to FAC. These include the incidents at Surry (1986), Pleasant Prairie (1995), Mihama (2004), and Iatan (2007). A pipe rupture downstream of an orifice plate due to FAC at Mihama nuclear power plant caused five deaths and several injuries, while a rupture in a 90 degree elbow at Surry nuclear power plant resulted in several fatalities. Thus, the need to understand and mitigate FAC is essential to the reliable operation of power generation plants.

The appearance of FAC on the pipe surface is rather distinctive. FAC in single-phase flow results in a worn pipe surface that can be described as having an ‘orange peel’ appearance [Dooley, 2008; Thebault et al., 2008]. The surface is characterized by horseshoes like pits that are oriented in the direction of the flow as seen in Figure 1.1 [Dooley, 2008]. The FAC surface is much different from the surface where wall thinning is less as shown in the lower right corner of Figure 1.1a. A similar wear pattern under a different operation condition is shown in Figure 1.1b implying consistency in the surface scallops that are characteristic of FAC in single-phase flows.

FAC is enhanced significantly in two-phase flows in comparison to single-phase flow. The impingement of high velocity liquid droplets carried in the steam vapor core on the pipe surface can significantly affect FAC rates [Brunton and Rochester, 1979;

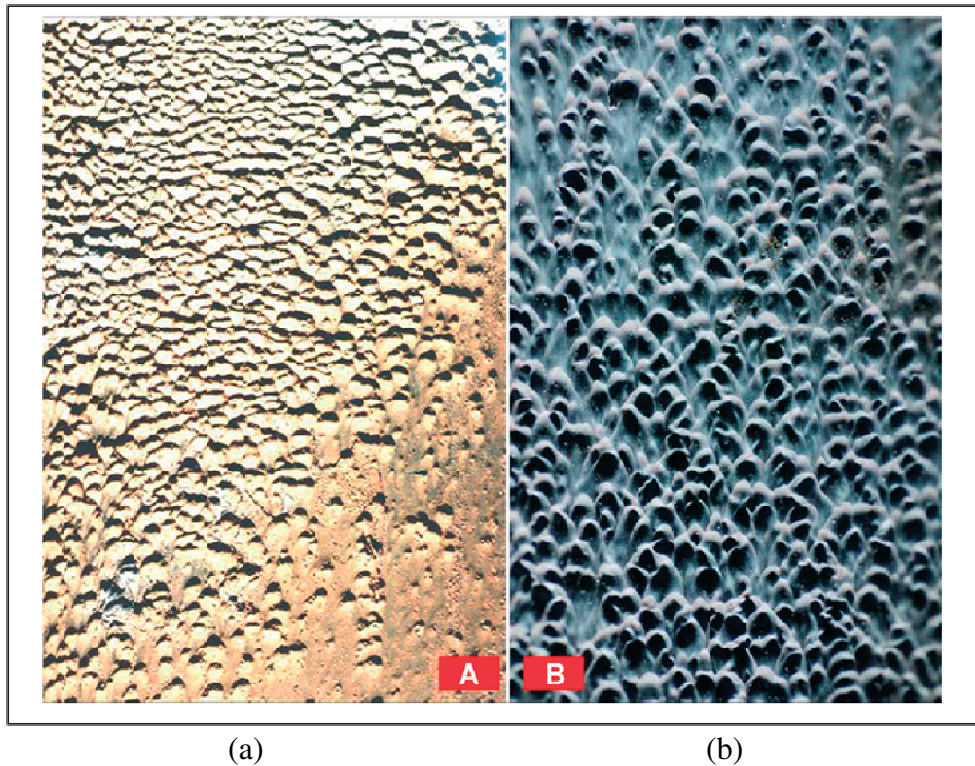


Figure 1.1: Typical worn surface characteristic of carbon steel pipe under single-phase flow [Dooley, 2008]

Heymann, 1969]. Liquid droplet impingement is of primary concern in piping geometry such as bends, since droplets often do not follow the curvature path of the elbow. The mass transfer occurs only in the liquid phase because ferrous ions are not soluble in steam. The worn pipe surface in two-phase flow is more diverse and can resemble: (1) the ‘orange peel’ appearance of single-phase FAC, (2) ‘tiger stripe’ pattern shown in Figure 1.2, and (3) smooth, polished black shiny surface. The piping surface due to FAC under two phase flows appears blackish possibly due to the removal of oxygen in the water to the steam phase, thus reducing the oxidizing capabilities of the water phase.

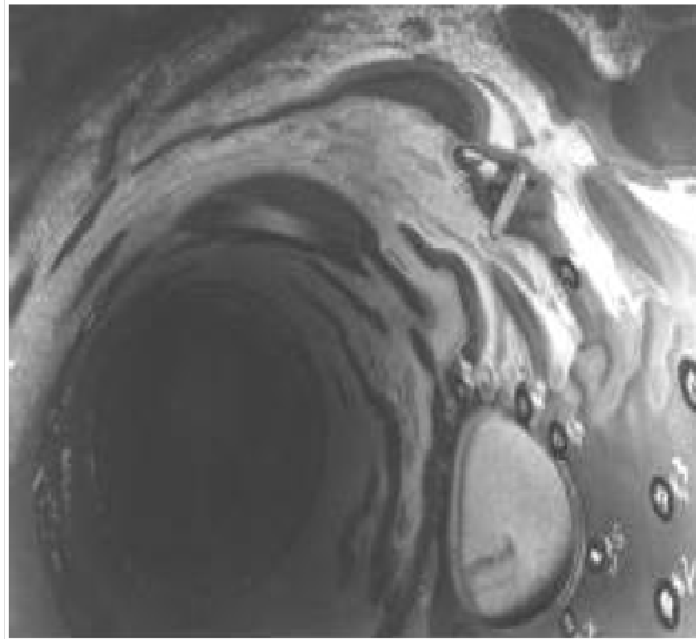


Figure 1.2: 'Tiger striped' surface characteristic of carbon steel pipe under two-phase flow [Thebault et al., 2008]

The development of surface scallops in single-phase flow as a result of FAC can increase the mass transfer rate significantly [Poulson and Robinson, 1988; Poulson, 2007]. The initial pipe surface is typically smooth and the development of scallops over time increases the surface roughness. The effect of roughness on the mass transfer has been investigated using predefined roughness patterns such as V-shaped grooves, square ribs and sandpaper-roughened [Berger and Hau, 1979; Dawson and Trass, 1971; Postlethwaite and Lotz, 1988; Lolja, 2005; Zhao and Trass, 1996]. However, predefined roughness patterns are most likely not an accurate representation of the natural scallops roughness that develops over time in terms of size, shape and spacing, all of which affect the mass transfer rate. The development of scallops is not fully understood and very few experimental data are available thus far. The study of surface dissolution utilizing gypsum

test sections provides insight into the development of scallops [Villien et al., 2005]. The initiation of scallops requires the existence of imperfections in the pipe surface. These imperfections initiate scallops that are randomly distributed over the pipe surface. The scallops grow in size and increase in population over time, presumably from imperfections revealed by dissolution until the whole surface is populated with scallops. The roughness develops less in two-phase flow [Poulson, 1991], and thus, is less significant on the mass transfer in two-phase flow applications [Chisholm, 1978].

The mass transport consists of two mechanisms, diffusion and convection. The diffusion mass transfer process is usually several orders of magnitude slower in comparison to convective mass transfer. The convective mass transfer results from the turbulent motions of the fluid near the pipe surface. The piping geometry can significantly affect the flow and local turbulence, and hence the local mass transfer rate. The mass transfer in single-phase flows are typically correlated in the form,

$$Sh = ARe^x Sc^y \quad (1.1)$$

where the Sherwood number,  $Sh = hD/d$ ,  $Sc = \nu/d$  and  $Re = VD/\nu$ ,  $h$  is the mass transfer coefficient,  $D$  is the pipe diameter,  $d$  is the diffusivity of the pipe material,  $V$  is the velocity and  $\nu$  is the kinematic viscosity. The exponent  $x$  is typically between 0.5 and 1 and  $y$  is typically 0.33. Equations in the form given by (1.1) have been used for both smooth and rough surfaces, though for rough surface the mass transfer would also depends on the roughness height.

There has been extensive mass transfer studies in flow downstream of orifices, nozzles and in bends [Achenbach, 1976; Poulson and Robinson, 1988; Rizk et al., 1996; Runchal, 1971; Sparrow and Chrysler, 1986; Tagg et al., 1979; Wilkin et al., 1983] as these have been shown to be most susceptible to FAC. The locations of high mass transfer in separated flows, such as downstream of orifices and nozzles is easier to identify (reattachment zone) in comparison to bends. The mass transfer in bends under single-phase flow was found to increase along the elbow outer wall and reach a maximum near the elbow outlet [Achenbach, 1976; Mazhar et al., 2013; Sparrow and Chrysler, 1986; Wilkin et al., 1983]. A high mass transfer was also observed on the flanks of the elbow. The mass transfer in a 180 degree (U-shaped) elbow is similar to that in a single elbow but with higher mass transfer on the flanks of the second elbow [Poulson and Robinson, 1988]. Different localized thinning rates between the first and second elbow in back to back elbow configurations have also been noted at nuclear power plants. These thinning rates varied depending on the back to back elbow configuration, distance between the elbows and single-phase or two-phase flow. The high mass transfer in the U-shaped second elbow warrants further investigations in different back-to-back elbow configurations as they are commonly found in piping systems.

In an effort to better understand and quantify the effect of angular orientation of the second elbow relative to the first on FAC in back to back elbows, mass transfer experiments have been performed for the S and C configuration [Mazhar et al., unpublished; Chen et al., unpublished]. For the S configuration, the maximum mass transfer was found to be downstream of the first elbow for different separation distances

between the elbows. For short separation distances (0 to 2 pipe diameters), the maximum mass transfer location is found downstream of the first elbow outer wall, near the inlet on the intrados of the second elbow. When the separation distance increased to 5 pipe diameters between the elbows, the maximum mass transfer occurred at 2 diameters downstream of the first bend outer wall. For the C configuration, the maximum mass transfer is found on the inner side walls of the first and second elbow at short separation distance  $L/D = 0$ . At  $L/D = 1$ , the maximum mass transfer occurs on the inner side walls at the inlet of the second elbow. For  $L/D = 5$ , the results approaches that of a single 90 degree bend.

The single-phase flow structure in back to back elbows for different second elbow angles ( $0^\circ$ -U shaped,  $90^\circ$ -out of plane and  $180^\circ$ -S shaped) and different lengths of pipe between the elbows was studied by Murakami et al. [1969]. For small separation distances between the elbows, the flow structure in a 120 degree out of plane configuration was the most complex due to the presence of swirling flow in the second elbow. The highest pressure loss was reported for the out of plane configuration, with the lowest for the U-configuration and the S configuration falling in between. A larger pressure drop is often correlated with higher wall shear stresses and in turn higher mass transfer rates [Poulson, 1999]. The particle image velocimetry flow data of Yuki et al. [2011] in an out of plane elbow configuration showed high velocity and turbulence levels in the second elbow that was associated with a swirling flow. Swirl flow has been shown to increase heat transfer in piping [Sparrow and Chaboki, 1984; Yilmaz et al., 1999], and thus likely promote mass transfer based on the analogy between heat and mass transfer.

While there have been several flow and mass transfer measurements in single and dual elbows, there are no mass transfer studies for back to back elbows arranged in an out of plane configuration.

Mass transfer has been measured using a variety of techniques, including wall dissolution of plaster or metal, naphthalene sublimation and electrochemical limiting current diffusion methods [Berger and Hau, 1977; Poulson and Robinson, 1988; Sparrow and Chrysler, 1986; Wilkin et al., 1983]. For example, mass transfer rates have been measured using dissolution of copper tubing in acid ferric chloride solution [Poulson and Robinson, 1988; Poulson, 1991] and plaster in water [El-Gammal et al., 2010; Wilkin et al., 1983]. An advantage of the wall dissolution technique is that it allows for the development of roughness on the pipe surface due to the flow. Gypsum, in particular, allows for the casting of complex piping geometry. The dissolution of gypsum in water is transport controlled [Christoffersen and Christoffersen, 1976; Liu and Nancollas, 1971] and has been used to study mass transfer [Wilkin et al., 1983; El-Gammal et al., 2010] and scallop development [Villien et al., 2005] as mentioned previously.

The objective of this investigation is to determine the mass transfer distribution in back to back elbows arranged in a 90 degree out of plane configuration with different lengths of separation pipe between the elbows. The mass transfer is measured by using the dissolution of bend sections cast from gypsum in flowing water. The diffusivity of gypsum in water has a Schmidt number of 1280, similar to that for the diffusion of the iron magnetite layer of carbon steel piping in water, thus providing analogous mass transfer conditions to flow accelerated corrosion in power generation plants. The mass

transfer in the back to back out of plane configuration was measured under single-phase flow for different elbow separation distances of  $L/D = 0, 1, 2$  and  $5$  at a Reynolds number of  $70,000$ . The mass transfer was also measured under different annular two-phase air-water flow conditions to study the effect of increasing the water and air superficial velocities. Additional experiments were performed to study the effect of separation distance ( $L/D = 0, 1$  and  $5$ ) between the elbows for one annular for flow condition.

## 1.2 Sequence of Chapters

Chapter 1 provides an introduction to flow accelerated corrosion in power generation plants and the motivation for this work. The effect of surface roughness and piping geometry on FAC are discussed. Finally, the need to quantify mass transfer distribution in back to back elbows arranged in a  $90$  degree out of plane configuration is presented.

Chapter 2 provides a review of the existing literature on mass transfer measurement techniques, flow structure and mass transfer studies in bends under single and annular two-phase flow.

Chapter 3 presents the details of the experimental facility. Additionally, the experimental methodology and data reduction techniques to evaluate the mass transfer rates in the out of plane configuration are explained.

Chapter 4 presents and discusses the mass transfer results in the out of plane configuration under single and two-phase flow conditions. The effect of increasing water

and air superficial velocities and the effect of the separation distance between the elbows are discussed.

Chapter 5 summarizes the key mass transfer results obtained for the out of plane configuration under single and annular two-phase flow. Recommendations for future work are also provided here.

## Chapter 2 Literature Review

Flow accelerated corrosion is a piping degradation mechanism affecting carbon steel pipe of power generation plants. A schematic of the mechanism of FAC is shown in Figure 2.1. The chemical reaction of carbon steel pipe with water results in an oxide protective layer that consists mostly of magnetite  $\text{Fe}_3\text{O}_4$  at the pipe surface.



The reaction also results in



This protective magnetite oxide layer would dissolve into the flowing fluid in terms of  $\text{Fe}^{2+}$  ions. The rate of mass transfer through the diffusion layer is equal to the rate of mass transfer from the dissolution of the surface. The underlying carbon steel pipe would corrode to recreate the magnetite oxide layer resulting in wall thinning. The wall thinning rate is a combination of diffusive and convective mass transfer. The diffusive mass transfer is often neglected since convective mass transfer is several orders of magnitude higher.

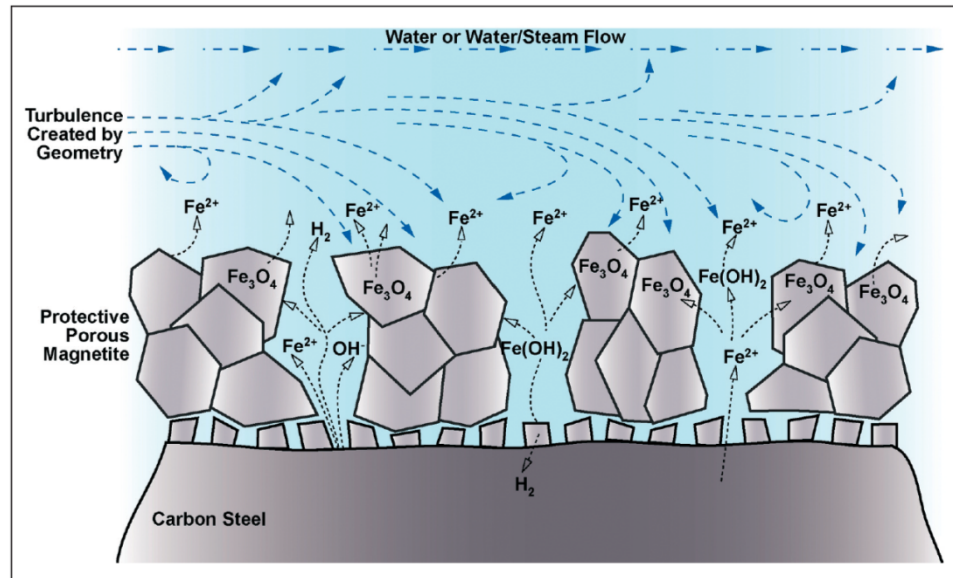


Figure 2.1: Schematic of the mechanism of flow accelerated corrosion [Dooley, 2008]

There are essentially two approaches to predicting mass transfer: (1) empirical correlations developed from wall thinning rate data obtained from plant operation, and (2) measuring mass transfer rates experimentally under controlled conditions. There is a high uncertainty in the data from plant operating conditions due to the effects of many parameters that can affect mass transfer. Thus, mass transfer measurements in a controlled laboratory environment allows for a better characterization of the parameters affecting FAC. Mass transfer has been measured using a variety of techniques, including wall dissolution of plaster or metal, naphthalene sublimation, the limiting current density electrochemical (LCDT) technique, and from heat transfer measurements using the analogy between heat and mass transfer.

The mass transfer can be evaluated from heat transfer measurements [Chilton and Colburn, 1934] and vice versa given the analogy between heat and mass transfer. The

analogy is based on the fact that temperature gradient provides the driving potential for heat transfer while a species concentration gradient in a mixture provides the driving potential for mass transfer [Incropera and Dewitt, 1985]. Sparrow and Chrysler [1986] used naphthalene sublimation, a mass transfer technique to evaluate the local heat transfer coefficient in a single 90 degree bend. The Schmidt number in FAC applications is typically in the order of 1500 and much higher than Prandtl numbers,  $Pr$  in heat transfer investigations that typically range up to 10. Thus the applicability of heat transfer measurements for high Schmidt number applications is unclear. It is difficult to perform heat transfer measurements at high  $Pr$ , due to uncommonly used high viscous fluids which may not be Newtonian.

The limiting current density electrochemical technique (LCDT) measures the current through the local cathode that is conducted by the electrons in the flow. The details of this technique can be found in Raboian [1986]. LCDT has been widely used for mass transfer measurements [Berger and Hau, 1977; Dawson and Trass, 1972; Poulson, 1983; Postlethwaite and Lotz; 1988; Zhao and Trass, 1997]. With the LCDT technique, the change in surface topology is negligible. Thus it is ideal for quantifying mass transfer on smooth surfaces, or a predefined rough surface with different roughness parameters. The disadvantage with using LCDT is the intrusiveness of the electrodes, causing disturbances to the flow. Also the location of large number of local cathodes and positioning of the anode to ensure uniform current distribution becomes challenging. In addition, the technique provides only point measurements at the locations of the electrodes.

The wall dissolving technique utilizes the surface dissolution of a coating or material, usually plaster or metal in the flowing fluid [Poulson, 1991; Poulson and Robinson, 1988; Wilkin et al., 1983; El-Gammal et al., 2010]. The mass transfer is measured based on the reduction in thickness of the material. Typical combinations of material and fluid that have been used include plaster in water [Wilkin et al., 1983; El-Gammal et al., 2010] and copper in hydrochloric acid solution [Poulson, 1991; Poulson, 1988]. Accurate measurement of the thickness loss with coated specimens and also ensuring uniform coating thickness is challenging. It is also important to ensure that there is no erosion which can be confirmed by performing experiments with different initial bulk concentrations. The advantage of the wall dissolving technique is that it allows the surface roughness to develop due to the flow. This is useful for the study of developing roughness [Villien et al., 2005] and in quantifying the development of surface roughness with time. For example, Poulson and Robinson [1988] proposed both smooth and rough mass transfer enhancement factors for single-phase flow in 180 degree bends to account for the development of roughness.

The dissolution of gypsum in water, in particular, is a transport controlled process [Liu and Nancollas, 1971] driven by the concentration difference between the saturated liquid at the gypsum surface and the bulk flowing water. The dissolution rate is given by,

$$R = h(C_w - C_b) \quad (2.3)$$

where  $R$  is the mass transfer rate,  $h$  is the mass transfer coefficient,  $C_w$  is the saturated gypsum concentration at the surface and  $C_b$  is the concentration in the bulk flowing water.

Since the dissolution of gypsum in water is surface diffusion controlled [Liu and Nancollas, 1971; Christoffersen and Christoffersen, 1976], the local mass transfer rate is strongly affected by turbulence and velocity in the near wall region.

The local mass transfer rate depends on the piping geometry and flow: single-phase or two-phase flow. Bends, which are the focus of this study, are one of the major components in piping systems of power generation plants. The single-phase flow mass transfer characteristics in bends have been investigated in greater detail [Wilkin et al., 1986; Poulson and Robinson, 1988; Sparrow and Chrysler; 1986; Mazhar et al., 2013] compared to the two-phase flow case. The mass transfer under annular two-phase flow conditions [Poulson, 1991] are reported to be higher compared to single-phase flow. The flow structure and mass transfer studies in bends under single and two-phase flow are reviewed in the subsequent sections.

## 2.1 Single-phase Flow

Mass transfer in bends is often characterized in terms of an enhancement factor relative to that in a straight pipe under the same flow condition. Coney [1980] proposed an enhancement correlation for the bends in the form,

$$\frac{Sh_{outside\ of\ bend}}{Sh_{fully\ developed\ tube}} = 1 + 2.2 \left(\frac{r}{R_c}\right)^{1.2} \left(\frac{L}{D}\right)^{0.75} \quad (2.4)$$

where  $R_c$  is the average bend radius,  $r$  is the tube inside radius,  $D$  is the inside diameter and  $L$  is the length along the centre line of the curved pipe.

Mass transfer in smooth pipes was investigated by Berger and Hau [1977] using the LCDT method for a range of Reynolds number from  $8 \times 10^3$  to  $2 \times 10^5$  and high Schmidt numbers between 1000 and 6000. Berger and Hau [1977] measured the mass transfer coefficients in fully developed flow and developed a correlation for the pipe Sherwood number as,

$$Sh = 0.0165Re^{0.86}Sc^{0.33} \quad (2.5)$$

The proposed correlation depends on the range of Schmidt number, and thus, is unreliable for the low Prandtl or Schmidt number range.

Surface roughness plays an important role in mass transfer, with greater effect particularly in high Schmidt number systems, due to the much thinner concentration boundary layers compared to the hydrodynamic boundary layers [Frank, 2006]. The effect of roughness on the pipe mass transfer was studied by Postlethwaite and Lotz [1988], also using the LCDT method. Slurry was used for the fluid, with the working electrode surface previously exposed to sand slurry to obtain a fully developed rough wear pattern. The roughness height,  $e$  was in the range of 0.18 to 0.25 mm with a corresponding  $e/D$  of approximately 0.0055. A correlation, similar to the smooth wall of Berger and Hau [1977], was developed for the rough wall case with a different Reynolds number exponent in the form,

$$Sh = 0.007Re^{0.96}Sc^{0.33} \quad (2.6)$$

It is evident that roughness enhances the mass transfer for plant conditions, and the correlation of Postlethwaite and Lotz [1988] is likely more practical to power generation plants due to the development of roughness on the pipe surface over time.

The studies of Dawson and Trass [1972] suggested that the ratio of the rough and smooth mass transfer coefficient,  $h_r/h_s$ , is a function of the Schmidt number as,

$$\frac{St_r}{St_s} = 1.94Sc^{0.1}(e^+)^{-0.1}; \quad e^+ > 25 \quad (2.7)$$

where  $St$  is the Stanton number and  $e^+$  is the roughness relative to the near wall scale. On the other hand, Berger and Hau [1979] concluded that  $h_r$  and  $h_s$  dependence on  $Sc$  is the same.

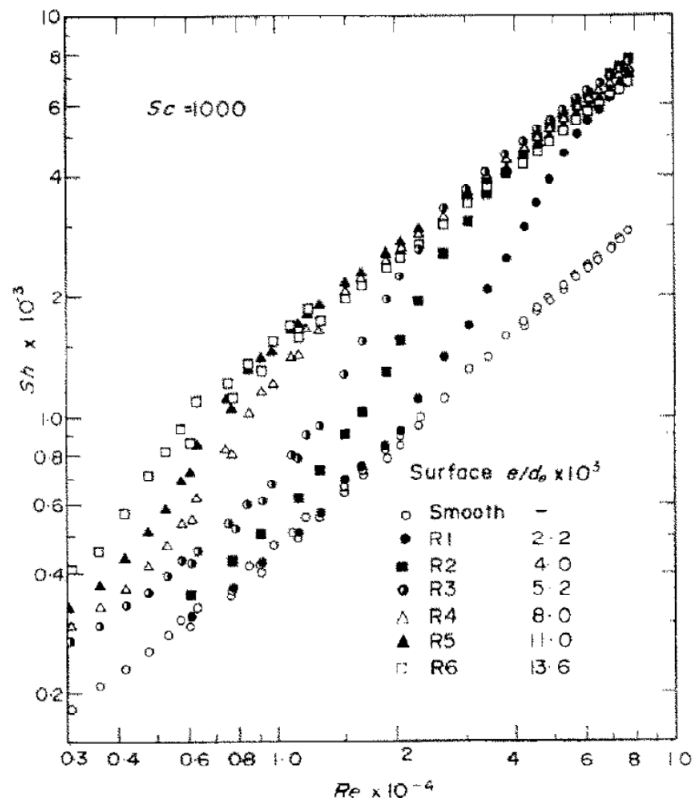


Figure 2.2: Dimensionless mass transfer coefficient for different roughness height [Dawson and Trass, 1972]

Dawson and Trass [1972] investigated the mass transfer rates in square ducts for smooth and different rough surfaces having V-shaped grooves with depth of 2-14 mil. The roughness effect was studied under a range of Reynolds number from 3,000 to 120,000 and Schmidt number from 390 to 4600. It was found that the roughness enhances the mass transfer more significantly with increasing Schmidt number. Since the major resistance to mass transfer in high  $Sc$  system is the low rate of molecular diffusion, any roughness generated turbulence near the wall will increase the mass transfer greatly. The Sherwood number at different Reynolds number for the different roughness height,  $e$  and Schmidt number of 1000 is shown in Figure 2.2. When the flow is above a certain Reynolds number, the mass transfer of the rough surfaces start to increase with increasing Reynolds number from a smooth to fully rough mass transfer rate. Higher surface roughness reaches the fully rough mass transfer rate at lower Reynolds number and vice versa. Dawson and Trass [1972] classified the pipe surface into hydrodynamically smooth, transitional and fully rough according to the relative roughness scale  $e^+ < 3$ ,  $5 < e^+ < 25$  and  $e^+ > 30$ , respectively.

Bends are common components of piping systems, and the flow in such components can be complex. The mass transfer in single bend has been studied by several researchers [Achenbach, 1976; Wilkin et al., 1983; Sparrow and Chrysler, 1986; Mazhar et al., 2013]. Achenbach [1976] evaluated the mass transfer in bends using naphthalene sublimation in air. However, the Schmidt number of 2 was much lower than in most mass transfer applications. Sparrow and Chrysler [1986] also used naphthalene sublimation for the measurement of local mass transfer in single bend for Reynolds

number in the range of 5000 to 100,000. The mass transfer was found to increase along the outer wall and reach a maximum near the bend outlet.

Wilkin et al. [1976] studied the mass transfer in single bends using a wall dissolving technique of plaster in water. The scallop pattern and mass transfer distribution along the bend was reported. The minimum mass transfer was on the inner wall corresponding to the region of flow separation. The suppression of mass transfer in this region was less marked with increasing Reynolds number. On the outer wall, the mass transfer increased with distance into the bend, and the maximum was observed on the bend flanks.

Mazhar et al. [2013] performed mass transfer experiments with single bend test sections cast from gypsum, for a range of Reynolds number from 40,000 to 130,000 at Schmidt number of 1280. The mass transfer was also found to increase along the bend outer wall and reach a maximum near the bend outlet. Additional regions of high mass transfer were reported at the inlet to the bend inner wall and midway into the bend on the sides of the inner wall. The maximum enhancement factor for the bend relative to the upstream pipe was approximately 1.85 for different cases of Reynolds number. The formation of scallops on the pipe surface increased the surface roughness well into the fully rough wall region for the range of Reynolds number in the study.

The mass transfer in a 180 degree elbow is similar to that in a single elbow but with higher mass transfer on the flanks of the second elbow [Poulson and Robinson, 1988]. A second high mass transfer location on the inside near the entry to the bend was

also observed. The maximum enhancement factor was less than 1.8 for a smooth wall bend with short radius of curvature  $R_c$  of 2.5 diameters. Poulson and Robinson [1988] also proposed a rough enhancement factor to account for the increase in surface roughness over time as,

$$\text{enhancement factor} = 0.71Re^{0.12} \quad (2.8)$$

The flow structure in dual elbows arranged in U, S, and 120 degree out of plane with different pipe length separating the elbows was investigated by Murakami et al. [1969]. The measurements of pressure and velocity profiles were performed along the exit pipe to the second elbow with a Pitot tube. For separation distance between the elbows less than 5 diameters, the pressure drop was highest for the 120 degree out of plane configuration, lowest for the U with the S configuration falling between the other two. Pressure drop is often correlated to shear stress and hence mass transfer rate [Poulson, 1999]. The flow structure in the downstream pipe of the second elbow of the 120 degree out of plane configuration was the most complex due to the presence of swirling flow. Swirl flow can promote heat transfer in pipes [Sparrow and Chaboki, 1984; Yilmaz et al., 1999], and thus likely to promote mass transfer due to heat-mass transfer analogy.

The recent particle imaging velocimetry measurements of Yuki et al. [2011] provides details of the flow structures in the 90 degree out of plane configuration. The bends were separated with a pipe length of 0.57 diameters. A high velocity flow with significant velocity fluctuations was measured at the inner wall of the second elbow as

seen in the results shown in Figure 2.3. The visualization downstream of the second elbow confirmed formation of strong swirling flow in the second elbow. Flow separation was observed at the inner wall of the first elbow but no obvious flow separation was seen in the second elbow.

There are no mass transfer studies in the out of plane configuration. Mass transfer studies in a 180 degree elbow [Poulson and Robinson, 1988] showed higher mass transfer in the second elbow. Furthermore, flow measurements and visualizations confirmed higher velocity and fluctuations associated with swirling flow within the second elbow in comparison to the first elbow along with higher pressure drop for the out of plane configuration. Thus, it is of interest to identify local maxima and mass transfer distribution in the second elbow in an out of plane configuration under single-phase flow with the natural development of surface roughness.

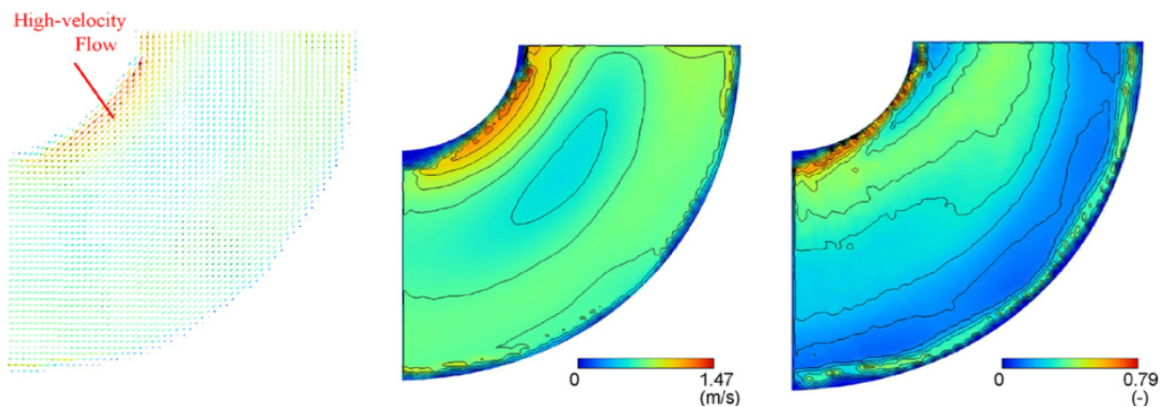


Figure 2.3: velocity profile in the second elbow of the out of plane configuration [Yuki et al., 2011]

## 2.2 Two-phase Flow

Two-phase steam-water flows are common in power generation plants and can result in localized regions of high mass transfer, especially in bend geometries. The presence of steam in two-phase steam-water flow can create localized turbulence and acceleration of the water resulting in high mass transfer. Annular flow, in particular, causes entrainment of liquid droplet resulting in high liquid impingement erosion at the impact location [Heymann, 1970]. Film thickness redistribution and liquid droplet impingement is believed to play a strong role in the overall mass transfer in bends [Poulson, 1991].

Mass transfer studies in bends under annular two phase-flow conditions are limited [Poulson, 1991; Pecherkin and Chekhovich, 2011; Mazhar et al., 2013]. Poulson [1991] measured the mass transfer in a 180 degree bend using a dissolvable wall technique with copper tubing in hydrochloric acid solution. Poulson [1991] found high mass transfer rates on the outer wall of the first elbow along the line of sight, which was attributed to the combined effect of liquid film redistribution and liquid droplet impingement. The combined effect of the two mechanisms would depend on the flow conditions, with droplet impingement being the main mechanism controlling mass transfer in the first elbow. The mass transfer in the latter half of the first bend and the second bend in the 180 degree bend was enhanced relative to the upstream pipe though less than at the line of sight location. The maximum enhancement in the first elbow relative to the upstream pipe was found to increase with increasing gas superficial

velocity as seen in the results shown in Figure 2.4. Poulson [1991] noted a lack of surface roughness development in two-phase flows compared to single phase flows. This is possibly attributed to no formation of a recirculation zone near the vicinity of initially small scallops due to the thin wall film in annular two-phase flows.

Mazhar et al. [2013] also found high mass transfer rates on the outer wall of the first elbow along the line of sight and in the latter half of a 90 degree bend, consistent with the results of Poulson [1991]. The mass transfer region in the latter half of the bend was lower and much narrower than at the line of sight location as seen in Figure 2.5. The enhancement of both regions relative to the upstream pipe increased with increasing either the air or water superficial velocities.

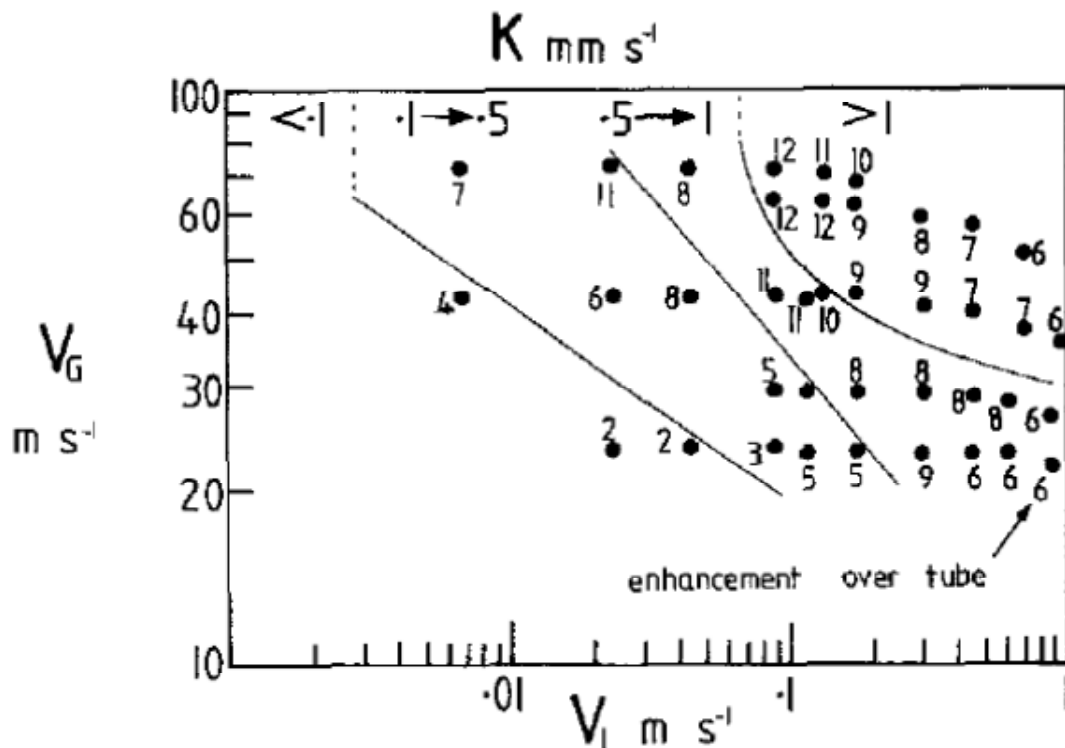


Figure 2.4: Effect of superficial gas and liquid velocities on maximum mass transfer coefficients (K) and enhancement at bends in two phase flow [Poulson, 1993]

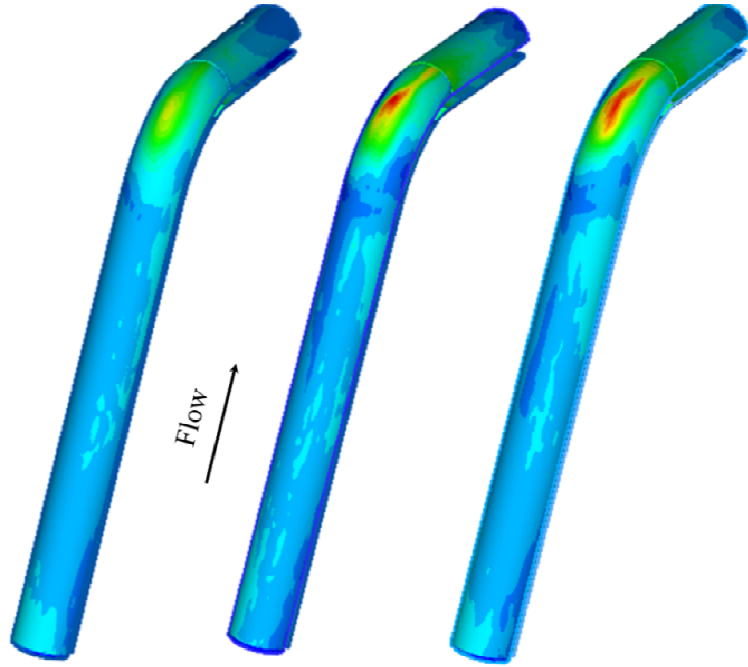


Figure 2.5: Effect of water superficial velocity on the Sherwood number distribution in a 90 degree bend for  $V_G = 30.2$  m/s,  $V_L = 0.18, 0.29$  and  $0.41$  m/s [Mazhar et al., 2013]

The mass transfer in bend is often characterized in terms of an enhancement relative to the upstream pipe. The mass transfer correlations for pipe can be based on heat transfer measurement and vice versa given the analogy between heat and mass transfer. The comparison of existing pipe correlations to experimental data in heat transfer under two-phase flow has been analyzed in a number of investigations [e.g. Kim et al., 1999; Kim and Ghajar, 2006]. Kim and Ghajar [2006] performed heat transfer measurements in air-water flows in a horizontal pipe for a range of two-phase flow regimes. They found the heat transfer coefficients correlated more strongly with the liquid Reynolds number than gas Reynolds number in the annular flow regime. However, the applicability of low Prandtl number heat transfer correlations to high Schmidt number applications is unclear. Poulson [1991] compared his mass transfer results for the upstream pipe to the heat

transfer correlation proposed by Chen [1966] and found good agreement for low mass qualities but poorer agreement for higher mass qualities. The comparison of the mass transfer results in the upstream pipe with existing heat transfer correlations is considered in chapter 4.

Annular two-phase flows in bends are complicated due to the effects of centrifugal force on the interaction of the phases. For example, estimating the film thickness redistribution in the bend is challenging. There would be thickening of the film on the bend outer wall due to deposition of entrained liquid droplets within the vapor core while the high shear stress induced by the fast moving gas core accelerates the liquid film hence thinning it [Maddock et al., 1974]. Gravity can also play a role depending on the flow condition and the orientation of the bend. Flow visualization, liquid film measurement and computational fluid dynamics simulation have been used to study the phase redistribution in bends [Maddock et al., 1974; Usui et al., 1980; Da Silva Lima and Thome, 2013; Tkaczyk and Morvan, 2011].

Maddock et al. [1974] investigated the characteristics of two-phase flow in a vertical bend through film thickness, film flow rate and gas core velocity measurements. The liquid droplets entrained in the gas core were found to deposit on the outer wall of the bend with some deflection of smaller droplets around the bend. The deposition of droplets thickened the film, consistent with the computational fluid dynamics results of Tkaczyk and Morvan [2011]. The maximum velocity of the gas core would move towards the outer wall with distance into the bend. On the inner wall, the film would slow down, thicken due to a lower shear stress and become unstable in the presence of the fast

moving gas core. Disturbance waves from the straight pipe caused droplet entrainment at the inner wall resulting in a spray of droplets that is deposited to the latter part of the outer wall as shown schematically in Figure 2.6.

The flow visualizations of Da Silva Lima and Thome [2013] also show the onset of liquid impingement against the outer wall of the second elbow of a 180 degree bend. The visualization was performed on 134a refrigerant flow in a U bend glass tube. In the annular flow regime, liquid droplet impingement to the second elbow can be seen for all three orientations of the U bend: horizontal, downwards and vertical. This is the result of liquid detachment from the thick liquid film at the inner wall. The detachment phenomenon is periodic and intensified with smaller radius of curvature,  $R_c$ . Waviness/breakup of the thick liquid film was also observed at the outer wall.

The high mass transfer in the first elbow outer wall is attributed to the impingement of liquid droplets entrained in the gas core flow [Maddock et al., 1974, Poulson, 1991; Mazhar et al., 2013]. However, the mechanism responsible for the mass transfer in the second elbow of back to back elbow configurations is unclear due to complex flow behaviour in the second elbow that is affected by the combined action of gravity and centrifugal force [Usui et al., 1980]. The focus here is on mass transfer in back to back elbows arranged in an out of plane configuration under annular two-phase flow.

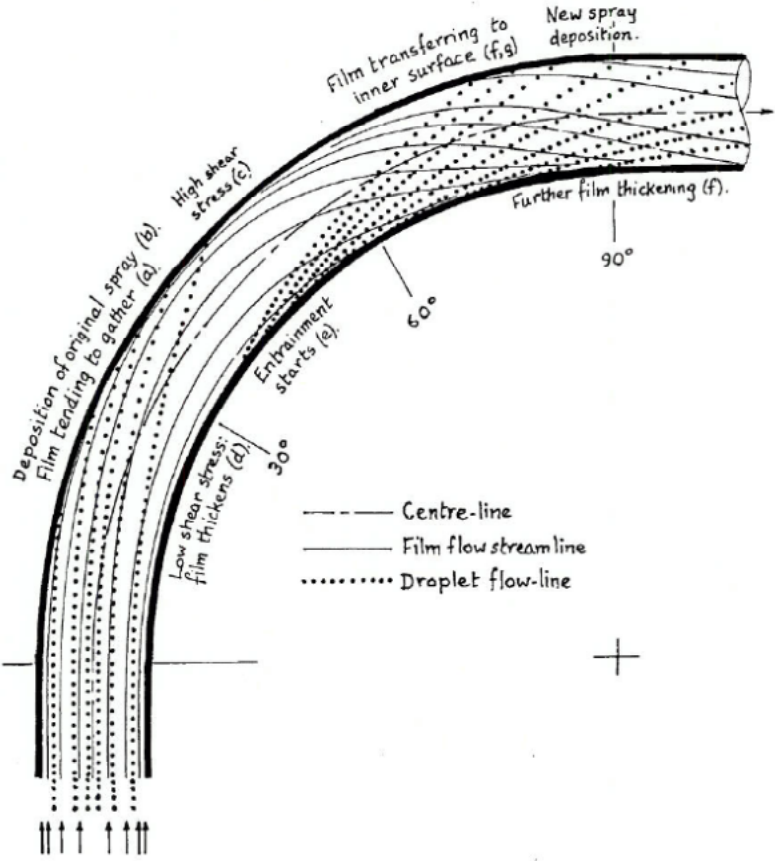


Figure 2.6: Schematic diagram of two-phase flow structure in a bend [Maddock et al., 1974]

# Chapter 3 Experimental Facility

## 3.1 Experimental Facility

The experiments were performed in a flow loop system shown schematically in Figure 3.1. For the single phase experiments, water is circulated through the system by a centrifugal pump. Flexible hoses are attached at the inlet and outlet of the pump to minimize vibrations to the system. The flow rate in the system is controlled by a globe valve situated at the bypass line to the reservoir. The water flow rate is measured by a turbine flow meter with an accuracy of  $\pm 1\%$  of the flow reading. The flow to the test section passes through a perforated plate and honeycombs that conditions the flow before it enters a 60 diameter long acrylic pipe leading to the test section. The test section is attached to an acrylic flange on the flow loop by four screw rods with two concentric O-rings between the flange and the test section to prevent leakage. The out of plane test section is attached to the upstream acrylic pipe with a right turn to the horizontal 90 degree elbow. The flow exits the test section to a 75 cm long acrylic pipe leading to a flexible hose that returns the water to the 100 l reservoir. The reservoir includes a cooling coil that is used to maintain the water temperature at  $25\text{ }^{\circ}\text{C} \pm 0.5\text{ }^{\circ}\text{C}$  during the experiment. A conductivity probe inside the reservoir measures the overall electrical

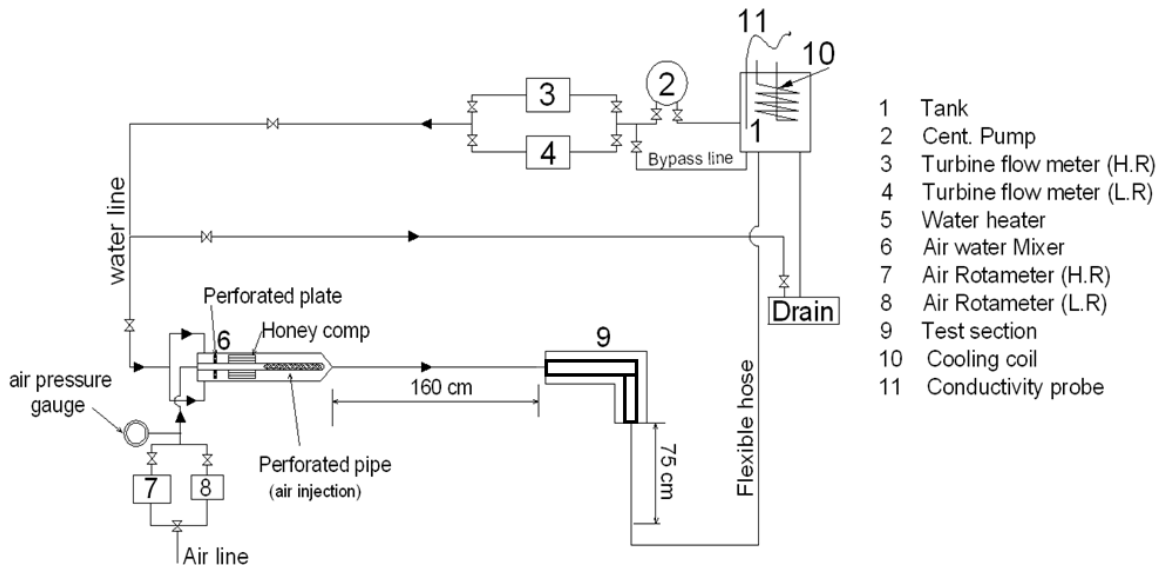


Figure 3.1: Schematic layout of all components in the experimental facility

conductivity of the water. Dissolved gypsum ions increase the electrical conductivity of the system with experimental time. The overall amount of gypsum dissolved can be calculated based on the electrical conductivity readings and calibration performed off line before the experiments. For the current series of tests, the overall mass removed varied from 20 g to 60 g, depending on the experimental time and separation distance between the back to back elbows.

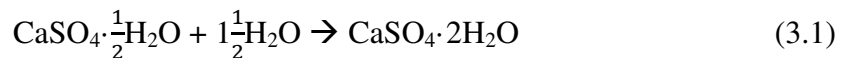
In the case of the two-phase flow experiments, air is supplied to the system through a pressure airline at room temperature. The air flow rate is measured by two air rotameters, one for low flow rates and the other for high flow rates, with an accuracy of  $\pm 2\%$  of the readings. The air and water (measured by a low range turbine flow meter) mixes in the air water mixer, which consisted of two concentric tubes. The water flows through the annulus, while the air flows in the inner tube, perforated along the end to

inject air into the annulus. There are four pressure gages, three upstream and one downstream of the test section to measure the changes in pressure along the flow loop.

### 3.2 Experimental Methodology

Mass transfer experiments were performed under single-phase and annular two-phase flow conditions using a wall dissolving technique with pipe section cast from gypsum. The pipe sections were cast in the mold shown in Figure 3.2. The mold was designed to accommodate different lengths of pipe, up to 5 pipe diameters, between the two bends. The different parts of the mold, made out of PVC plates were machined to high precision with a tolerance of  $\pm 0.03$  mm. The parts were assembled and held together by a set of screws. The core of the pipe and the bend was made out of rubber with steel rod inserts along the length shown in Figure 3.3a. The surface of the cores was wrapped with a balloon to achieve an initially smooth surface. The cores were oriented in the mold identically for each cast, and with a rotation lock piece applied to the bend to minimize any initial discrepancies in the cast sections.

The test sections are cast from gypsum that is generated by mixing hydrocal ( $\text{CaSO}_4 \cdot \frac{1}{2}\text{H}_2\text{O}$ ) with deionized water and a small amount of citric acid to slow the curing time to facilitate the casting. The chemical reaction of hydrocal and water is given by,



The mass ratio of hydrocal to water and citric acid used was 175:60:1. The mixture solution is vacuumed for five minutes to remove any trapped air bubbles before the

casting. Once the mixture solution is poured into the mould, it is left to cure for approximately 30 minutes. After the initial drying time, the rubber core is removed and subsequent sections are cast following the same approach to form the out of plane configuration, as shown in Figure 3.3b. The test sections are cast in sequence, starting with the downstream pipe, followed by the second elbow, the separation pipe, the first elbow and finally the upstream pipe.

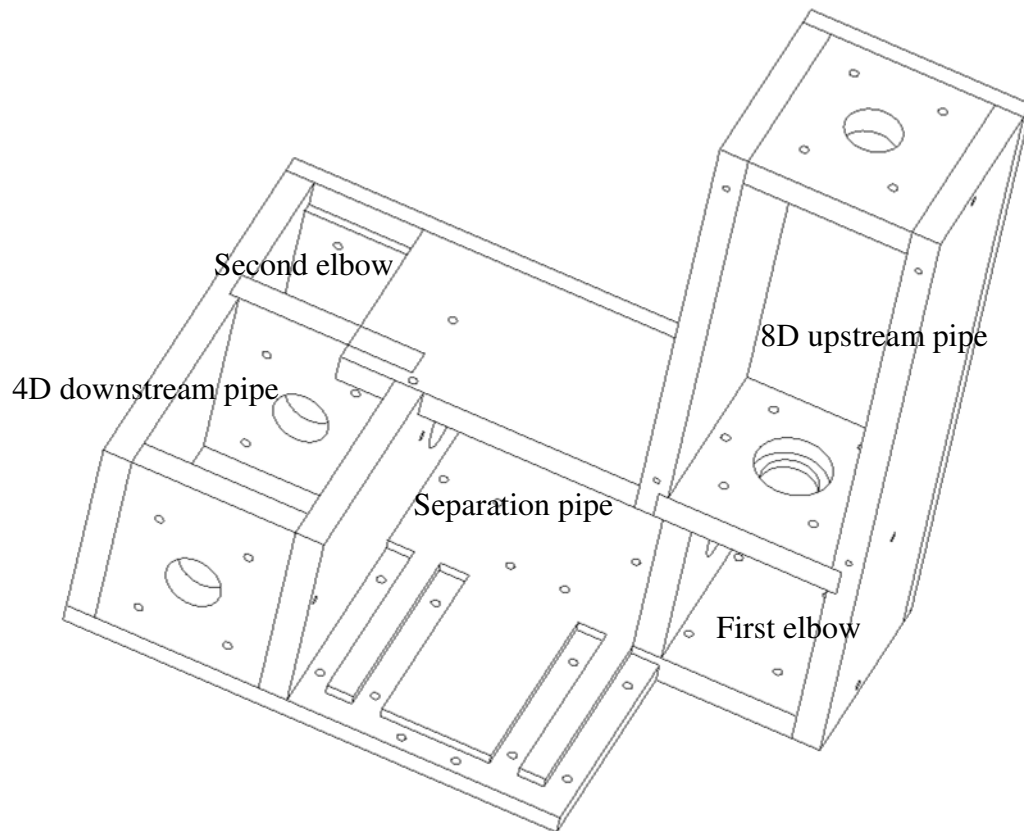


Figure 3.2: Schematic of casting mold for the out of plane configuration with different elbow separation distances

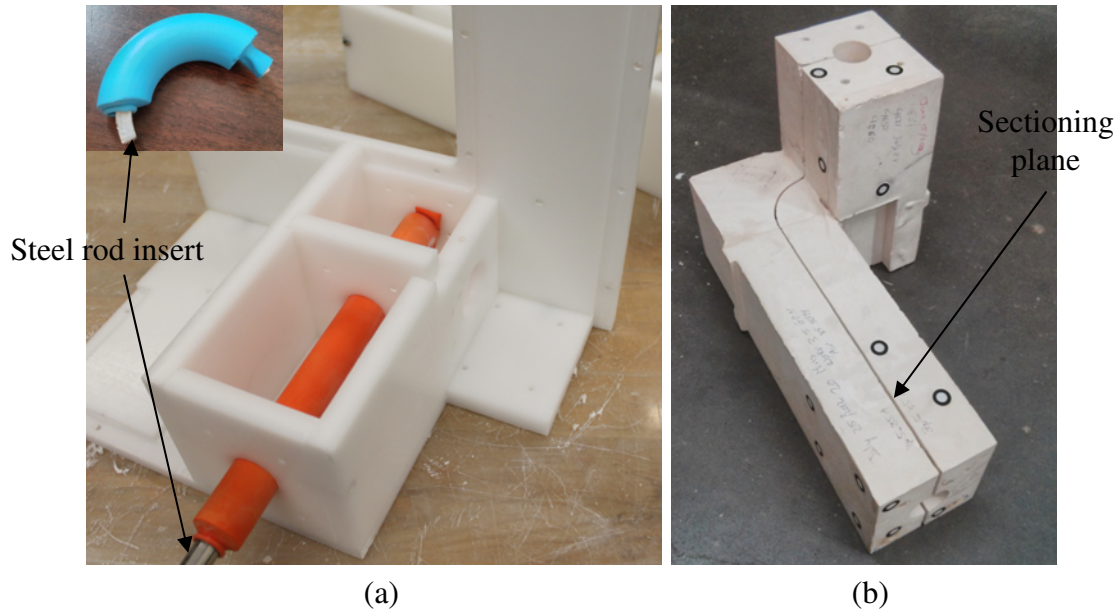


Figure 3.3: (a) out of plane mould with straight pipe core inserted (b) out of plane configuration test section

The final test sections have a nominal 2.5 cm inner diameter and elbows with radius of curvature  $R_c/D = 1.5$ . The samples are cast with a 20.3 cm upstream pipe and 10.2 cm downstream pipe to minimize entrance and exit effects. The sections are left to dry under ambient conditions after casting for approximately 20 days until the weight measured by a scale accurate to  $\pm 1$  g no longer decreases. The typical change in weight with time during the drying process is plotted in Figure 3.4. The sections are then tested in the flow loop for different times at the given Reynolds number and allowed to fully dry again before being sectioned for laser scanning to obtain the worn surface topology. Due to the destructive nature of the methodology, a new test section is required for each test time at the given Reynolds number.

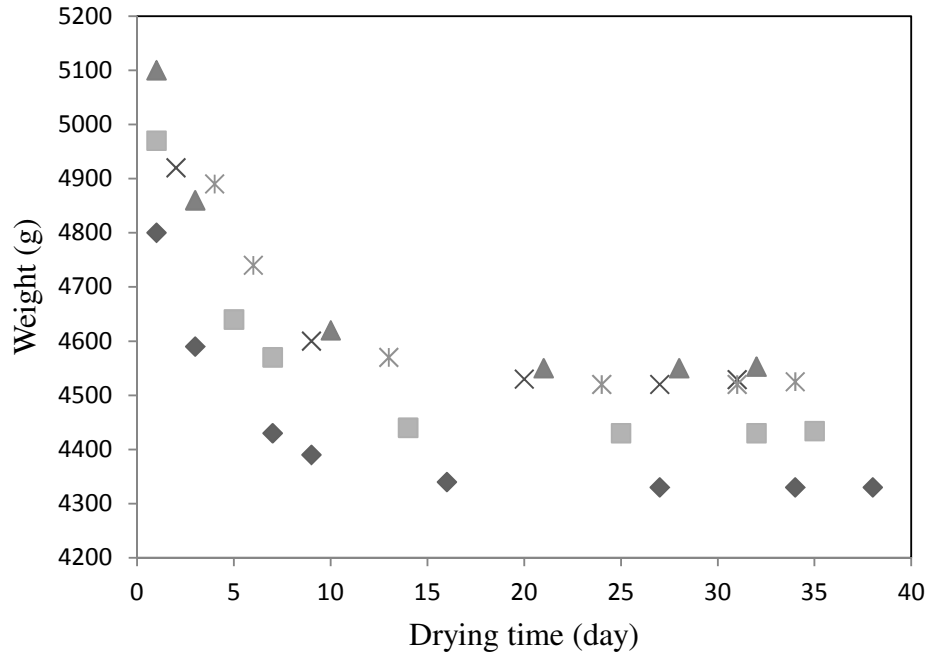


Figure 3.4: Typical test sections drying time measured by weight for  $L/D = 0$  configuration

In preparation for testing, the flow loop is initially flushed with tap water to clear the loop of any debris left in the system from previous tests. The reservoir is filled with 100 L of water and heated to  $25^{\circ}\text{C} \pm 0.5^{\circ}\text{C}$  by running the centrifugal pump with the recirculation line fully open. Once steady conditions have been reached, the experiment is initiated by fully opening the valve to the test section and setting the desired flow rate by adjusting the globe valve of the recirculation line. During the experiment, the temperature of the water is controlled to  $25 \pm 0.5^{\circ}\text{C}$  using a manually adjusted compensation cooling loop placed within the reservoir. The temperature and conductivity of the system is automatically logged every 30 seconds by computer software. The experimental time ranges from 30 minutes to 100 minutes, to ensure adequate wear yet keeping the maximum wear below 10% of the diameter to avoid geometry distortion.

Approximately five tests, including the unworn section for zero time, are performed for each elbow separation distance of  $L/D = 0, 1, 2$  and  $5$  under the same Reynolds number.

The single-phase flow test matrix is shown in Table 3.1.

Table 3.1: Single-phase flow test matrix for  $Re = 70,000, Sc = 1280$

Out of plane configuration	Experimental time (minutes)				
	$Re = 70,000 \quad Sc = 1280$				
$L/D = 0$	0	40	60	80	100
$L/D = 1$	0	-	60	-	100
$L/D = 2$	0	30	60	80	100
$L/D = 5$	0	30	60	80	100

The two-phase flow experiments were performed following the same approach, with the exception of water passing through the low range instead of the high range turbine flow meter leg used for single-phase flow. The experiment starts once both the water and air line is open. The tests are performed for a single time for each given flow condition of water and air superficial velocity. The testing time chosen for each test varies from 20 minutes to 30 minutes, depending on the two-phase annular flow condition. In two-phase flow the mass removed tends to be localized. Thus the testing time is shorter for higher air superficial velocity case and vice versa. The annular two-phase flow test matrix is presented in Table 3.2. The maximum radius change was found to be less than 15% of the diameter.

Table 3.2: Annular two-phase flow test matrix

Separation distance $L/D$	Superficial velocity		Experimental time (minutes)	Void fraction (Chisholm, 1983)	Mass quality
	Water (m/s)	Air (m/s)			
0	0.19	29.71	25	0.93	0.21
0	0.31	21.58	30	0.90	0.10
0	0.31	23.88	25	0.90	0.11
0, 1 and 5	0.31	28.82	20	0.91	0.14
0	0.44	27.96	20	0.89	0.11

The tested samples are left to fully dry under ambient conditions and sectioned into two halves with a 0.7 mm thick band saw. The surface topology of both halves is scanned using a three-dimensional handheld VIUScan laser scanner. The scanner emits a laser stripe on the pipe surface and detects its location using a camera. This technique is known as triangulation due to the formation of a triangle between the camera, the laser emitter and the laser on the pipe surface. The resolution of the scanner is 0.3 mm with a repeated accuracy of  $\pm 0.05$  mm.

The laser scan measurement captures and digitizes the surface topology of the worn sections in terms of a Cartesian coordinate point cloud. The sections are initially aligned to a common Cartesian coordinate origin using commercial software. Firstly, a cylindrical fit of the upstream pipe produces an axis along the center of the pipe. A perpendicular plane to the upstream pipe axis is then defined at the entrance of the pipe. The second and third planes are created based on a best fit of the flat side walls. The line intersections of the three planes are used to define the  $x$ ,  $y$  and  $z$ -axis. As a result, a

common coordinate system is created with origin at the corner of the section and z-axis parallel to the upstream pipe for all test sections. Unnecessary surfaces are trimmed resulting in the final pipe surface shown in Figure 3.5.

The raw data points are then gridded by averaging multiple data points within a grid cell having a resolution of 0.35mm in the crosswise and 0.70mm in the streamwise direction using in-house developed codes. The test sections are then re-aligned based on the symmetry of the upstream pipe. A further alignment check is made by examining for any systematic misalignment in the pipe based on the deviation of local mass removed from each section from a plot of the mass removed with experimental time from all tests at the same test condition. The surface topology of the unworn sample is then subtracted from the worn sections to obtain the local amount of mass removed for each testing time.

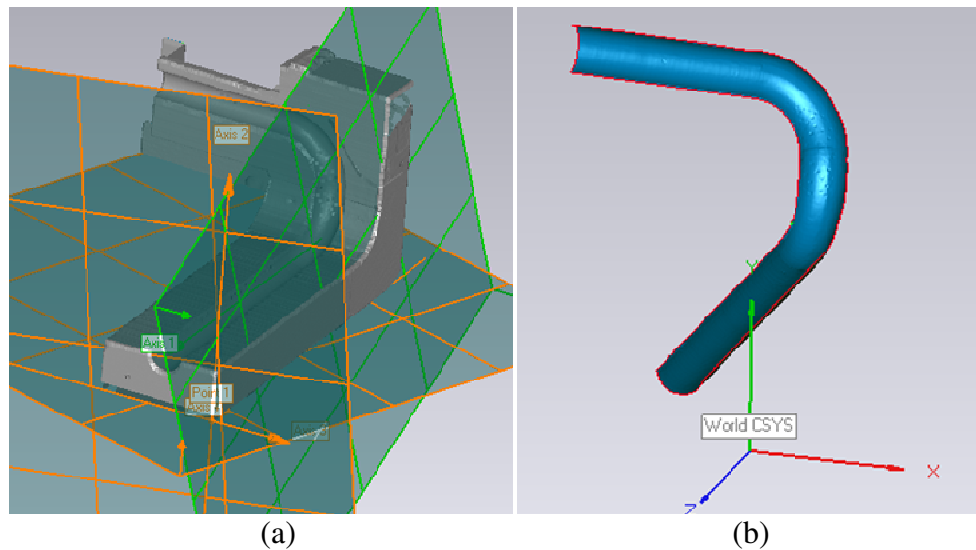


Figure 3.5: (a) scanned image (b) final pipe surface

### 3.3 Data Reduction

The algorithm for the alignment process of the tested sections is shown in Figure 3.6. The initial aligned Cartesian coordinate point clouds of the pipe surfaces are transferred to cylindrical coordinates for further analysis. The point clouds are then gridded using a cell size of 0.35 mm by 0.70 mm in the crosswise and streamwise direction, respectively. The gridding process averaged all data points within the grid cell, which helps to minimize noise and formulate a two dimensional matrix of the radius for data processing. When there are no data at a particular grid location, the local radius would be interpolated from the surrounding data. The original point cloud is 2 to 3 times denser than the gridded point cloud, thus the occurrence of no data is minimal. The worn sections are first aligned based on axisymmetric flow in the upstream pipe. To avoid any entrance effects, the flow is considered axisymmetric from 2 to 6 diameters from the pipe entrance. A systematic misalignment correction from the unworn section is applied to all worn sections. Further alignment considers the plane symmetry of the flow in the first elbow and separation pipe when applicable. Finally, the last alignment step is performed on the sections by considering the systematic deviation of the mass removed at each individual time from the best fit line of mass removed with modified time for all times.

The fine alignment based on axisymmetric flow in the upstream pipe is necessary to correct any minor misalignment resulting from the side wall planes of the cast sections. The alignment procedure in the upstream pipe follows a similar approach of Wang [2012]. Figure 3.7 shows cross sectional profiles of an unworn section at different  $z/D$

locations from the pipe entrance. It can be seen that the pipe surface is slightly misaligned from the ideal radius of 0.5 diameters. Thus, the Cartesian coordinate system needs to be shifted in both  $x$  and  $y$  direction, and possibly rotation until the average radius of region A, B and C are similar. The difference in average radius of region A and B computed along the pipe is,

$$O_x = \frac{(r_A - r_B)/2}{\cos\theta} \quad (3.2)$$

where  $r_A$  is the radius of region A,  $r_B$  is the radius of region B and  $O_x$  is the offset of the coordinate system in the  $x$  direction. The rotation about the  $y$  axis, if any, is computed based on the tilt of  $O_x$  along the pipe,  $z/D$ . Similarly, the difference in average radius of region C to the average radius of region A and B computed along the pipe is,

$$O_y = \frac{r_C - (r_A + r_B)/2}{\sin\theta} \quad (3.3)$$

where  $r_C$  is the radius of region C and  $O_y$  is the offset of the coordinate system in the  $y$  direction. Again, the rotation about the  $x$  axis is computed based on the tilt of  $O_y$  along the pipe,  $z/D$ . The offset of  $O_x$  and  $O_y$  is plot with dimensionless distance  $z/D$  into the pipe in Figure 3.8. A linear best fit line is fitted to the data, where its intercept and slope is the shift and rotation of the coordinate system, respectively. The process of correcting the coordinate system is iterated until the shift and rotation of  $O_x$  and  $O_y$  is less than 0.001mm and 0.0001 radians, respectively.

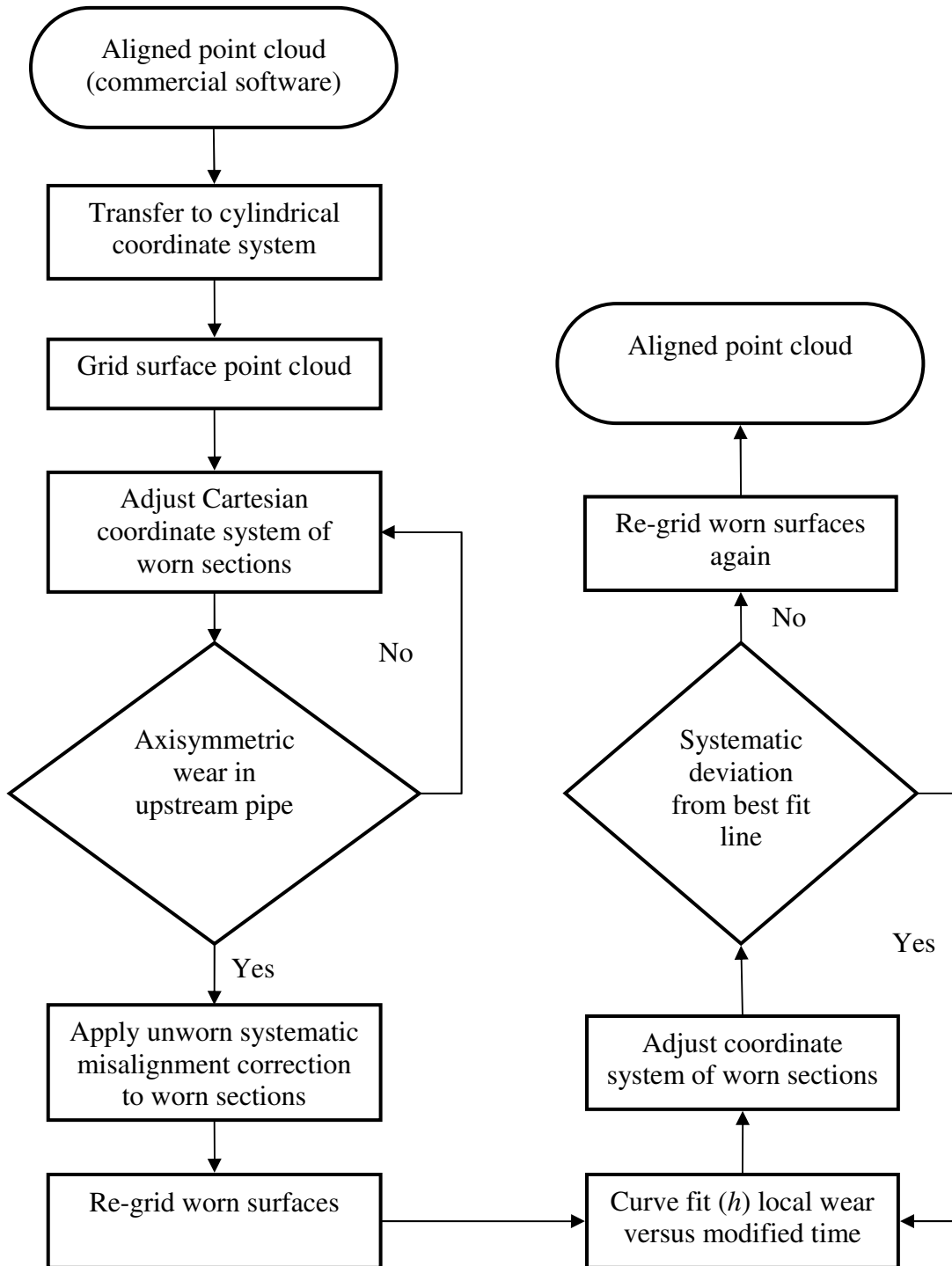


Figure 3.6: Algorithm for the alignment process of worn sections

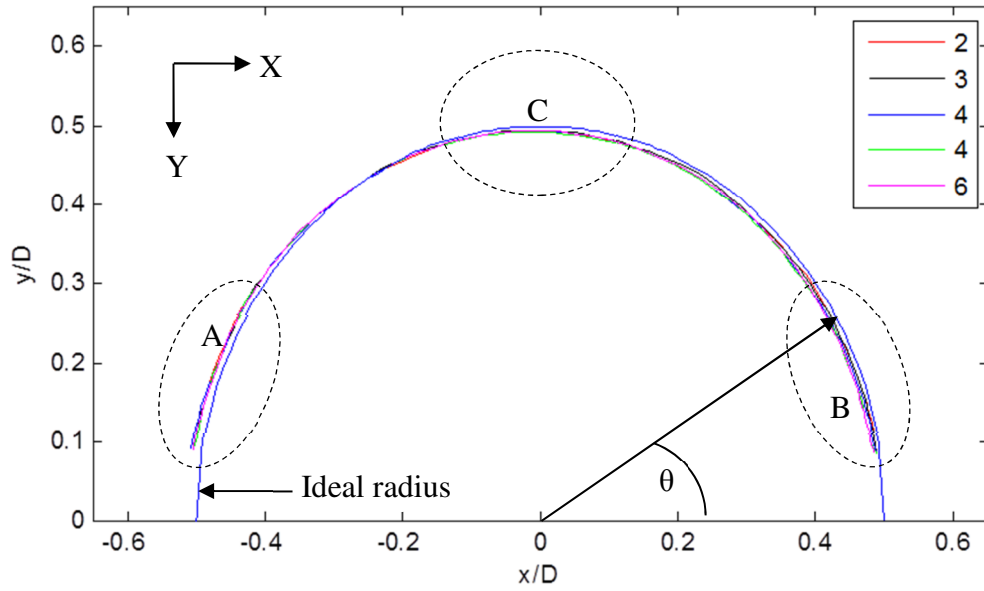


Figure 3.7: Radius profiles of the upstream pipe of an unworn section at different streamwise  $z/D$  locations from the pipe entrance

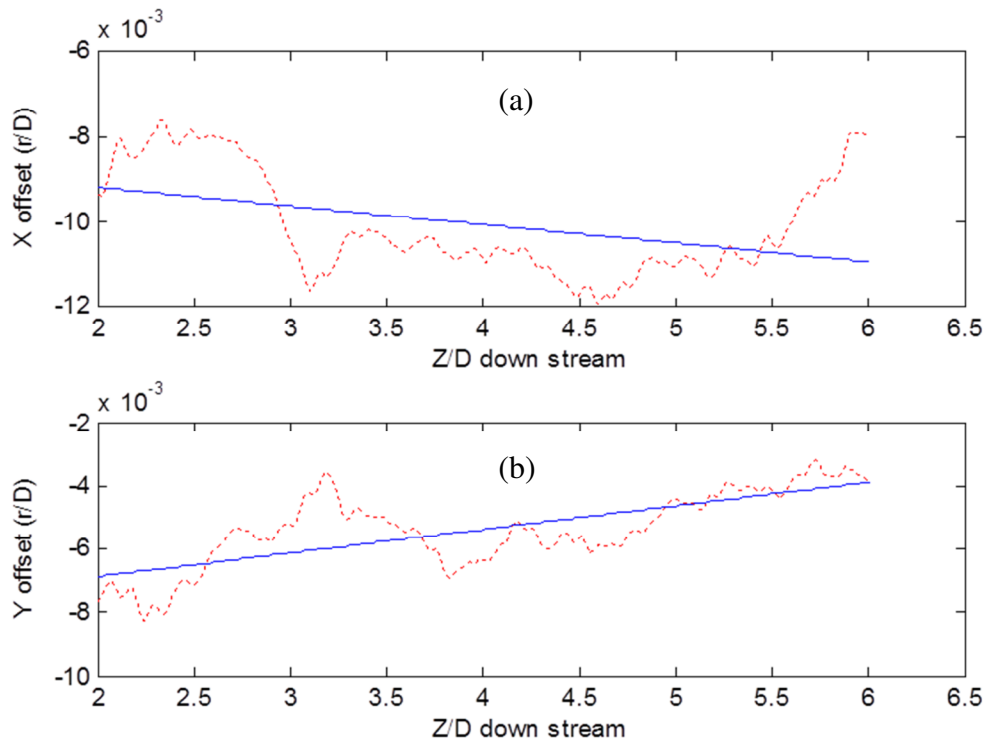


Figure 3.8: Offset of the coordinate system based on axisymmetric flow in the upstream pipe (a)  $x$  shift,  $y$  rotation (b)  $y$  shift,  $x$  rotation

The shift and rotation in  $x$  and  $y$  direction is corrected based on axisymmetric flow in the upstream pipe. However, the shift and rotation in the  $z$  axis which affects the separation pipe, second elbow and the downstream pipe cannot be detected by the axisymmetric flow condition in the upstream pipe. Therefore, a systematic misalignment correction in the  $z$  direction of the unworn section is applied to all worn sections assuming repeatability. Two unworn sections are used to check for repeatability of casting. The misalignment correction in the  $z$  direction of one unworn was applied to the other with good repeatability. The subtraction of local radius between the two unworn sections provides an estimation of the local variation of the casts. The variation between the unworn sections was found to be  $\pm 0.26$  mm in the second elbow and slightly higher in the downstream pipe, due to its further position away from the origin of the coordinate system. The uncertainties in the mass transfer due to casting variability, laser scanner measurement and other parameters are evaluated later.

After the previous alignment steps, the worn surfaces are re-gridded. The local mass removed is calculated by evaluating the volume of each grid cell shown in Figure 3.9. The volume of a grid cell in the straight pipe sections is obtained by volume integration with respect to the radius  $r$ , given as

$$V_{pipe} = \Delta z \Delta \theta \int_{r_o}^{r_o + \delta} r dr \quad (3.4)$$

where  $\Delta z$  is the length of the grid cell in the streamwise direction,  $\Delta \theta$  is the angular span of the grid cell in the circumferential direction,  $r_o$  is the initial radius and  $\delta$  is the surface

wear or depth in the radial direction. The volume of a grid cell in the bend is obtained by volume integration with respect to  $r$  and  $\theta$  given as,

$$\forall_{bend} = \Delta z \int_{\theta_o}^{\theta_o + \Delta\theta} \int_{r_o}^{r_o + \delta} \left(1 \pm \frac{r \sin\theta}{R_c}\right) r dr d\theta \quad (3.5)$$

where  $\theta_o$  is the initial angle and  $R_c$  is the radius of curvature of the elbow. The volume of a grid cell located in the intrados and extrados half of the bend is calculated with subtraction and addition sign, respectively. Evaluating the integral of equation (3.4) and (3.5) results in,

$$\forall_{pipe} = \delta \Delta z \Delta\theta \left(r_o + \frac{\delta}{2}\right) \quad (3.6)$$

$$\forall_{bend} = \Delta z \left[ \left(\frac{(r_o + \delta)^2 - r_o^2}{2}\right) \Delta\theta \pm \left(\frac{(r_o + \delta)^3 - r_o^3}{3R_c}\right) (\cos(\theta_o + \Delta\theta) - \cos\theta_o) \right] \quad (3.7)$$

The mass removed is obtained as follows,

$$m = \rho \forall \quad (3.8)$$

where  $\rho$  is the density, estimated by Wang [2012] to be 1581 kg/m<sup>3</sup>.

The mass transfer rate is determined from,

$$\frac{dm}{dt} = hA(C_w - C_b) \quad (3.9)$$

Here  $h$  is the mass transfer coefficient,  $A$  is the instantaneous surface area,  $C_b$  is the concentration in the bulk flowing fluid and  $C_w$  is the wall concentration taken to be the saturated concentration of gypsum in the water (2.6 g/l) [Wilkin et al., 1983; Villien et al.,

2001]. The instantaneous local surface area,  $A$  of a grid cell in the pipe and bend, is calculated as,

$$A_{pipe} = \Delta z \Delta \theta (r_o + \delta) \quad (3.10)$$

$$A_{bend} = \Delta z \int_{\theta_o}^{\theta_o + \Delta \theta} \left( 1 \pm \frac{r \sin \theta}{R_c} \right) r d\theta \quad (3.11)$$

Evaluating equation (3.11) results in,

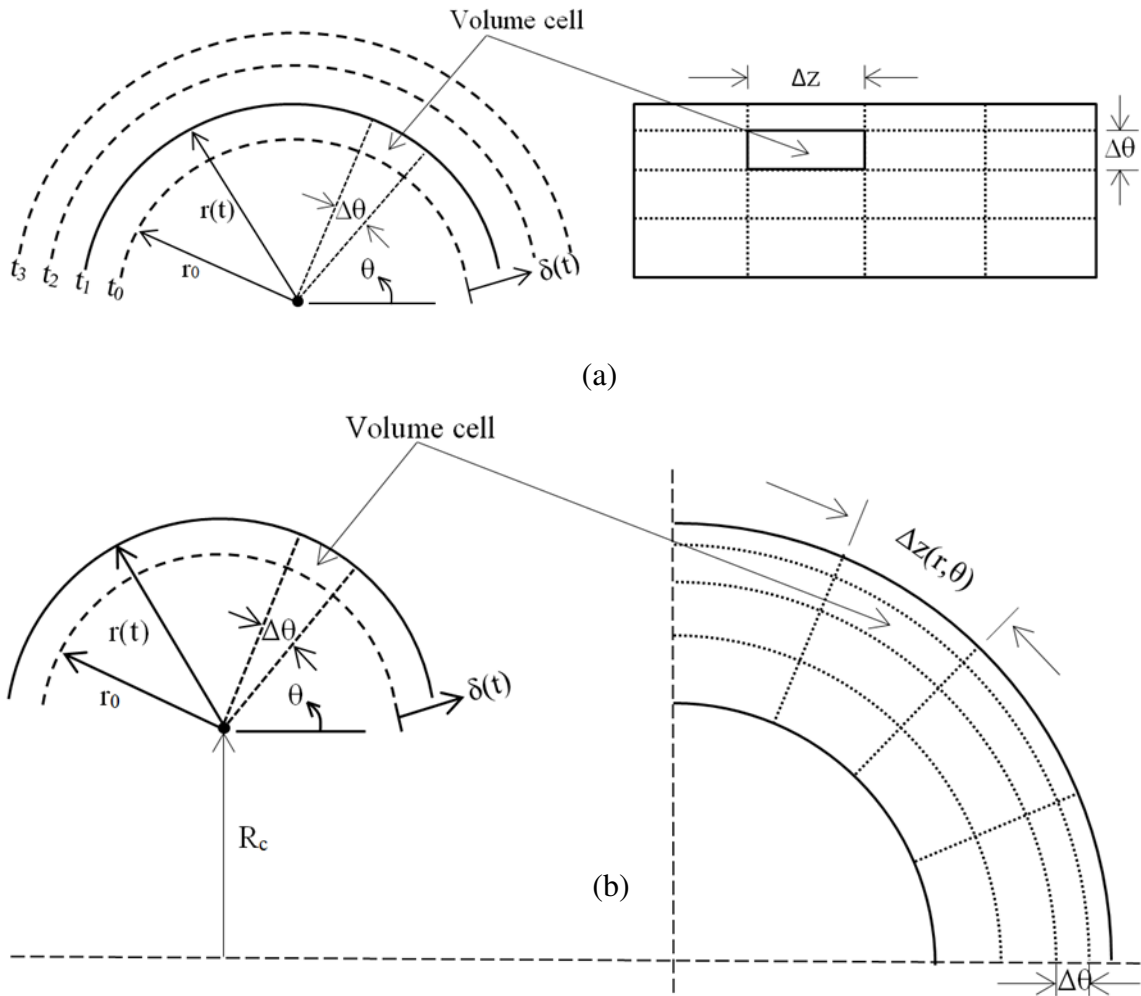


Figure 3.9: Two dimensional schematic diagram of volume of a grid cell for (a) straight pipe (b) extrados half of a bend

$$A_{bend} = \Delta z \left[ (r_o + \delta) \Delta \theta \pm \frac{(r_o + \delta)^2}{R_c} (\cos(\theta_o + \Delta \theta) - \cos \theta_o) \right] \quad (3.12)$$

The mass transfer equation (3.9) can be further reduced. Substituting equation (3.6), (3.8) and (3.10) for the pipe, into equation (3.9) results in,

$$\rho \Delta z \Delta \theta \frac{d \left[ \delta \left( r_o + \frac{\delta}{2} \right) \right]}{dt} = h [\Delta z \Delta \theta (r_o + \delta)] (C_w - C_b) \quad (3.13)$$

Taking the derivative of surface wear,  $\delta$  with respect to time  $t$  and simplifying equation (3.13) results in the mass transfer equation,

$$\frac{\rho d\delta}{dt} = h(C_w - C_b) \quad (3.14)$$

The simplification of the mass transfer equation (3.9) in the bend is evaluated using a similar approach to the pipe. Substituting equation (3.7), (3.8) and (3.11) into equation (3.9) and simplifying results in the mass transfer equation (3.14).

The bulk concentration,  $C_b$  in the close loop system increases with experimental time, thus decreasing the driving potential for mass transfer ( $C_w - C_b$ ). To account for this, a modified time  $\tau$  is defined as

$$\tau = \frac{1}{\Delta C_o} \int_0^t (C_w - C_b) dt \quad (3.15)$$

with

$$d\tau = \frac{1}{\Delta C_o} (C_w - C_b) dt \quad (3.16)$$

where  $\Delta C_o$  is the initial concentration difference between the pipe wall and the bulk flowing fluid. Therefore, equation (3.14) can be written as,

$$\frac{\rho d \delta}{d\tau} = h \Delta C_o \quad (3.17)$$

The typical concentration difference ( $C_w - C_b$ ) during the experiment is shown in Figure 3.10. The data is fitted with a second order polynomial and integrated to obtain the modified time.

The mass transfer coefficient,  $h$  and the Sherwood number,  $Sh$  is calculated as

$$h = \frac{\rho \delta}{\tau \Delta C_o} \quad (3.18)$$

$$Sh = \frac{h D_{avg}}{d} \quad (3.19)$$

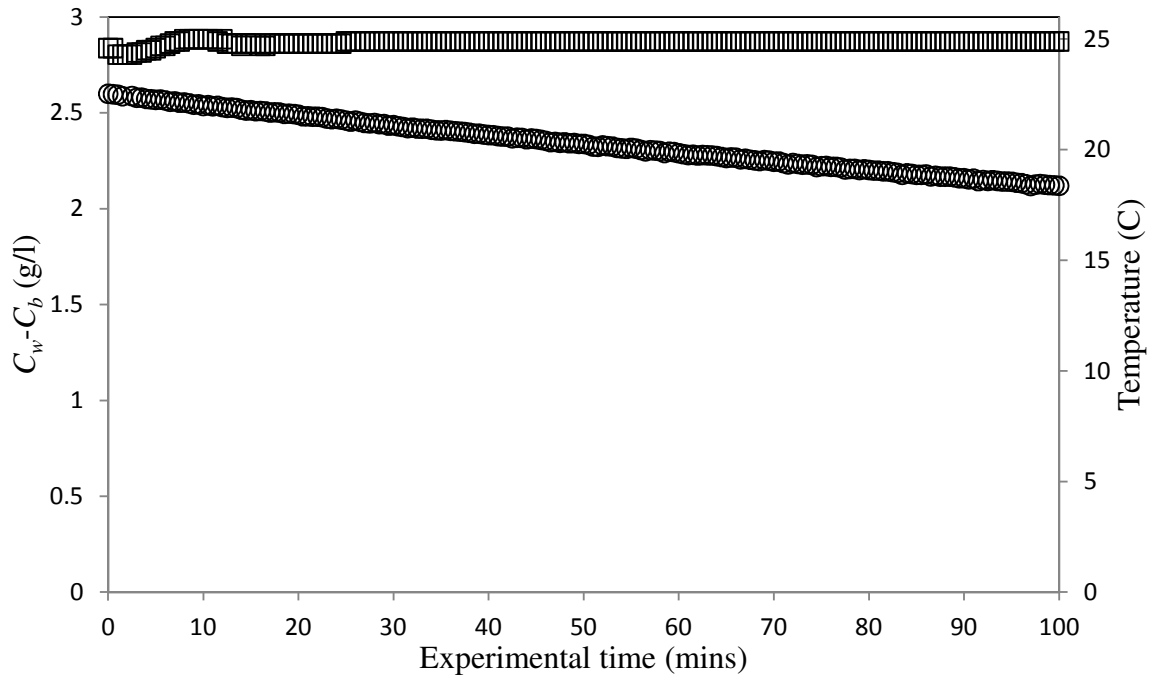


Figure 3.10: Typical concentration difference ( $\circ$ ) and water temperature ( $\square$ ) of the system during the experiment

where  $D_{avg}$  is the averaged pipe diameter over the test period and  $d$  is the diffusivity of gypsum in water ( $6.49\text{e-}10 \text{ m}^2/\text{s}$  [Wilkin et al., 1983; Robinson and Stokes, 1968]). The mass transfer coefficient  $h$  is obtained from the slope of a linear best fit line to the data of local wear  $\delta$  versus modified time  $\tau$ . The typical local mass transfer rate at different

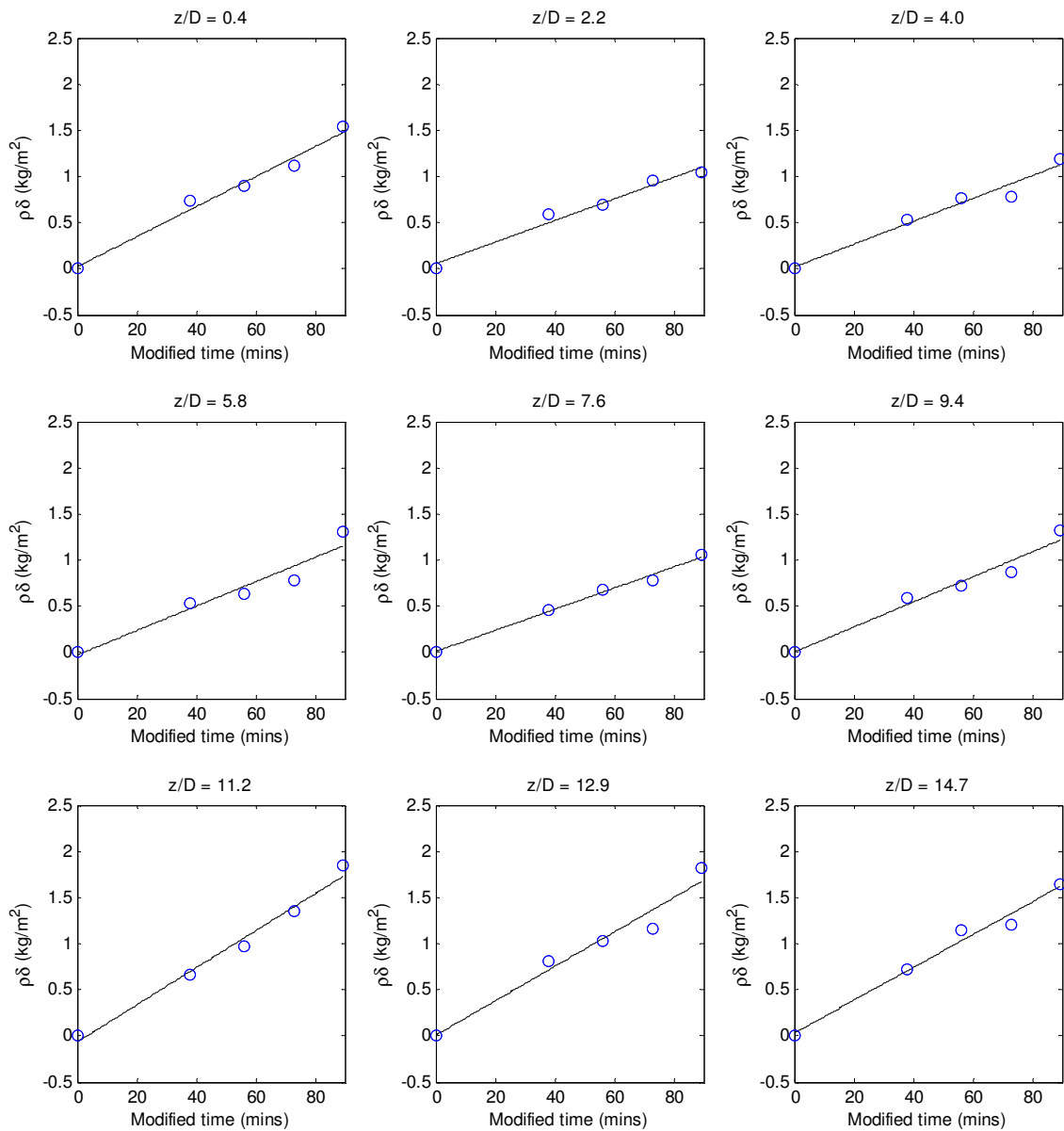


Figure 3.11: Typical local mass transfer removed at different streamwise location for  $\theta$  at 90 degree of the  $L/D = 0$  configuration

locations along the test section is shown in Figure 3.11. The mass transfer coefficient  $h$  is expected to increase with the development of surface roughness and decrease with the reduction in velocity due to the increase in pipe diameter with time. A linear best fit line was found to be the most appropriate for the current data.

The Reynolds number would decrease due to the increase in pipe diameter as it wears with time. The change in Reynolds number with time is given as,

$$Re(t) = Re_o \left[ 1 + \frac{2\delta(t)}{D_o} \right]^{-1} \quad (3.20)$$

where  $Re_o = 70,000$  is the initial Reynolds number based on the nominal unworn pipe diameter  $D_o$  of 2.54 cm. The maximum surface wear,  $\delta$  of the straight pipe for the single-phase flow experiments is approximately 0.04 diameters, resulting in an averaged Reynolds number of approximately 68,000 over the run time. The averaged diameter of the straight pipe under single and two-phase flow condition for the current experiments is approximately 2.65 cm and 2.60 cm, respectively.

A final step in the alignment of the test sections is performed by examining for any systematic misalignment in the pipe based on the deviation of local mass removed from each section versus the experimental trend line deduced from multiple sections. A similar analysis to aligning the upstream pipe, adapted from Wang [2012], described previously is applied here on the deviations. The aligned sections are re-gridded again and the overall mass removed of the sections is computed for comparison to the overall mass dissolved in the water from the increase in conductivity and that from the weight

measurement before and after the test. In all cases, the overall mass removed computed from the laser scan data after alignment is in agreement with the weight measurement before and after the test and from the conductivity readings to within  $\pm 10\%$ , as shown in Figure 3.12. The good agreement in the overall mass removed provides confidence in the validity of the linear fit to obtain the mass transfer coefficient. The local Sherwood number is finally computed by averaging over a larger grid cell of 2.1mm in the crosswise direction by 4.2mm in the streamwise direction to obtain an estimate of the local mean Sherwood number. The grid cell size is chosen such that local features are not lost due to averaging. The local mean surface wear was also estimated by averaging over a grid cell of the same dimension, 2.1mm by 4.2mm. The surface roughness is obtained by subtracting the local surface wear from the local mean result. The roughness height,  $e$  is estimated by examining the surfaces in profile to obtain valley to peak height.

The electrical conductivity readings of the water in the system are correlated to the amount of gypsum dissolved through calibration data determined before the experiments. The calibration was performed by dissolving a measured amount of gypsum powder into an approximately 2L bucket of water, measured by weight. The water-gypsum mixture is occasionally stirred for a duration of approximately 10 minutes. The conductivity reading is recorded when the conductivity no longer changes. Two sets of calibrations were performed; the first set of data consisted of adding additional amount of gypsum powder to the same bucket of water, while the second set of data starts with a new bucket of water for each measurement of gypsum powder to be dissolved. The calibration results are plotted in Figure 3.13. The data are fitted with a linear best fit line

with slope equal to  $1.16 \times 10^{-3} (\text{g/l}) / (\text{uS/cm})$ . The overall mass removed based on the conductivity recording is determined from the equation,

$$m_{cond} = 0.00116 X_{cond} \forall_{reservoir} \quad (3.21)$$

where  $X_{cond}$  is the conductivity reading,  $\forall_{reservoir}$  is the volume of water in the system and  $m_{cond}$  is the total mass removed from the test section.

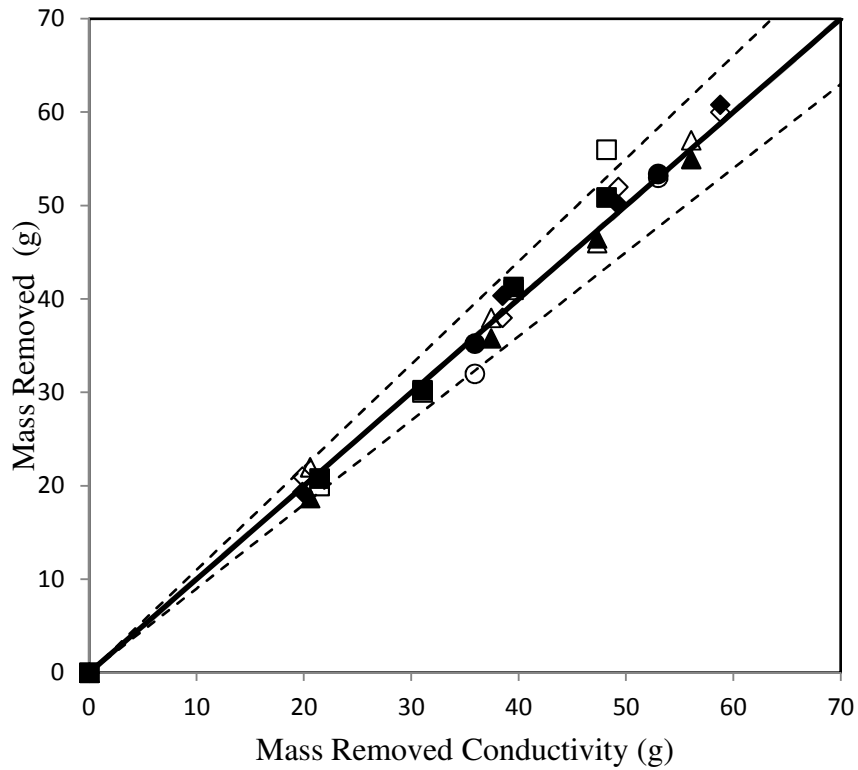


Figure 3.12: Comparison of the overall mass removed of the laser scanner measurement data reduction (filled symbols) and the weight measurement before and after test (open symbols) to the conductivity increase in the system. ■  $L/D = 0$ , ●  $L/D = 1$ , ▲  $L/D = 2$  and ◆  $L/D = 5$

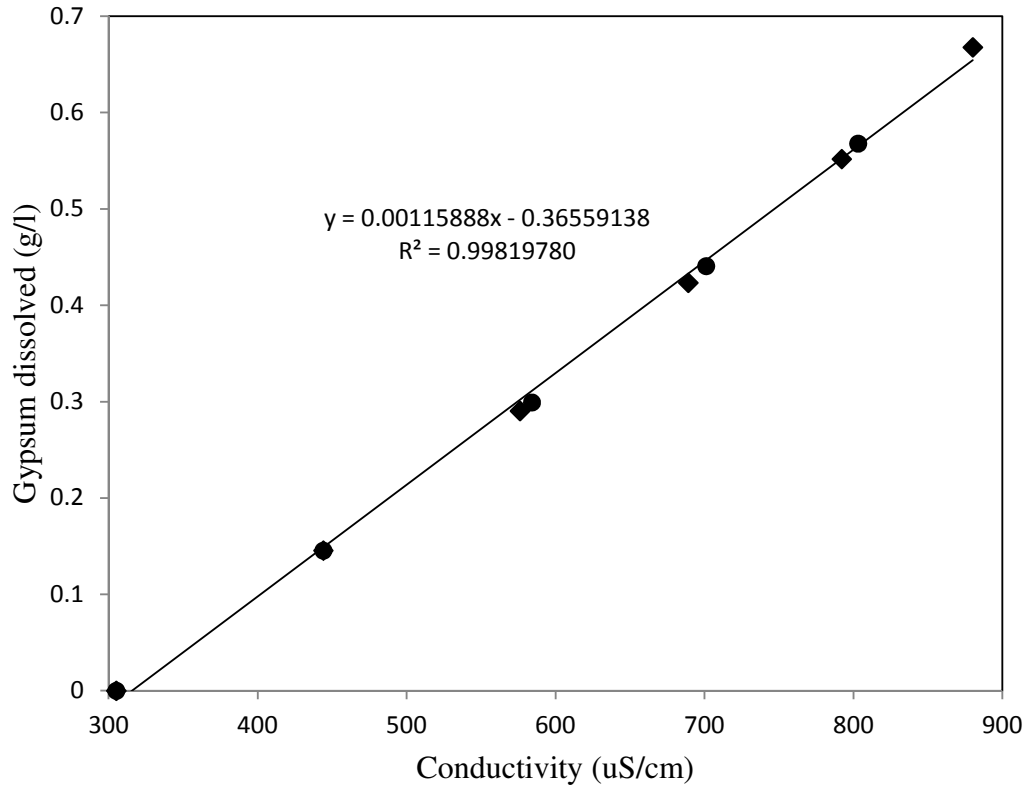


Figure 3.13: Calibration data of mass of gypsum removed and electrical conductivity

### 3.4 Uncertainty analysis

The mass transfer coefficient is calculated using the equation,

$$h = \frac{\rho \delta}{\tau \Delta C_o} \quad (3.22)$$

where  $\delta$  is the local surface wear,  $\Delta C_o$  is the initial concentration difference between the pipe wall and bulk flowing fluid,  $\tau$  is the modified time,  $\rho$  is the density and  $h$  is the mass transfer coefficient. The total uncertainty in the dependent variable, mass transfer coefficient can be expressed in terms of the independent measured variables [Coleman and Steele, 1998];  $\delta$ ,  $\Delta C_o$  and  $\tau$  according to the following equation,

$$dh = \sqrt{\left(\frac{\rho}{\tau\Delta C_o} d\delta\right)^2 + \left(\frac{\delta}{\tau\Delta C_o} d\rho\right)^2 + \left(-\frac{\rho\delta}{\tau^2\Delta C_o} d\tau\right)^2 + \left(-\frac{\rho\delta}{\tau\Delta C_o^2} d\Delta C_o\right)^2} \quad (3.23)$$

The uncertainty in the mass transfer coefficient is a combination of casting variability, laser scanner measurement, density of test sections and modified time (combination of gypsum concentration measurement in the system and experimental time) uncertainty.

The laser scanner has an accuracy of  $\pm 0.05$  mm as listed under specification. The uncertainty in the modified time is estimated to be  $\pm 2$  minutes. The random uncertainty due to the variability of the casting was estimated from two unworn sections to be approximately  $\pm 0.26$  mm. Thus, several test times are used to reduce the uncertainty of the measurements. The uncertainty in the measured density of the gypsum was  $\pm 40$  kg/m<sup>3</sup>. The largest uncertainty in the mass transfer coefficient depends on the uncertainty of the local surface wear,  $\delta$ . The uncertainty in the mass transfer coefficient is estimated to be  $\pm 23\%$ .

### 3.5 Mass Transfer Erosion Test

The role of erosion, if any, was examined by repeating an experiment with an initial water bulk concentration of 46 percent of the wall concentration. Assuming the mechanism of erosion is present, the total mass removal rate equation (3.17) would be a combination of mass removed by dissolution and erosion, given as

$$\frac{\rho d\delta_t}{d\tau} = \frac{\rho d\delta_e}{d\tau} + h\Delta C_o \quad (3.24)$$

where  $\delta_t$  is the total surface wear and  $\delta_e$  is the surface wear due to erosion. The mass removed due to dissolution is a function of the mass transfer coefficient and the initial bulk concentration difference, while the mass removed due to erosion depends solely on the flow conditions. Consequently, erosion is more likely to occur in annular two-phase flow in comparison to single-phase flow. The fast moving liquid droplets and liquid film might cause mechanical wear at the maximum mass transfer location in the two-phase experiments.

To determine the two unknown parameters,  $h$  and  $\delta_e$  requires two experiments, while other parameters,  $\delta_t$  and  $\Delta C_o$  are directly measured or calculated for the case of modified time  $\tau$ . Two experiments with different initial water bulk concentration of 0 and 46 percent of the wall concentration were performed at the same flow conditions, with liquid and gas superficial velocity  $V_L = 0.31\text{m/s}$  and  $V_G = 28.82\text{ m/s}$ , respectively. To achieve 46 percent bulk concentration, 1.2 g/l of gypsum powder was dissolved into the reservoir. The water in the reservoir is recirculated through the recirculation line, to ensure thorough dissolution of gypsum in water before testing. The two experiments were performed for 20 minutes each. The difference in concentration between the wall and the bulk flow with time is plotted in Figure 3.14. The rate of gypsum dissolved for the initial bulk water concentration of 46 percent of the wall concentration was much lower in comparison to the 0 percent case.

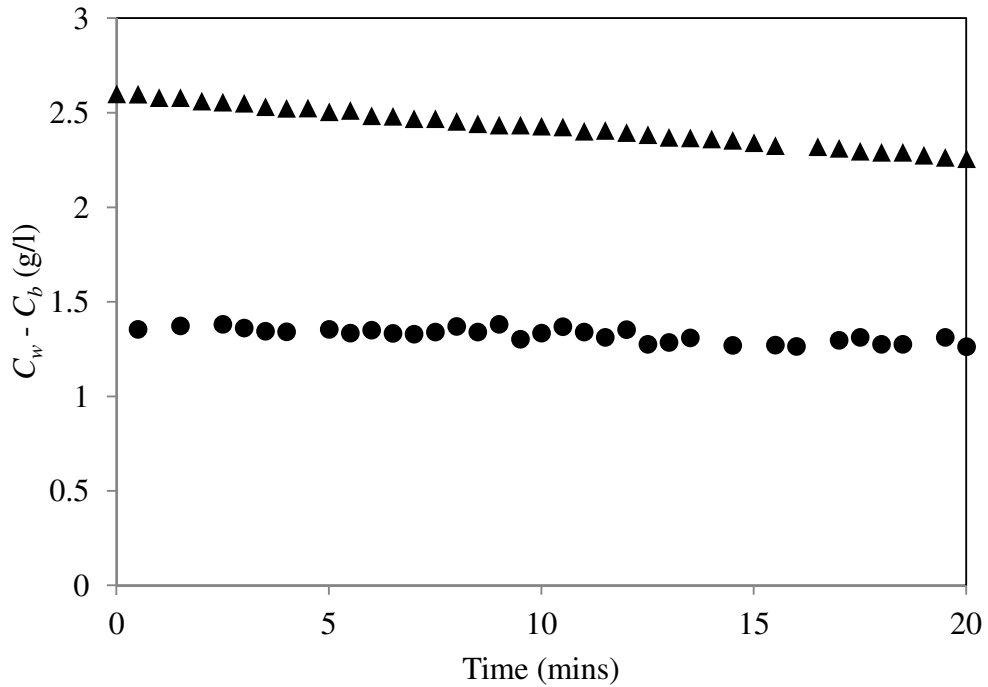


Figure 3.14: Concentration difference of wall and the bulk water flow for ▲ 0 g/l and ● 1.2 g/l initial bulk concentration.  $V_L = 0.31$  m/s and  $V_G = 28.82$  m/s

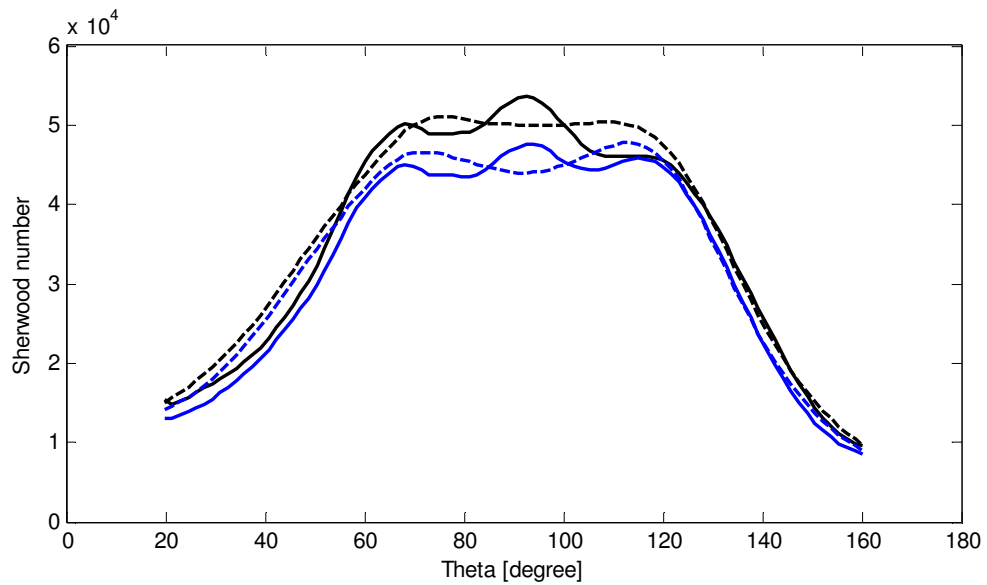


Figure 3.15: Maximum Sherwood number in the first elbow outer wall for: - 1.2g/l - - 0 g/l at different angles along the bend (black:  $\Phi = 40^\circ$  and blue:  $\Phi = 45^\circ$ )

The highest mass transfer location is found on the outer wall of the first elbow for annular two-phase flow. The Sherwood number profiles in the high mass transfer vicinity,  $\Phi = 40^\circ$  and  $\Phi = 45^\circ$  along the first elbow for the two different initial bulk concentration cases is plotted in Figure 3.15. The discrepancies in the maximum Sherwood number of the two cases are small, approximately less than 10%, and within the uncertainty of the mass transfer coefficient. Therefore, it is concluded that there is no mass transfer due to erosion.

# Chapter 4 Results and Discussion

## 4.1 Single-phase Flow Results

The distribution of the Sherwood number ( $sh$ ) for the different separation distances are shown in Figure 4.1. The distribution shows uniform and comparable Sherwood number in the upstream pipe. There was a region of elevated Sherwood number at the pipe inlet due to entrance effects but this only persisted for approximately two diameters. The Sherwood number in the first elbow increases in the downstream direction with a high value on the flanks and outer wall near the exit. This region of high Sherwood number continues into the separation pipe between the elbows and the second elbow for the small separation distances. For the cases with  $L/D = 2$  and 5, this region of high mass transfer (Region I) occurs on the outer wall of the pipe separating the elbows, and is located 1 to 3 diameters downstream of the first elbow. Thus this region can be described as being downstream of the first elbow outer wall, consistent with the mass transfer in single  $90^\circ$  elbows where a high mass transfer occurred outside of the elbow outer wall [Achenbach, 1976].

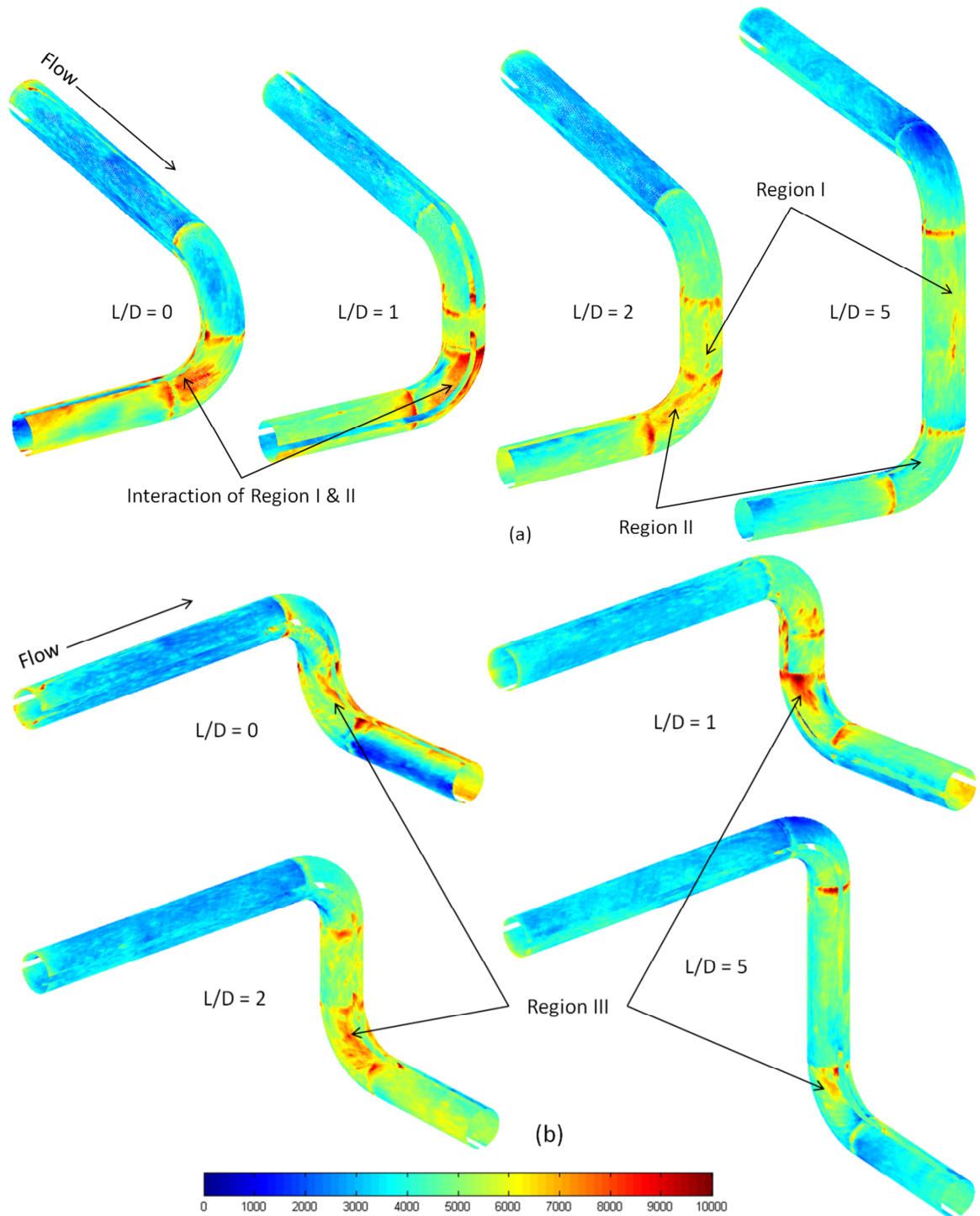


Figure 4.1: Distribution of the Sherwood number on (a) outer wall region and (b) inner wall region for 90° out of plane configuration with separation distances  $L/D = 0, 1, 2$  and 5 between the elbows for  $Re = 70,000$  and  $Sc = 1280$

A second region of high mass transfer occurred downstream of the separation pipe between the outer side wall and inner wall of the second elbow (Region II). The mass transfer enhancement in this region is modest at large separation distance, but becomes predominant as the separation distance decreases. For small separation distances, there seems to be an interaction between this region and the region downstream of the first elbow outer wall. This resulted in the widening of the high mass transfer area in the second elbow outer side wall of the configuration at  $L/D$  of 1. For the configuration with no separation pipe, the curvature effect of the second elbow on the region downstream of the first elbow outer wall resulted in a single high mass transfer region that shifted towards the second elbow inner wall. The highest mass transfer region downstream of the first elbow outer wall shifts upstream relative to the end of the second elbow with increasing elbow separation distance. The magnitude also decreases as the separation distance increases. This is not unexpected since as the elbow separation distance increases, the effect of the elbow on the flow features is reduced. The Sherwood number in the downstream pipe of the second elbow decreases but is generally higher than that of the upstream pipe. The localized high mass transfer at the interface of each section of the cast is not accounted for due to the small step that exists and possibly weaker gypsum bonding at the interface after casting. This region is local to the seam and there is no evidence of it being propagated downstream of the seam.

There was a third region of elevated mass transfer in the second elbow (Region III) slightly downstream of the second elbow entrance, between the inner side wall and inner wall. The location of this region is similar in all four elbow separation cases. The

high Sherwood number at this location can be attributed to the acceleration and swirl effect of the flow on the inner wall as it changes direction in the second elbow. The magnitude of this region decreases with increasing separation distances. This is not unexpected since the swirl effect lessens with increasing separation distance. The high mass transfer near the second elbow inner wall is consistent with the high flow velocity in this region in the flow measurements of [Murakami et al., 1969; Yuki et al., 2011]. Yuki et al. [2011] reported a maximum velocity as high as 1.9 times the mean velocity at this vicinity, with high levels of turbulence as well.

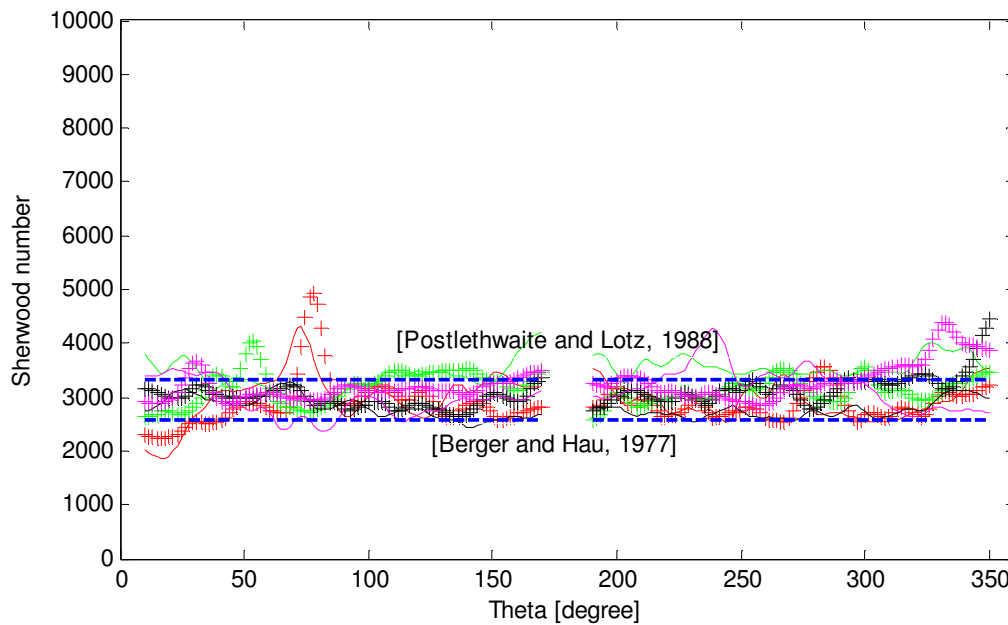


Figure 4.2: Typical azimuthal Sherwood number profiles in the upstream pipe for  $Re = 70,000$  and  $Sc = 1280$ . +  $z/D = -1$ , -  $z/D = -4$ , red  $L/D = 0$ , green  $L/D = 1$ , black  $L/D = 2$ , magenta  $L/D = 5$

The Sherwood number in the different regions was characterized by examining azimuthal profiles at key locations. The Sherwood number profiles at various locations along the upstream pipe shown in Figure 4.2 are uniform and similar for all four elbow separation cases. The results are compared with the smooth wall mass transfer correlation proposed by Berger and Hau [1977] given by

$$Sh = 0.0165Re^{0.86}Sc^{0.33}, \quad (4.1)$$

and the fully rough wall mass transfer correlation proposed by Postlethwaite and Lotz [1988] given by

$$Sh = 0.007Re^{0.96}Sc^{0.33} \quad (4.2)$$

The averaged pipe Sherwood number was approximately 3000, higher than the value from the smooth wall correlation of Berger and Hau [1977] and slightly lower than the result from the fully rough wall correlation of Postlethwaite and Lotz [1988]. The Sherwood number evaluated here is averaged between 2 to 6 diameters from the pipe inlet to avoid any inlet effect and elbow effect on the upstream pipe.

Azimuthal Sherwood number profiles at different locations along the second elbow for the different separation distances are plotted in Figure 4.3. Here, the azimuthal positions theta of  $0^\circ$  and  $\pm 180^\circ$  correspond to the intrados and the extrados of the elbow, respectively. Theta increases toward the inner side wall and decreases in the outer side wall direction. The high mass transfer in the separation pipe downstream of the first elbow (Region I) occurs at a location corresponding to the outer wall of the first elbow ( $\theta = -90^\circ$ ) at large separation distances of  $L/D = 5$  and 2. The Sherwood number of this

region remains unchanged when the separation distance was changed from  $L/D$  of 5 to 2 but there was a large increase in the Sherwood number of the second elbow centered around  $\theta=-35^\circ$ (Region II). This occurred in the latter half of the second elbow ( $\Phi=65^\circ$ ). For small separation distance of  $L/D = 1$ , the interaction between these two regions and the second elbow resulted in a wide high mass transfer area centered about  $\theta =-75^\circ$ . This occurs for  $\Phi =20^\circ$  to  $70^\circ$ . The second elbow curvature effect becomes greater at  $L/D$  of 0, shifting the single high mass transfer centered about  $\theta=-50^\circ$  towards the inner wall (Region II).

The maximum mass transfer on the intrados associated with the acceleration and turning of the flow in the second elbow (Region III) is narrow with a width of approximately  $20^\circ$  to  $40^\circ$  in the theta direction, inclined towards the midway ( $\Phi=45^\circ$ ) of the inner wall from the side wall entrance. This region shifted marginally away from the inner wall towards the inner side with increasing elbow separation distance. The maximum mass transfer in this region shifts upstream as the separation between the elbows increases. For small elbow separation distances the maximum occurs half way around the elbow ( $\Phi\sim 45^\circ$ ), while for larger elbow separation distance the maximum shifts toward the entrance ( $\Phi\sim 25^\circ$ ), approaching the mass transfer enhancement region near the inlet of single  $90^\circ$  elbows. In general, the size of the regions downstream of the first elbow outer wall is wider and longer but lower in magnitude compared to the region associated with the acceleration and turning of the flow in the second elbow intrados.

The maximum Sherwood number is estimated by examining the azimuthal profiles of the local mean Sherwood number in detail within the high mass transfer regio-



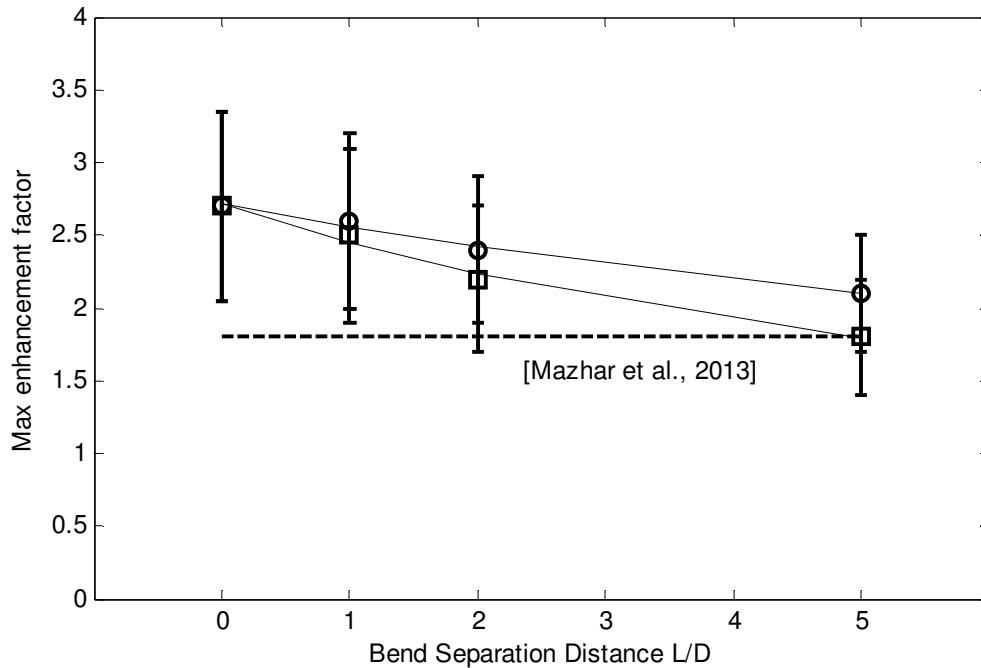


Figure 4.4: Maximum enhancement factor in the elbow relative to the upstream pipe Sherwood number for different elbow separation distances.  $\circ$  Region III,  $\square$  highest region downstream of first elbow

ns. The mass transfer enhancement factor (normalized by the value in the upstream pipe) for the two regions of highest mass transfer are plotted against the separation distance in Figure 4.4, giving a maximum enhancement factor in the second elbow of 2.7, decaying to 2.1 with increasing separation distances  $L/D$  of 0 to 5, compared to the enhancement factor of 1.8 for the first elbow. The mass transfer enhancement of the two highest regions is comparable at small elbow separation distance. At larger elbow separation distances, the enhancement associated with the outside of the first elbow is lower than that on the inside of the second elbow. The maximum mass transfer rate decays with increasing elbow separation distances. This can be attributed to the reduction in turbulence level with increasing distance downstream from the first elbow. The similarity

in magnitude of the mass transfer enhancement for  $L/D$  of 0 and 1 may be attributed to the fact that the flow structures remain relatively similar at short elbow separation distance [Murakami et al., 1969].

The surface topology in Figure 4.5 shows a difference in the roughness for the two separation distances. The surface roughness was characterized by subtracting the local wear from the local averaged result. The roughness of the inner side wall for the cases with  $L/D$  of 0 and 5 is shown in Figure 4.6. Well defined streaks are seen in both cases as well as deep pits. The deep pits are scallops that formed with tails pointing in the flow direction. The width and depth of these pits is on the order of 1.5mm and 0.2mm, respectively. The roughness height is estimated based on the valley to peak value by examining the surfaces in profile. The results for the different regions and different test times were characterized following a similar approach. The relative roughness at each region estimated at an experimental test time of 80 minutes is summarized in Table 4.1. The nominal relative roughness  $e/D$  in the upstream pipe is approximately 0.003-0.004. The nominal roughness increases with experimental test time but stays similar after 60 minutes. The roughness scale  $e^+ = eu^*/\nu$  in the upstream pipe region for the Reynolds number under consideration (70,000) is approaching the fully rough region [Postlethwaite and Lotz, 1988; Dawson and Trass, 1972]. The relative roughness in the second elbow decreased from 0.006 to 0.005 as  $L/D$  was increased from 0 to 5. The roughness levels in the second elbow are higher than the upstream pipe for all configurations and are about 1.5 times higher for the configuration with  $L/D$  of 0. The reduction in roughness is also associated with the reduction in mass transfer with increasing elbow separation distance.

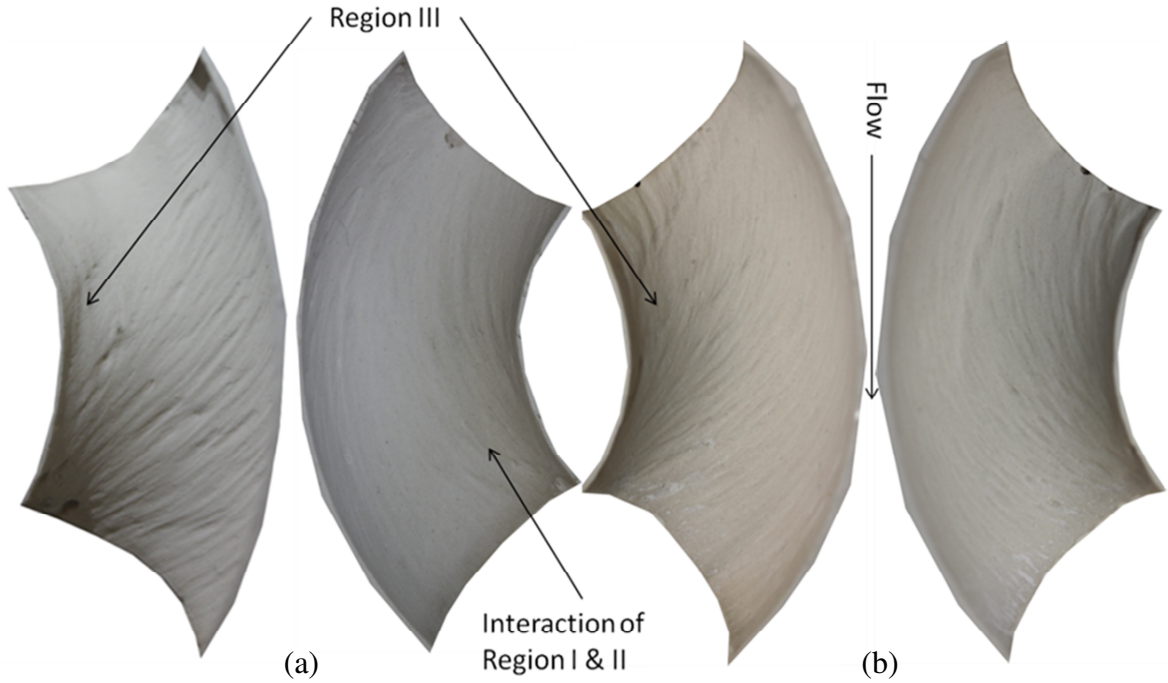


Figure 4.5: Typical surface topology of the second elbow for (a)  $L/D = 0$ , time = 80 minutes (b)  $L/D = 5$ , time = 80 minutes

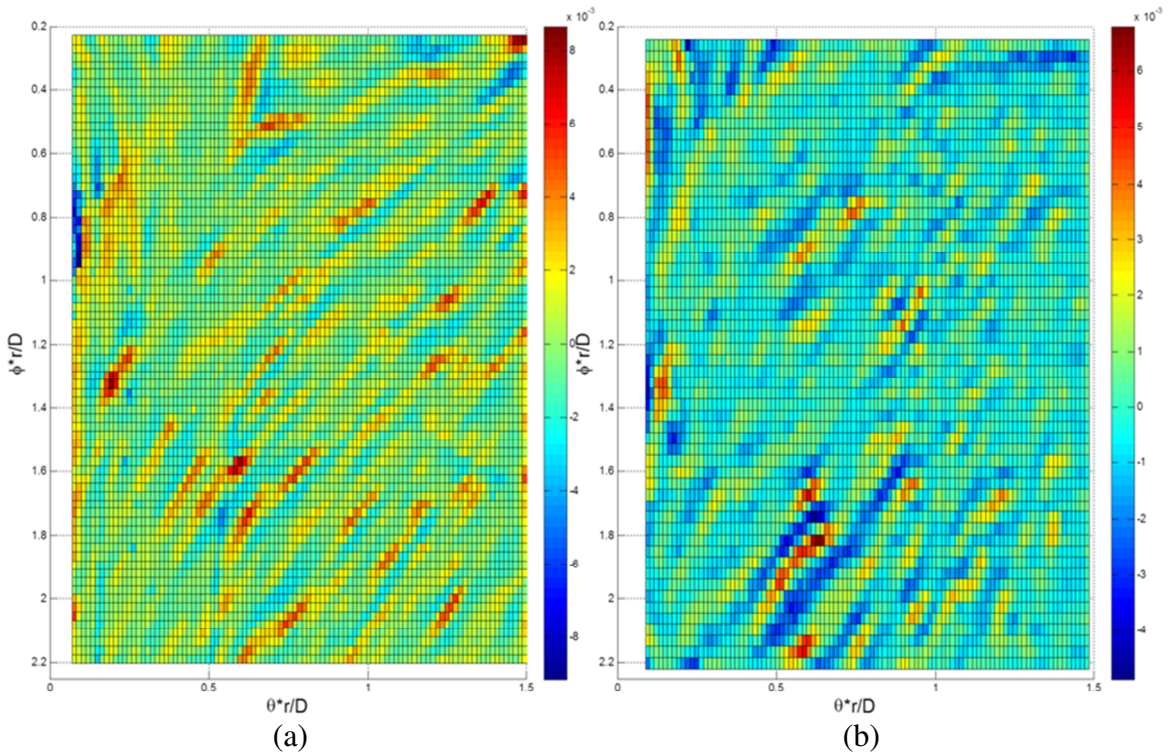


Figure 4.6: Typical relative roughness level of the second elbow inner side wall for (a)  $L/D = 0$ , time = 80 minutes (b)  $L/D = 5$ , time = 80 minutes

Table 4.1: Relative roughness level in the different regions for all elbow separation distances

Elbow separation distance ( $L/D$ )	Relative roughness level: $e/D$			
	Upstream Pipe	Second elbow inner side wall	Second elbow outer side wall	Separation pipe outer wall
0	$3.5 \times 10^{-3}$	$6 \times 10^{-3}$	$4 \times 10^{-3}$	--
1	$3 \times 10^{-3}$	$5 \times 10^{-3}$	$4 \times 10^{-3}$	$3 \times 10^{-3}$
2	$4 \times 10^{-3}$	$5 \times 10^{-3}$	$5 \times 10^{-3}$	$4 \times 10^{-3}$
5	$3.5 \times 10^{-3}$	$5 \times 10^{-3}$	$4 \times 10^{-3}$	$3.5 \times 10^{-3}$

## 4.2 Two-phase Flow Results

The effect of water and air superficial velocities on the distribution of the Sherwood number for the bends with a separation distance of 0 pipe diameters are shown in Figure 4.7. The Sherwood number distribution shows low and uniform mass transfer in the upstream pipe and high mass transfer on the outer wall of the first elbow. The high mass transfer in this region is similar to that observed by Poulson [1991] and Mazhar et al. [2013], and thought to be due to the impingement of liquid droplets entrained in the core gas flow. This region of high mass transfer is broad and circular, similar in size to the gas core when viewed from the upstream pipe. There is a narrower region of high mass transfer downstream of this region consistent with the results of Poulson [1991] and Mazhar et al. [2013]. This region extended to the exit of the first elbow and appears to extend into the second elbow particularly for air superficial velocities of 27.96 m/s and g-

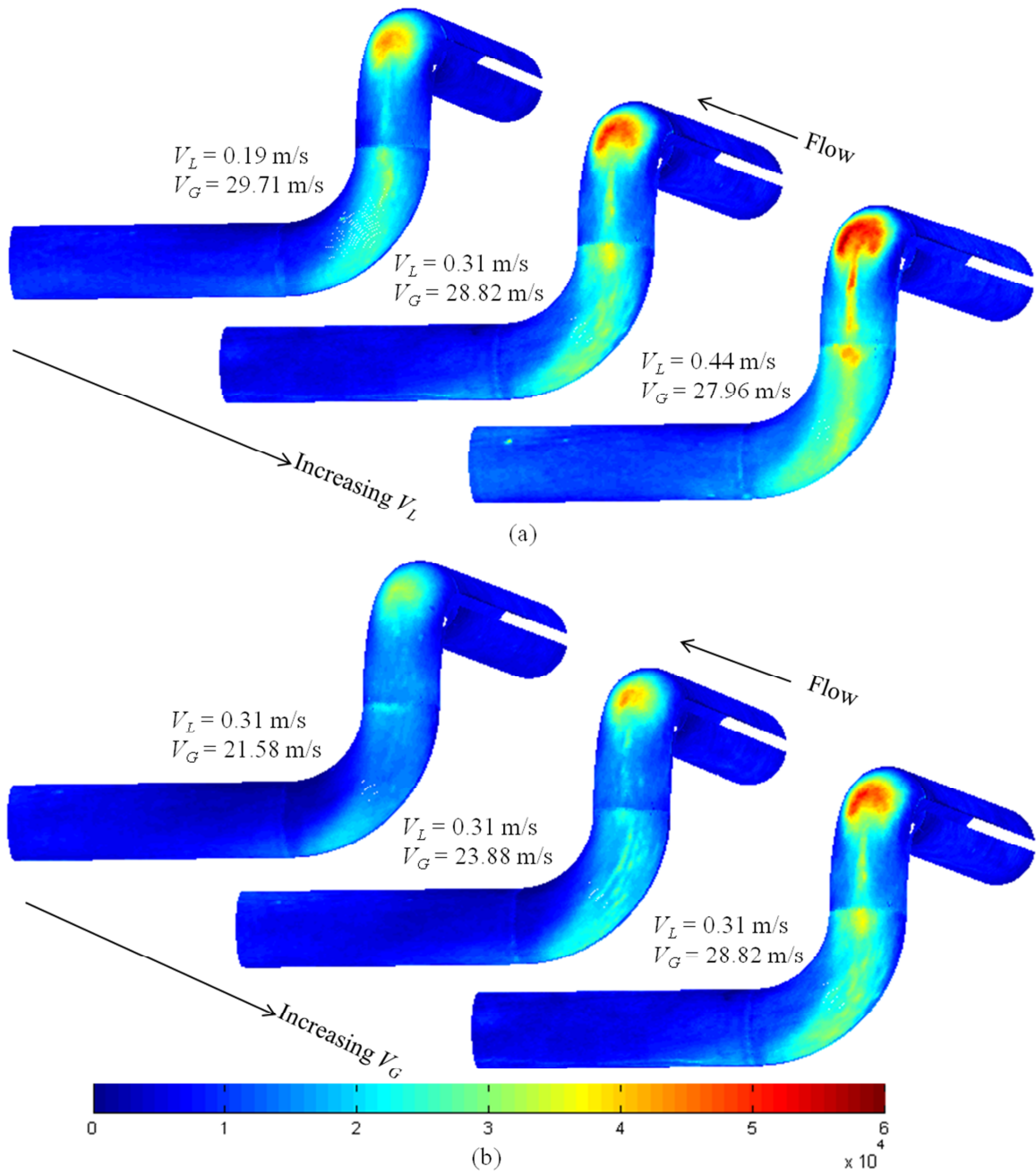


Figure 4.7: Effect of (a) water superficial velocity (b) air superficial velocity on the Sherwood number distribution

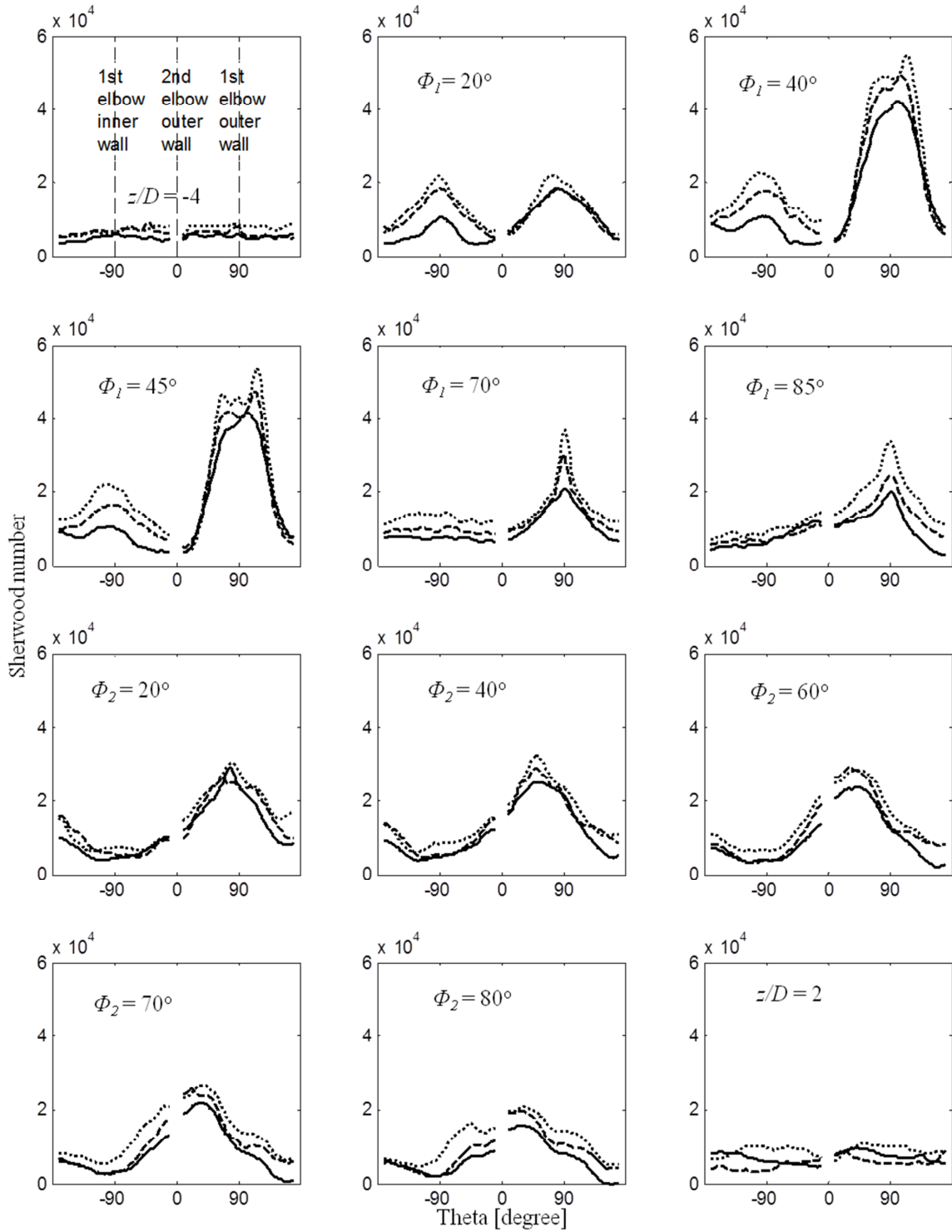


Figure 4.8: Azimuthal profiles of Sherwood number along the first and second elbow for increasing water superficial velocity: -  $V_L = 0.19$  m/s,  $V_G = 29.71$  m/s; --  $V_L = 0.31$  m/s,  $V_G = 28.82$  m/s; ...  $V_L = 0.44$  m/s,  $V_G = 27.96$  m/s

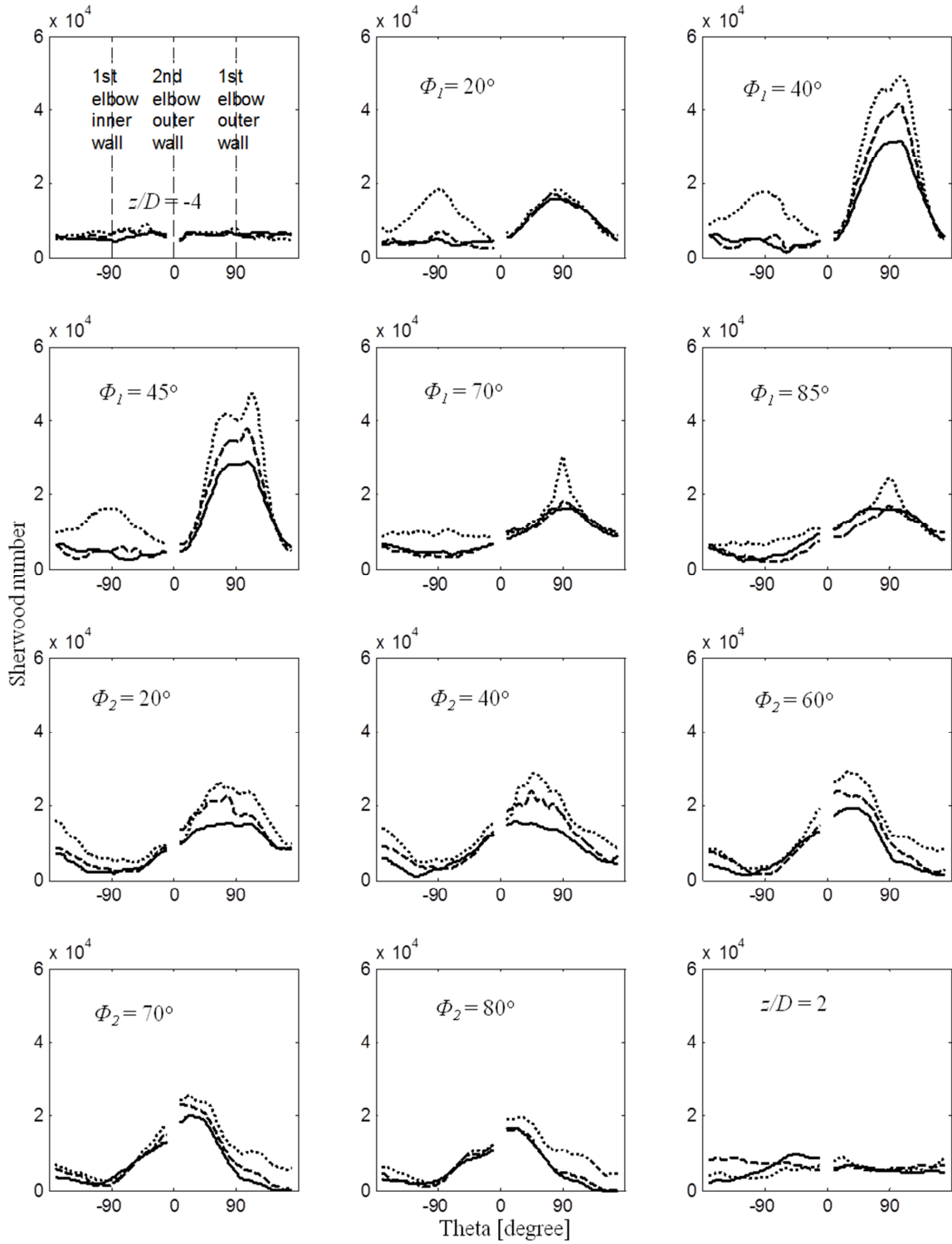


Figure 4.9: Azimuthal Sherwood number profile along the first and second elbow for increasing gas superficial velocity: -  $V_L = 0.31$  m/s,  $V_G = 21.58$  m/s; --  $V_L = 0.31$  m/s,  $V_G = 23.88$  m/s; ...  $V_L = 0.31$  m/s,  $V_G = 28.82$  m/s

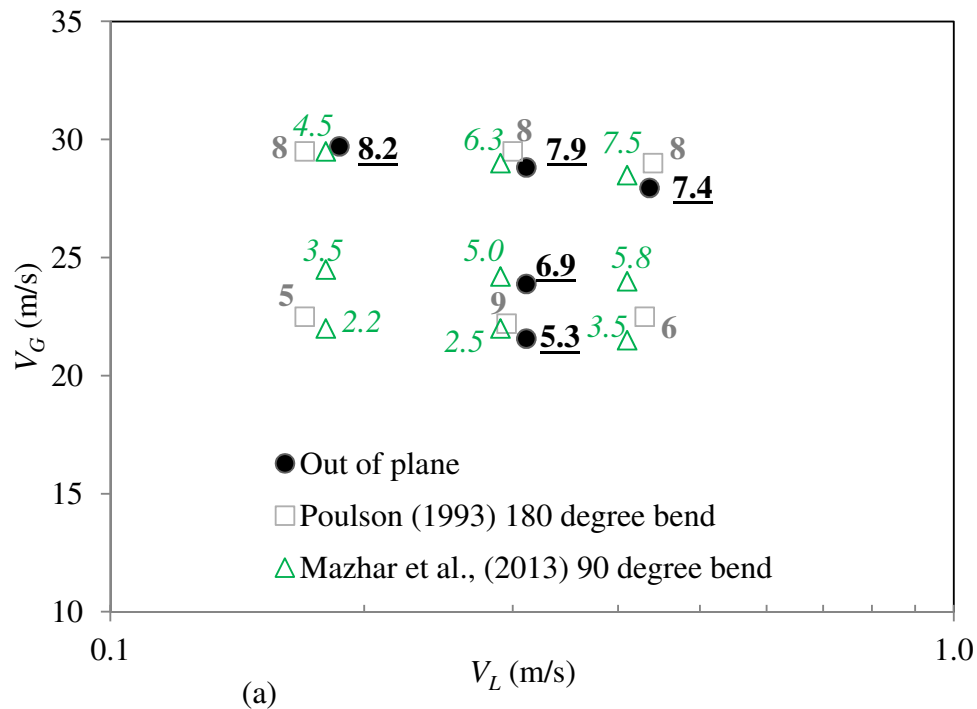
reater. The high mass transfer on the outer wall of the first elbow continued into the second elbow outer side wall and sweeps around towards the outer wall in the latter part of the second elbow due to curvature effect. The region is broad and long, extending from entrance to near the elbow exit. High mass transfer is not evident on the inner side wall of the second elbow.

Azimuthal profiles of the Sherwood number at different streamwise locations showing the effects of increasing water and air superficial velocities for the separation distance  $L/D$  of 0 are plotted in Figures 4.8 and 4.9, respectively. The mass transfer on the outer wall increases significantly and reaches a maximum value at an angle along the bend  $\Phi_1$  of  $40^\circ$  to  $45^\circ$  that approximately corresponds to the line of sight of the flow [Maddock et al., 1976; Poulson, 1991]. The region of high mass transfer is approximately  $90^\circ$  wide across the outer wall with a maximum that is slightly off center, consistent with the results of Mazhar et al. [2013]. The mass transfer on the inner wall of the first elbow increases near the entrance, reaching a maximum at approximately  $\Phi_1 = 20^\circ$  to  $30^\circ$  before decreasing to a level comparable to the pipe near the exit. There is a secondary narrow region of high mass transfer in the latter part of the first elbow that is lower compared to the liquid impingement location. This region extends into the second elbow particularly for air superficial velocity of 27.96 m/s and higher flow conditions but is lower than in the first elbow. There is also a broader underlying region of elevated mass transfer in the latter part of the first elbow that extends into the second bend and increases in magnitude resulting in a broad peak in the mass transfer in the second bend from an angle  $\Phi_2$  of approximately  $30^\circ$  to  $70^\circ$ . The breadth of this region (in the  $\theta$  direction) is approximately

90° but the center and maximum shifts from the side wall of the second bend that corresponds to the outer wall of the first bend ( $\theta = 80^\circ$ ) near the inlet toward the outer wall of the second bend, reaching  $\theta = 30^\circ$  in the latter part of the bend. Thus, the results suggest there may be two different mechanisms for mass transfer increase in the latter part of the first elbow and the second elbow. The narrow peak can be attributed to the entrainment of liquid from the inner wall by the gas core and deposition onto the latter part of the first elbow outer wall [Maddock et al., 1976; Da Silva Lima and Thome, 2012]. This narrow peak appears to extend into the second elbow for the out of plane bends considered here and may persist throughout a 180 degree bend. The broader peak is likely due to the combination of higher air velocity moving towards the second elbow outer side wall [Maddock et al., 1976] accelerating the near wall liquid, and waviness/breakup of thick liquid film observed at that location [Da Silva Lima and Thome, 2012].

The effect of both air and water superficial velocities on the high mass transfer regions are significant, with the air velocity having a greater effect. The mass transfer enhancement factors (maximum Sherwood number normalized by the corresponding value in the upstream pipe) for the different regions are shown in Figure 4.10. The results for the line of sight location in the first bend are compared to the result of Poulson [1993] for a 180 degree bend and Mazhar et al., [2013] for a 90 degree bend. Increasing the air superficial velocity from 21.58 m/s to 28.82 m/s increases the enhancement factor from 5.3 to 7.9 in agreement with the results of Poulson [1993]. The result at  $V_G = 22$  m/s and  $V_L = 0.3$  m/s from Poulson [1991] appears to be an outlier when all data is considered.

The change in enhancement with gas velocity was less than that reported by Mazhar et al. [2013]. The enhancement factors did not change significantly with water superficial velocity (from 0.19 m/s to 0.44 m/s) in agreement with Poulson [1991] and differing again from Mazhar et al. [2013]. The maximum Sherwood number in the first elbow is lower in comparison to the results of Mazhar et al. [2013] for a 90 degree bend. The change in the enhancement in the narrow region at the end of the first bend and start of the second bend in Figure 5b increases with either an increase in the gas superficial velocity or air superficial velocity, in agreement with Mazhar et al. [2013] though slightly different in magnitude. The enhancement factors for the second elbow shown in figure 5c followed a similar trend to the line of sight location in the first elbow. The maximum mass transfer in the second elbow is approximately 60 percent of the peak value measured



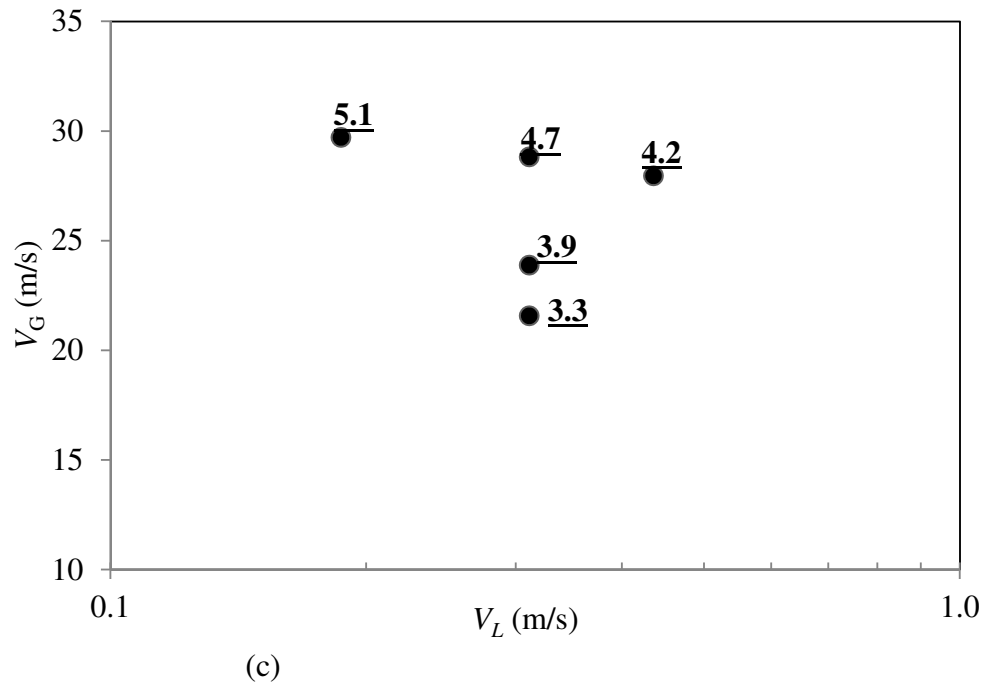
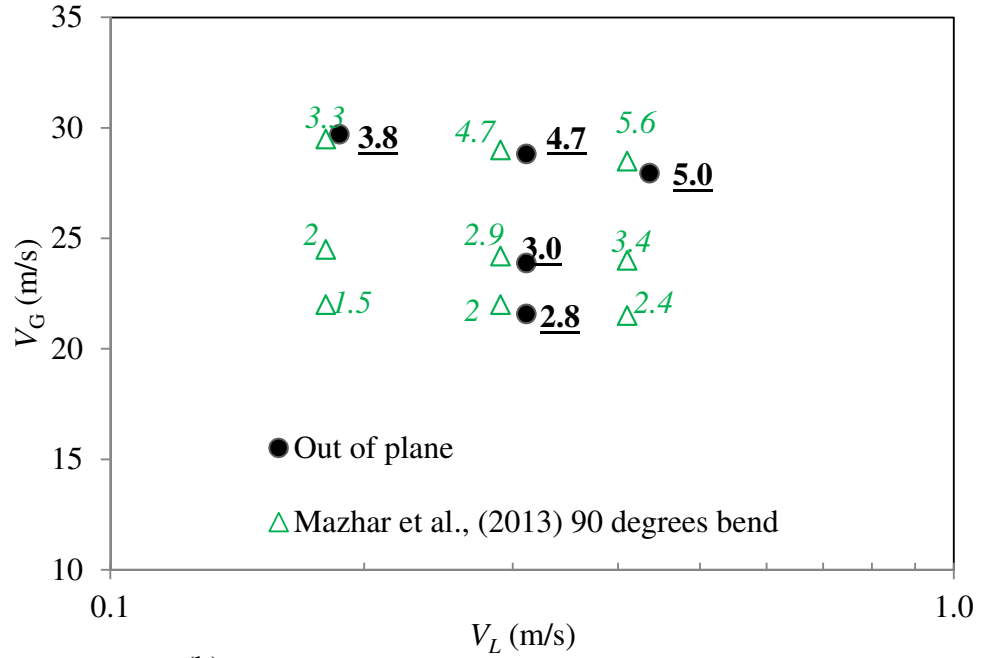


Figure 4.10: Effect of water and air superficial velocities on the mass transfer enhancement factor at (a) the line of sight in first elbow, (b) narrow peak in first elbow and (c) second elbow for separation distance  $L/D = 0$

in the first elbow outer wall. The change in the enhancement with air velocity appears slightly less than for the line of sight location and the enhancement appears to decrease with an increase in the water superficial velocity.

The Sherwood number distributions for the cases with different lengths of piping separating the bends are compared in Figure 4.11. The pipe between the elbows is oriented vertically downward. The mass transfer in the first elbow is similar with increasing separation distance. The narrow region of enhanced mass transfer in the latter part of the first bend and the broad underlying region do extend into the separation pipe for the bends with separation distances  $L/D$  of 1 and 5, but decrease as the flow evolves downstream towards the entrance of the second elbow, particularly for the bends with a separation distance  $L/D$  of 5. High mass transfer is not seen at the outer side wall of the second elbow entrance for the bends with a separation distance  $L/D$  of 5, but is present for the  $L/D$  of 0 and 1. The high mass transfer in the second elbow shifts slightly towards the outer wall and upstream with increasing separation distances. The azimuthal Sherwood number profile at different streamwise locations for the different cases is shown in Figure 4.12. The results show that the narrow maximum in the mass transfer present in the latter half of the first bend does not persist far into the separation pipe for the bends with separation distances of 1 or 5 diameters, whereas the broader underlying region does, suggesting the narrow and broad regions are caused by different mechanisms. The mass transfer in the broader region does decrease with downstream position in the pipe for the bends with the separation distance and there is only minimal evidence of this region four diameters downstream of the first bend. The maximum mass transfer location in the

second bend for the bends with a separation distance  $L/D$  of 5 occurs at approximately  $\Phi_2 = 40^\circ$  to  $60^\circ$  into the second elbow though the maximum occurs much closer to the outer wall of the second bend (only 10 to 30 from the outer wall). The maximum mass transfer rate in the second elbow for this case is comparable to the maximum for the bends with separation distances of  $L/D$  of 0, 1 suggesting that the mechanism causing the maximum mass transfer in the second bend is similar for the different cases. The maximum shifts towards the outer wall as the separation distance increases likely because the liquid and gas flow redistributes itself as the flow evolves downstream. The increase in the early part of the second bend for the shorter separation distance may reflect some effect of the flow from the first bend on the second bend.

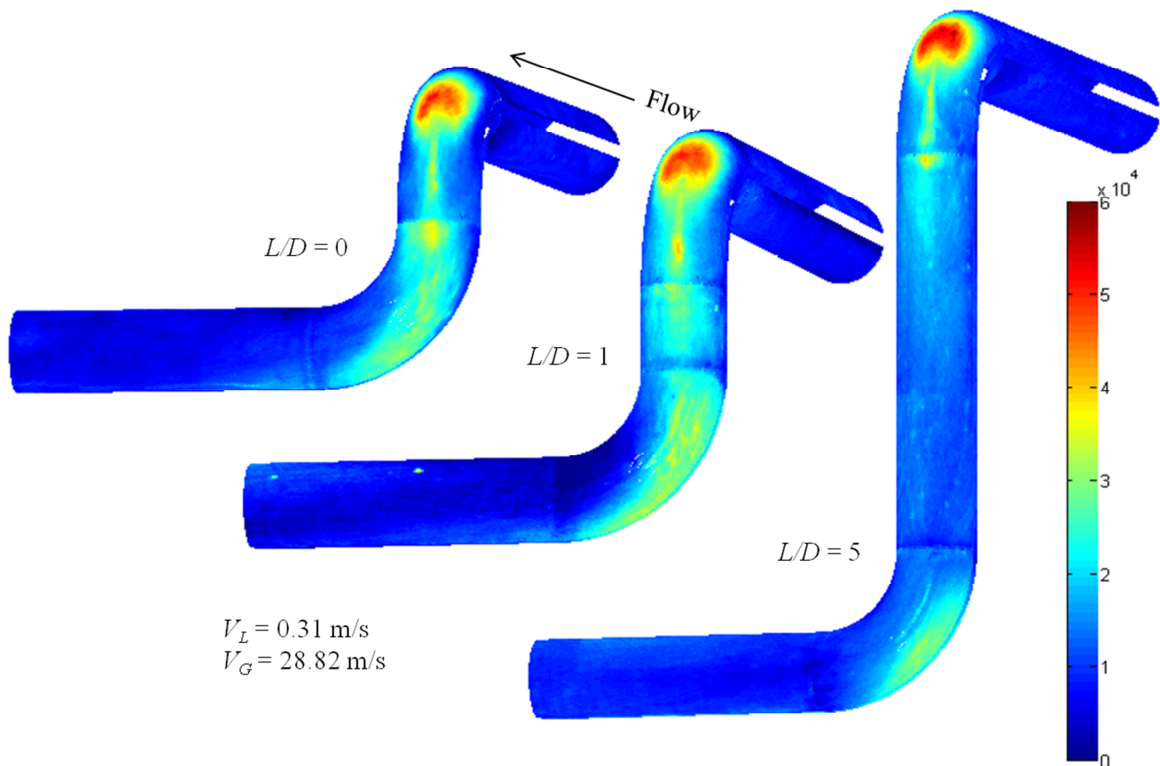


Figure 4.11: Effect of elbow separation distance  $L/D$  on the Sherwood number distribution

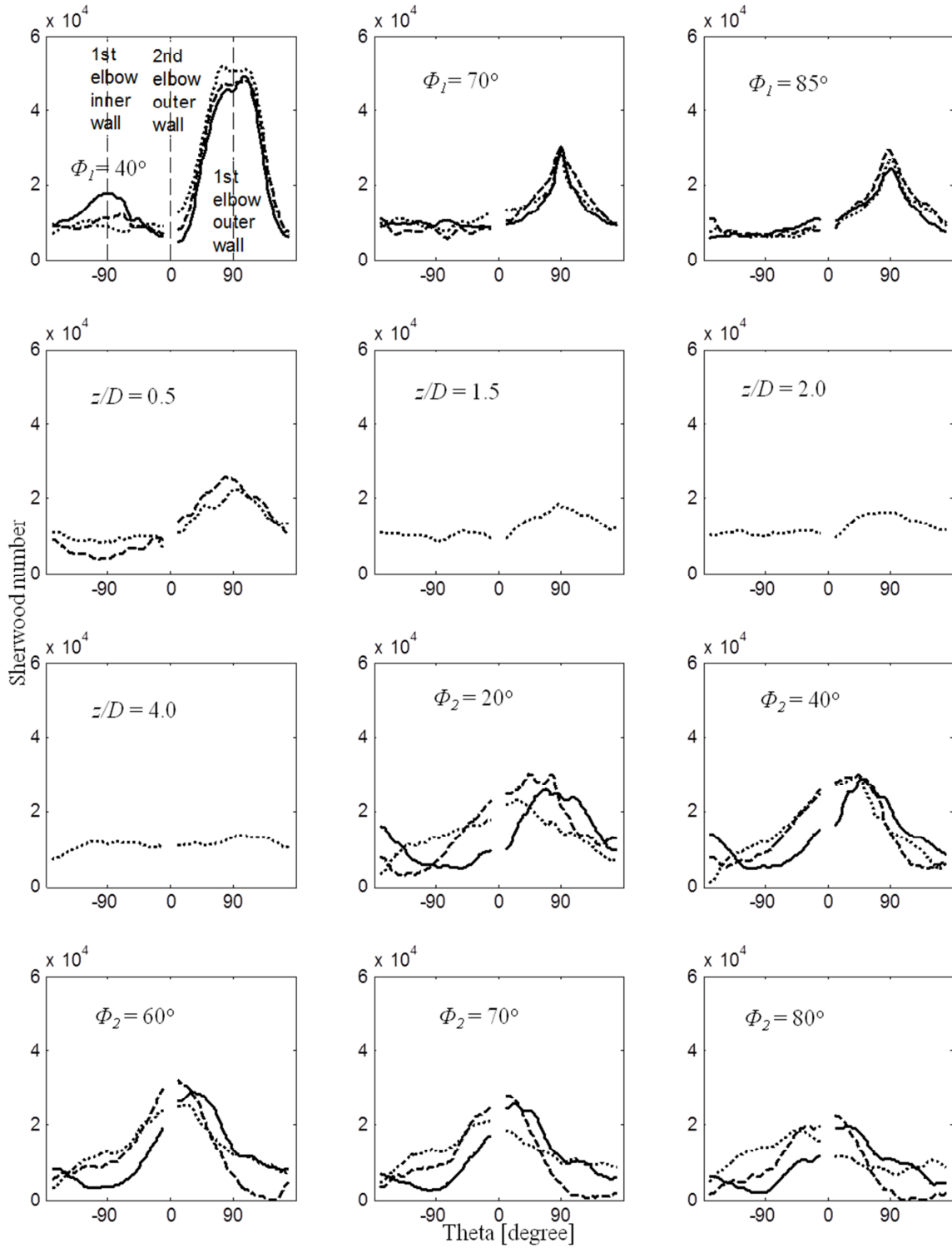


Figure 4.12: Azimuthal profiles of Sherwood number along the first and second elbow at  $V_L = 0.31$  m/s,  $V_G = 28.82$  m/s for elbow separation distance  $L/D$  of -0; -1; ... 5 ( $z/D$  is the distance downstream of exit of first elbow)

Table 4.2: Comparison of fully developed pipe mass transfer to heat transfer correlations for different annular two-phase flow conditions

Water (m/s)	0.19	0.31	0.31	0.31	0.44
Air (m/s)	29.71	21.58	23.88	28.82	27.96
Chu and Jones [1980]	2300	2300	2400	2600	2800
Dorresteijs [1970]	2600	2800	3000	3200	3800
Kudirka et al [1965]	2200	2200	2200	2300	2400
Ravipudi and Godbold [1978]	2200	2300	2400	2500	2700
Serizawa et al [1975]	2400	2500	2600	2900	3200
Groothuis and Hendaal [1959]	4000	3400	3600	4100	4300
Kim and Ghajar [2006]	3000	2600	2900	3600	4000
Elamvaluthi and Srinivas [1984]	4200	3600	3800	4300	4400
<b>Current results</b>	<b>5160</b>	<b>5870</b>	<b>6040</b>	<b>6220</b>	<b>7400</b>
Chen [1966]	16300	10000	11200	14100	12900
Knott et al [1959]	12700	10200	11000	12700	12800

A comparison of the pipe Sherwood number for the different flow conditions with typical correlations from literature are shown in Table 4.2. The Sherwood number in the upstream pipe, averaged between 2 to 6 diameters from the inlet, increases with increasing gas and water superficial velocity. However, the effect of increasing water superficial velocity is more significant. This is consistent with the heat transfer results of Kim and Ghajar [2006] who found the heat transfer coefficients correlated more strongly with liquid Reynolds number rather than gas Reynolds number in the annular flow regime. Only correlations with  $Pr^{0.33}$  dependence were selected for comparison due to the single-phase result that suggested  $Sc^{0.33}$  is applicable for smooth and rough mass transfer

applications [Berger and Hau, 1977; Postlethwaite and Lotz, 1988]. The model of Chisholm [1983] was used to compute the void fraction of the flow, based on test section inlet pressure. Most of the correlations predicted pipe Sherwood number in the range of 2000 to 4400, lower than the current result; however, a few including Chen [1966] predicted much higher Sherwood numbers. Poulson [1991] found good agreement with the correlation of Chen [1966] for low mass qualities typical of the cases considered here.

The mass transfer can be affected by the development of roughness during the process. This is particularly evident in single-phase flow [Wilkin et al., 1976; Poulson and Robinson, 1988]. Poulson [1991] found the surface in the two-phase experiment appeared smooth. The surface roughness at different locations along the pipe was characterized by subtracting the mean surface from the local surface. The roughness is estimated by examining the surfaces in profile to obtain valley to peak height. Typical surface relative roughness  $e/D$  in the upstream pipe and the first elbow outer wall is shown in Figure 4.13. The relative roughness in the pipe is approximately  $1.5 \times 10^{-3} - 2 \times 10^{-3}$ . This is much lower than the case for single-phase flow, consistent with the results of Poulson [1991] for a 180 degree bend. The relative roughness increased sharply to approximately  $6 \times 10^{-3}$  in the line of sight location. Small pits are seen, likely attributed to the impingement of liquid droplets, though these do not appear to be erosion due to repeatable results obtained from the experiment for  $V_G = 28.82$  m/s and  $V_L = 0.31$  m/s with an initial water bulk concentration of 46 percent of the wall concentration. The roughness decreased downstream of the maximum location, but is higher than in the upstream pipe. The results

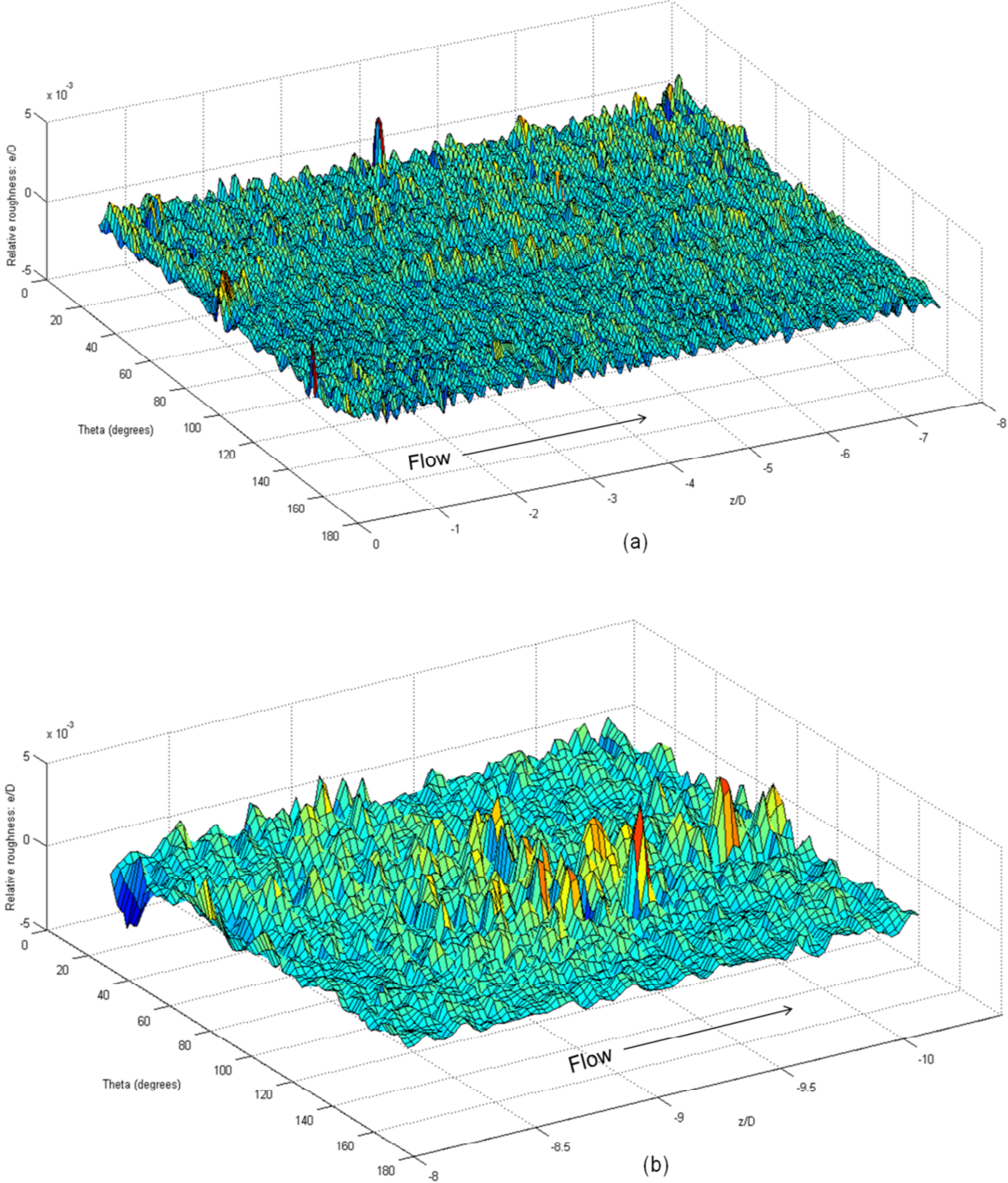


Figure 4.13: Typical surface relative roughness of (a) upstream pipe (b) first elbow outer wall

for different regions and flow conditions were characterized following a similar approach. The relative roughness results are tabulated in Table 4.3. The effect of roughness on heat and mass transfer is typically analyzed by looking at the roughness relative to the near wall scale,  $e^+ = eu^*/\nu$ . The skin friction for each case was estimated from the Lockhart-Martinelli [1949] separated flow correlation. The resulting values of  $e^+$  tabulated in Table 4.3 suggest the roughness in the pipe would be in the transition region for single-phase flow, while the high mass transfer region on the first and second elbow is likely fully rough [Dawson and Trass, 1972]. The increase in mass transfer for high  $Sc$  applications is much greater and also occurs at lower value of  $e^+ < 10$  [Dawson and Trass, 1972]. In this case, the calculated  $e^+$  for the pipe is in the range of 8 to 22 for the different flow conditions.

Table 4.3: Relative roughness of different location for the different annular two-phase flow conditions

Elbow separation distance	$V_L$ (m/s)	$V_G$ (m/s)	Pipe ( $e/D$ )	1 <sup>st</sup> elbow outer wall ( $e/D$ )	2 <sup>nd</sup> elbow ( $e/D$ )	Pipe $e^+$
$L/D = 0$	0.19	29.71	$2 \times 10^{-3}$	$6 \times 10^{-3}$	$4 \times 10^{-3}$	8
	0.31	21.58	$1.5 \times 10^{-3}$	$4 \times 10^{-3}$	$2.5 \times 10^{-3}$	13
	0.31	23.88	$1.5 \times 10^{-3}$	$4 \times 10^{-3}$	$6 \times 10^{-3}$	12
	0.31	28.82	$1.5 \times 10^{-3}$	$5 \times 10^{-3}$	$5 \times 10^{-3}$	11
	0.44	27.96	$2 \times 10^{-3}$	$6 \times 10^{-3}$	$5 \times 10^{-3}$	22
$L/D = 1$	0.31	28.82	$2 \times 10^{-3}$	$6.5 \times 10^{-3}$	$6 \times 10^{-3}$	15
$L/D = 5$	0.31	28.82	$2 \times 10^{-3}$	$6 \times 10^{-3}$	$3 \times 10^{-3}$	15

# Chapter 5 Conclusions and Recommendations

## 5.1 Conclusions

Mass transfer in back to back elbows arranged in an out of plane configuration under single-phase and annular two-phase flow was measured using a wall dissolving technique with bend sections cast from gypsum. The mass transfer was determined from the wear by flowing water for the single-phase and air-water for the two-phase, through the gypsum bend sections in a flow loop. The surface roughness was allowed to develop naturally from an initially smooth surface. The worn surface topology was digitized using a three dimensional laser scanner. The wear progression of the surface with time provided local mass transfer distribution and local surface roughness over the entire surface.

For the single-phase flow, experiments were performed at  $Re=70,000$  and  $Sc=1280$  for separation distances of 0, 1, 2 and 5 pipe diameters between the two elbows. The maximum mass transfer was on the second elbow when there was no separation distance between the elbows, with an enhancement factor of 2.7. The enhancement factor decreased to 2.1 as the separation distance increased from  $L/D$  of 0 to 5. For comparison,

the maximum enhancement factor on the first elbow was 1.8. Depending upon the separation distance between the out of plane back-to-back elbows, two to three regions of high mass transfer were identified:

- One region is downstream of the first elbow outer wall, consistent with the maximum location reported for single 90° elbows in the literature. The enhancement associated with the outside of the first elbow is lower than that on the inside of the second elbow at large separation distance.
- The second region is associated with the acceleration and turning of the flow in the second elbow intrados. A pattern of flow streaks on the second elbow surface indicated the formation of swirl flow, and its strength decreases with increasing separation distances.
- A third region was present in the second elbow for larger separation distances. The enhancement level of the two highest regions in the second elbow is comparable at short elbow separation distance, and both decay with increasing elbow separation distances.

Streak patterns on the second elbow surface suggest swirling flow. The angle of the streaks decreased with increasing elbow separation distance, indicating a reduction in swirl strength. The relative roughness  $e/D$  in the upstream pipe and the second elbow was evaluated. The upstream pipe relative roughness level was 0.003-0.004, close to the fully rough region under the tested Reynolds number. The relative roughness in the second

elbow is 1.5 times higher than the upstream pipe, and decreases with increasing elbow separation distance.

For the annular two-phase air-water flow conditions, the highest mass transfer occurs on the outer wall of the first elbow for all cases, likely due to the impingement of liquid droplet entrained within the gas core. The maximum mass transfer in the second elbow is approximately 60 percent of the maximum value in the first elbow, and is similar for different separation distances of 0, 1 and 5 pipe diameters between the two bends. The location of the maximum in the second elbow, however, changes with the separation distance. The highest mass transfer rate increases with increasing water and air superficial velocity, with the air velocity having a greater effect. The mass transfer in the pipe depends strongly on the water superficial velocity and less with air superficial velocity. The mass transfer enhancement factor over the pipe was relatively constant in the range 8.2 to 7.4 with increasing water superficial velocity from 0.19m/s to 0.44 m/s, while it increased from 5.3 to 7.9 with increasing air superficial velocity from 21.58m/s to 28.82m/s. The mass transfer results in the straight pipe were higher than those predicted by most heat transfer correlations, possibly due to the transition from smooth to rough wall in mass transfer applications as opposed to fully smooth walls in heat transfer. The pipe roughness in the two-phase flow was much lower compared to that in single-phase flows. However, the surface becomes significantly rougher, up to 5 times in the high mass transfer regions of first and second elbow.

## 5.2 Recommendations

The mass transfer under single-phase flow showed higher mass transfer in the second elbow in comparison to the first elbow. The maximum enhancement factor of the second elbow decreases when the separation distance  $L/D$  was increased from 0 to 5 pipe diameters. The mass transfer in the second elbow is expected to further decrease, approaching the result of a single 90 degree elbow with longer separation distances. Similarly, the mass transfer of the second elbow under annular two-phase flow is expected to recover to the result of a single 90 degree bend with increasing separation distances, though further investigation is needed to quantify the length of the separation pipe.

The surface roughness plays a strong role in the mass transfer under both single and two-phase flow, with greater effect in single-phase flow. Surface roughness was found to be higher in the regions of high mass transfer, though the enhancement in mass transfer of those regions associated with roughness is unclear. Further investigation in which roughness is defined as a direct input parameter to the mass transfer is needed to quantify its effect. Furthermore, the evolution of roughness is likely different in larger pipe diameters [Wang, 2012], and thus affect the mass transfer.

The orientation effect of the second elbow relative to the first in back to back elbows is not fully understood based on the result of the bends arranged in C, S and 90 degree out of plane configurations. Additional measurement in different relative angles

(e.g. 45 and 120 degree) is important to understand the angle effect. In addition, the Reynolds number effect on the mass transfer was not investigated in this study.

Thus, in summary, the recommendations for future work are:

- To perform mass transfer under single and annular two-phase flow for larger separation distances  $L/D$  of 10, 20 and 50 pipe diameters to quantify the relaxation/recovery in mass transfer of the second elbow.
- To perform mass transfer under single-phase flow with predefined roughness characteristics to quantify its effect on the enhancement of high mass transfer regions.
- To perform mass transfer in larger diameter piping sections to quantify the scaling effect of surface roughness and how the mass transfer might change as a result of different roughness.
- To perform mass transfer in different angles of the out of plane configuration to quantify the orientation effect of back to back elbows on mass transfer.
- To perform mass transfer experiments at higher Reynolds number to better define the Reynolds number effect on the mass transfer.

## List of References

- [1] Achenbach, E., 1976. Mass transfer from bends of circular cross section to air, *Future Energy Production Systems*, Academic Press, New York, Vol. 1, pp. 327-337
- [2] Berger, F. P., Hau, K. F. F. L., 1979. Local mass/heat transfer distribution on surfaces roughened with small square ribs, *International Journal of Heat and Mass Transfer*, Vol. 22, pp. 1645-1656
- [3] Berger, F. P., Hau, K. F. F. L., 1977. Mass transfer in turbulent flow measured by the electromechanical method, *International Journal of Heat Mass Transfer* 20, pp. 1185-1194
- [4] Brunton, J. H., Rochester, M. C., 1979. Erosion of solid surfaces by the impact of liquid drops, *Treatise on Materials Science and Technology*, Vol. 16, Erosion, C. M. Preece, Ed., New York, Academic Press, 1979, pp. 185-248
- [5] Chen, J. C., 1966. Correlation for boiling heat transfer to saturated fluids in convective flow, *Industrial & Engineering Chemistry Process Design and Development*, Vol. 5, pp. 322-329
- [6] Chen, X., Ewing, D., Ching, C. Y., Mass transfer in back to back elbows arranged in an C configuration, Unpublished
- [7] Chilton, T. H., Colburn, A. P., 1934. s.l.: *Ind. Engineering Chem.*
- [8] Chisholm, D., 1978. Influence of pipe surface roughness on friction pressure gradient during two-phase flow, *Journal of Mechanical Engineering Science*, Vol. 20, pp. 353-354
- [9] Chisholm, D., 1983. Two-phase flow in pipelines and heat exchangers. In: George Godwin in (ed.), London and New York in association with the Institution of Chemical Engineers, New York.
- [10] Christoffersen, J., Christoffersen, M., 1976. The kinetics of dissolution of calcium sulphate dihydrate in water, *Journal of Crystal Growth*, Vol. 35, pp. 79-88

- [11] Coleman, H. W., Steele, W. G., 1999. Experimentation and uncertainty analysis for engineers, 2<sup>nd</sup> Ed., John Wiley & Sons, New York
- [12] Coney, M. W. E., 1980. Erosion corrosion: the calculation of mass transfer coefficients, CEGB Report RD/L/N197/80, Central Electricity Research Laboratories
- [13] Da Silva Lima, J. R., Thome, R. J., 2012. Two-phase flow patterns in U-bends and their contiguous straight tubes for different orientations, tube and bend diameters, International Journal of Refrigeration, 35, pp. 1439-1454
- [14] Dawson, D. A., Trass, D., 1972. Mass transfer at rough surfaces, International Journal of Heat and Mass Transfer 15, pp. 1317-1336
- [15] Dooley, R. B., 2008. Flow-accelerated corrosion in fossil and combined cycle/HRSG plants, PPCHEM, pp. 68-89
- [16] El-Gammal, M., Mazhar, H., Cotton J.S., Schefski, C., Pietralik, J., Ching, C.Y., 2010. The hydrodynamics effects of single-phase flow on flow accelerated corrosion in a 90-degree elbow, Nuclear Engineering Design 240, pp. 1589-1598
- [17] Fiedler, H. E., 1997. A note on secondary flow in bends and bend combinations, Experiments in Fluids 23, pp. 262-264
- [18] Frank, W. M., 2006. Viscous fluid flow, New York: McGraw-Hill
- [19] Heymann, F. J., 1969. High speed impact between a liquid drop and a solid surface, Journal of Applied Physics, Vol. 40, no. 13
- [20] Heymann, F. J., 1970. Toward quantitative prediction of liquid impact erosion, ASTM STP474, pp. 212-248
- [21] Incropera, F. P., Dewitt, D. P., 1985. Fundamentals of heat and mass transfer, New York: John Wiley and Sons
- [22] Kim, D., Ghajar, A. J., Dougherty, R. L., Ryali, V. K., 1999. Comparison of 20 two-phase heat transfer correlations with seven sets of experimental data, including flow pattern and tube inclination effects, Heat Transfer Engineering, Vol. 20, pp. 15-40

- [23] Kim, J., and Ghajar, A. J., 2006, A general heat transfer correlation for non-boiling gas-liquid flow with different flow patterns in horizontal pipes, *International journal of Multiphase Flow*, 32, pp. 447-465
- [24] Liu, S. T., Nancollas, G. H., 1971. The kinetics of dissolution of calcium sulphate dihydrate, *Journal of Inorganic and Nuclear Chemistry*, pp. 2311-2316
- [25] Lockhart, R.W., Martinelli, R. C., 1949. Proposed correlation of data for isothermal two-phase two-component flow in pipes, *Chem. Eng. Prog.* 45, pp. 39-48
- [26] Lolja, S. A., 2005. Momentum and mass transfer on sandpaper-roughened surfaces in pipe flow, *International Journal of Heat and Mass Transfer*, Vol. 48, pp. 2209-2218
- [27] Maddock, C., Lacey, P.M.C., Patrick, M.A., The structure of two-phase flow in a curved pipe, *Symposium on Multiphase Flow Systems*, 1974, Institution of Chemical Engineers Symposium, University of Strathclyde.
- [28] Mazhar, H., Ewing, D., Cotton, J. S., Ching, C. Y., 2013. Experimental investigation of mass transfer in 90° pipe bends using a dissolvable wall technique, *International Journal of Heat and Mass Transfer*, Vol. 65, pp. 280-288
- [29] Mazhar, H., Ewing, D., Cotton, J. S., Ching, C. Y., 2013. Mass transfer in single bends under annular two-phase flow conditions, *International Journal of Heat and Mass Transfer* (submitted)
- [30] Mazhar, H., Ewing, D., Cotton, J. S., Ching, C. Y., Mass transfer in back to back elbows arranged in an S configuration, Unpublished
- [31] Murakami, M., Shimizu, Y., Shiragami, H., 1969. Studies on fluid flow in three-dimensional end conduits, *Bulletin of JSME*, 12 (54), pp. 1375-1379.
- [32] Pecherkin N. and Chekhovich V., 2011, "Mass Transfer in Two-Phase Gas-Liquid Flow in a Tube and in Channels of Complex Configuration" 155, Chapter 8, *Mass transfer in multiphase systems and its applications*
- [33] Postlethwaite. J., Lotz. U., 1988. Mass transfer at erosion-corrosion roughened surfaces, *The Canadian Journal of Chemical Engineering*, Vol. 66

- [34] Poulson, B., 1983. Electrochemical measurement in flow solutions, *Corrosion Science*, Vol. 23, pp. 391-430
- [35] Poulson, B., 1991. Measuring and modeling mass transfer at bends in annular two-phase flow, *Chemical Engineering Science*, Vol. 46, pp. 1069-1082
- [36] Poulson, B., 1993, Advances in understanding hydrodynamic effects on corrosion, *Corrosion Science* 35, no. 1-4, pp. 655-665.
- [37] Poulson, B., 1999. Complexities in predicting erosion corrosion, *Wear*, 233-235, pp. 497-504.
- [38] Poulson, B., 2007. Predicting flow accelerated corrosion, *Proceedings from the 13<sup>th</sup> International Conference on Environmental Degradation of Materials in Nuclear Power Systems*,
- [39] Poulson, B., Robinson, R., 1988. The local enhancement of mass transfer at 180° bends, *International Journal of Heat and Mass Transfer*, 31, No. 6, pp. 1289-1297
- [40] Raboian, R., 1986. *Electrochemical techniques for corrosion engineering*, Houston: National Association of Corrosion Engineers, ISBN 0-915567-23-7
- [41] Rizk, T. Y., Thompson, G. E., Dawson, J. L., 1996. Mass transfer enhancement associated with sudden flow expansion, *Corrosion Science*, pp. 1801-1814
- [42] Robinson, R. A., Stokes, R. H., 1968. *Electrolyte Solutions*, 2<sup>nd</sup> Rev. Edit., Butterworths, London
- [43] Runchal, A. K., 1971. Mass transfer investigation in turbulent flow downstream of sudden enlargement of a circular pipe for very high Schmidt numbers, *International journal of heat and mass transfer*, pp. 781-792
- [44] Sparrow, E.M., Chaboki, A., 1984. Swirl-affected turbulent fluid flow and heat Transfer in a circular tube, *Journal of Heat Transfer*, Vol. 106, pp. 766-774
- [45] Sparrow, E.M., Chrysler, G.M., 1986. Turbulent flow and heat transfer in bends of circular cross section: I—Heat transfer experiments, *Journal of Heat Transfer*, 108, pp. 40-48

- [46] Tagg, D. J., Patrick, M. A., Wragg, A. A., 1979. Heat and mass transfer downstream of abrupt nozzle expansions in turbulent flow, *Trans IchemE*, pp. 176-181
- [47] Thebault, Y., Guibert, F., Moulart, P., Garnier, R., Calonne-Chatelee, V., 2008. The contribution of the metallurgical examinations to the FAC damage diagnostics, *International FAC Conference on Flow Accelerated Corrosion*, Lyon, France
- [48] Tkaczyk, P. M., Morvan, H. P., 2011. Film thickness prediction in an annular two-phase flow around C-shaped bend, *Journal of Computational Multiphase Flows*. Vol. 3, pp. 27-39
- [49] Usui, K., Aoki, S., Inoue, A., Flow behavior and pressure drop of two-phase flow through C-shaped bend in vertical plane (I) upward flow, *Journal of Nuclear Science and Technology*, 1980, 17, 875-887
- [50] Villien, B., Zheng, Y., Lister, D., 2001. The scalloping phenomenon and its significance in flow assisted-corrosion. *Twenty Sixth Annual CNS-CAN Student Conference*
- [51] Villien, B., Zheng, Y., Lister, D., 2005. Surface dissolution and the development of scallops, *Chemical Engineering Communications*, Vol. 192, pp. 125-136
- [52] Wang, D., 2012. Characterization of local mass transfer rate downstream of an orifice, *Masc. thesis, McMaster University, Hamilton, Canada*
- [53] Wilkin, S.J., Oates, H.S., Coney, M.W.E., 1983. Mass transfer in straight pipes and 90° bends measured by the dissolution of plaster, *Technology Planning and Research Division, Central Electricity Research Laboratories*
- [54] Yilmaz. M., Comakli, O., Yapici, S., 1999. Enhancement of heat transfer by turbulent decaying swirl flow, *Energy Conversion & Management*, 40, pp. 1365-1376

- [55] Yuki, K., Hasegawa, S., Sato, T., Hashizume, H., Aizawa, K., Yamano, H., 2011. Matched refractive-index PIV visualization of complex flow structure in a three-dimensionally connected dual elbow, *Nuclear Engineering and Design*, pp. 1589-1598
- [56] Zhao, W., Trass, O., 1997. Electrochemical mass transfer measurements in rough surface pipe flow: geometrically similar V-shaped grooves, *International Journal of Heat and Mass Transfer*, Vol. 40, pp. 2785-2797

# Appendix

MATLAB data reduction codes written for the analysis of mass transfer in back to back elbows arranged in an out of plane configuration. The codes accomplish the followings:

- (1) Data gridding of point cloud
- (2) Coordinate system alignment based on axisymmetric flow of upstream pipe  
(adapted from Wang (2012))
- (3) Alignment based on deviation (adapted from Wang (2012))
- (4) Mass removed calculation
- (5) Sherwood number calculation

```
%%%%%%%%%%%%%%%%%%%%%%%%%%%%%%%%%%%%%%%%%%%%%%%%%%%%%%%%%%%%%%%%%%%%%%%%%DATA GRIDDING%%%%%%%%%%%%%%%%%%%%%%%%%%%%%%%%%%%%%%%%%%%%%%%%%%%%%%%%%%%%%%%%%%%%%%%%%
%this program grids the pipe surface point cloud
%input:
%pipe surface point cloud
%user defined grid cell size
%output:
%gridded pipe surface

%clear memory
clear
clc
close all

%initiate timer
tic

%reads in point cloud
PC = dlmread('pointcloud.txt');

%setting the number of grids in the circumferential and axial direction
noCir = input('Enter the number of grids in the circumferential
direction: ');
thetaStr = input('Enter the starting angle: ');
noAxial = input('Enter the number of grids in the axial direction: ');
zStr = input('Enter the starting z/D location: ');
zEnd = input('Enter the ending z/D location: ');

delZ = (-zEnd+zStr)/noAxial;
thetaEnd = 180 - thetaStr;
delTheta = (thetaEnd-thetaStr)/noCir;
%nominal pipe diameter
PipeR = 0.5;

dt = delTheta/2;
dz = delZ/2;
```

```

xCart = PC(:,1);
yCart = PC(:,2);
zCart = PC(:,3);

r = sqrt(xCart.^2 +yCart.^2);
theta = acosd(xCart./r);

%constructing the interpolant
F = TriScatteredInterp(zCart,theta,r,'natural');

%formulate z gridding matrix
zGrid = zeros(noAxial,noCir);
for i = 1:noCir
    zGrid(:,i) = linspace(zStr,zEnd,noAxial)';
end

%formulate theta gridding matrix
thetaGrid = zeros(noAxial,noCir);
for i = 1:noAxial
    thetaGrid(i,:) = linspace(thetaStr,thetaEnd,noCir);
end

%interpolating the radius using the natural neighbor interpolation
radius = F(zGrid,thetaGrid);

%interpolating the radius by averaging the radius within the grid cell
%zGrid+dz and thetaGrid+dt
for i = 1:noAxial
    for j = 1:noCir
        ind = find(zGrid(i,j)-dz<=zCart & zCart<=zGrid(i,j)+dz &
thetaGrid(i,j)-dt<=theta & theta<=thetaGrid(i,j)+dt);
        if ind > 0
            r_ave(i,j) = sum(r(ind))/length(ind);
        else
            r_ave(i,j) = radius(i,j);
        end
    end
end

%translating 2 dimensional matrixes into vector
zVect = reshape(zGrid',noAxial*noCir,1);
thetaVect = reshape(thetaGrid',noAxial*noCir,1);
wearVect = reshape((radius-PipeR)',noAxial*noCir,1);
aveWearVect = reshape((r_ave-PipeR)',noAxial*noCir,1);

outputPC = [thetaVect, zVect, aveWearVect];

dlmwrite('GriddedData.txt', outputPC,'delimiter','\t','newline','pc');

%translating gridded data to Cartesian coordinates
x_ave = cosd(thetaGrid).*r_ave;
y_ave = sind(thetaGrid).*r_ave;

```

```

z = zGrid;
toc

%%%%%%%%%%%%%%%%%%%%%%%%%%%%%%%%%%%%%%%%%%%%%%%%%%%%%%%%%%%%%%%%%%%%%%%%%%PIPE ALIGNMENT%%%%%%%%%%%%%%%%%%%%%%%%%%%%%%%%%%%%%%%%%%%%%%%%%%%%%%%%%%%%%%%%%%%%%%%%%%
%adapted from Wang(2012)
%this program aligns the coordinate system of the test section based on
axisymmetric flow in the upstream pipe
%input:
%gridded surface of the upstream pipe 2 to 6 diameters from the pipe
entrance
%original pipe surface point cloud
%output:
%aligned point cloud

PipeR = 0.5;
PipeRCur = 1.5;

%load original point cloud
load 'PC.txt'
cartX_org = PC(:,1);
cartY_org = PC(:,2)+PipeRCur;
cartZ_org = PC(:,3);

%load gridded pipe surface 2 to 6 diameters from pipe entrance
load 'pipe.txt'
pipeMat = single(pipe);
noCir = input('Enter the number of angle subdivisions: ');
noAxial = length(pipeMat)/noCir;
zMat = reshape(pipeMat(:,2), noCir,noAxial)';
zLine = zMat(:,1);
thetaLine = pipeMat(:,1)/180*pi;
thetaMat = reshape(thetaLine, noCir, noAxial)';
zLine = zMat(:,1);
deltas = reshape(pipeMat(:,3),noCir,noAxial)';

%number of lines used for coordinate system correction
lines = 30;
%setting the starts and ends line of region C
yStr = floor((noCir-lines)/2);
yEnd = yStr + lines;
%max number of iterations
nIter = 30;
%setting iterations criteria
barSlope = 0.0001;
barShift = 0.001;
%initiating offset
lineSlope = barSlope + 0.01;
lineShift = barShift + 0.01;

%evaluating offset of coordinate system in x and y direction
counting = 0;
while (counting <
nIter)&&((abs(lineSlope)>barSlope)|| (abs(lineShift)>barShift))
    counting = counting +1;

```

```

%calculation of coordinate system offset in x
for n = 1:noAxial
    sum = 0;
    for m = 1:lines
        sum = sum + (deltas(n,m) - deltas(n,noCir-
m+1))/cos(thetaMat(n,m));
    end
    localShiftx(n,1) = sum/2/lines;
    %average shift at each z location
end
shiftCondX = localShiftx(1:noAxial);
zCond = zLine(1:noAxial);

%calculate the slope of the correction by linear best fit
px = polyfit(zCond, shiftCondX,1);
bestfitX(counting,:) = px;
lineSlopex = px(1,1);
lineShiftx = px(1,2);

anglex = atand(lineSlopex);
fitValx = polyval(px, zCond);

rs = deltas + PipeR;
%alignment of coordinate points
cartX = rs.*cos(thetaMat)-zMat.*(lineSlopex) - lineShiftx;
cartY = -rs.*sin(thetaMat);
cartZ = zMat*(1 + abs(cos(lineSlopex)*tan(lineSlopex)));
%approximately cartZ = zMat
zLine = cartZ(:,1);

%updating theta and surface wear
thetaMat = -atan(cartY./cartX);
%angle theta should be positive from 0 to 180
ind = find(thetaMat<0);
thetaMat(ind) = thetaMat(ind)+pi;
zMat = cartZ;
deltas = sqrt(cartX.^2 + cartY.^2)-PipeR;

%alignment of original point cloud
cartX_alg = cartX_org.*cos(anglex*pi/180) -
cartZ_org.*(anglex*pi/180) - lineShiftx;
cartY_alg = cartY_org;
cartZ_alg = cartX_org.*sin(anglex*pi/180) +
cartZ_org.*cos(anglex*pi/180);
%setting original points to be the aligned points
cartX_org = cartX_alg;
cartY_org = cartY_alg;
cartZ_org = cartZ_alg;

subplot(1,2,1)
plot(-zLine,localShiftx,':r',-zLine,fitValx,'b')
title('Shift in X direction')
xlabel('Z/D downstream')
ylabel('Wear/D')

```

```

set(gcf, 'color', 'white')

% calculation of coordinate system offset in y
for n = 1:noAxial
    sum = 0;
    for m = 1:lines
        sum = sum + (deltas(n,m) + deltas(n,noCir-m+1));
    end
    aveWear = sum/2/lines;    %average wear at each Z location

    sum = 0;
    for m = yStr:yEnd
        sum = sum + (deltas(n,m)-aveWear)/sin(thetaMat(n,m));
    end
    localShifty(n,1) = sum/lines;
end

shiftCondY = localShifty(1:noAxial);
zCond = zLine(1:noAxial);

%calculate the slope of the correction by linear best fit
py = polyfit(zCond, shiftCondY,1);
bestfitY(counting,:) = py;
lineSlopey = py(1,1);
lineShifty = py(1,2);

angley = -atand(lineSlopey);
fitValy = polyval(py, zCond);

rs = deltas + PipeR;
%alignment of coordinate points
cartX = rs.*cos(thetaMat);
cartY = -(rs.*sin(thetaMat)-zMat.*(lineSlopey) - lineShifty);
cartZ = zMat.*(1 + abs(cos(lineSlopey)).*tan(lineSlopey));
%approximately cartZ = zMat
zLine = cartZ(:,1);

%updating theta, z and wear
thetaMat = -atan(cartY./cartX);
%angle theta should be positive from 0 to 180
ind = find(thetaMat<0);
thetaMat(ind) = thetaMat(ind)+pi;
zMat = cartZ;
deltas = sqrt(cartX.^2 + cartY.^2)-PipeR;

%alignment of original point cloud
cartY_alg = cartY_org.*cos(angley*pi/180) -
cartZ_org.*(angley*pi/180) + lineShifty;
cartX_alg = cartX_org;
cartZ_alg = cartY_org.*sin(angley*pi/180) +
cartZ_org.*cos(angley*pi/180);

cartX_org = cartX_alg;

```

```

cartY_org = cartY_alg;
cartZ_org = cartZ_alg;

subplot(1,2,2)
plot(-zLine,localShifty,':r',-zLine,fitValy,'b')
title('Shift in Y direction')
xlabel('Z/D downstream')
ylabel('Wear/D')

end
bestfitXFinal = [cumsum(bestfitX(:,1)) cumsum(bestfitX(:,2))];
bestfitYFinal = [cumsum(bestfitY(:,1)) cumsum(bestfitY(:,2))];

%calculate the rotation about x and y axis
angleRotx = atand(bestfitYFinal(1,1));
angleRoty = atand(bestfitXFinal(1,1));
lineshiftx = bestfitXFinal(1,2);
lineShifty = bestfitYFinal(1,2);

%output processed data for further calculations
thetaLine = thetaMat'(:)*180/pi;
zLine = zMat'(:);
deltaLine = deltas'(:);

dlmwrite('PC_aligned.txt',[cartX_alg, cartY_alg-
PipeRCur, cartZ_alg], 'delimiter', '\t', 'newline', 'pc')

%%%%%%%%%%%%%%%%%%%%%%%%%%%%%%%%%%%%%%%%%%%%%%%%%%%%%%%%%%%%%%%%%%%%%%%%%DEVIATION ALIGNMENT%%%%%%%%%%%%%%%%%%%%%%%%%%%%%%%%%%%%%%%%%%%%%%%%%%%%%%%%%%%%%%%%%%%%%%%%%
%adapted from Wang(2012)
%this program aligns the sections based on the deviation of the local
mass removed from each individual test versus the experimental trend
line deduced from multiple tests time
%input:
%gridded surface point cloud of all tests
%original surface point cloud of all tests
% experimental parameters (testing time, number of tests, concentration
of the bulk flowing fluid, etc..)
%output:
%deviation aligned point cloud

clear all
close all
clc
tic;

PipeR = 0.5;
PipeRCurve = 1.5;
upsPL = 8;
downsPL = 4;
BendL = 0.5*pi*PipeRCurve;
SD = 5;
Cw = 2.6; %saturated concentration of gypsum: 2.6g/l
GypDens = 1580; %density of gypsum: 1580 kg/m^3

```

```

% number of lines used for coordinate system correction
lines = 30;
%the code iterate max nIter times
nIter = 3;
barSlope = 0.0001;
barShift = 0.001;

%CalcOpt = input('1 for linear ; 2 for poly-fit method');
CalcOpt = 2;
%input of experimental parameters
%experimental time of all experiments
time = [0 30 60 80 100]/60;
conductivity = [0 0.19846951 0.38477311 0.49266551 0.58750991];
Cw_Cb = Cw - conductivity;
%Cw_CbCoef = polyfit(time,Cw_Cb,2);
Cw_CbCoef = [0.03819395 -0.41949312 2.6];
Cw_CbBestFit = polyval(Cw_CbCoef,time);
Cw_CbInt = polyint(Cw_CbCoef);
CwModT = polyval(Cw_CbInt,time);
pipeSec = 5; %number of individual sections of the pipe

%load gridded files of pipe surfaces for all tests, including unworn
load unwornGrid.txt
load test1Grid.txt
load test2Grid.txt
load test3Grid.txt
load test4Grid.txt

%read in original point cloud of all tests, including unworn to be
aligned
unwornOrg = dlmread('unwornOrg.txt');
test1Org = dlmread('test1Org.txt');
test2Org = dlmread('test2Org.txt');
test3Org = dlmread('test3Org.txt');
test4Org = dlmread('test4Org.txt');

mmOrg = [length(unwornOrg) length(test1Org) length(test2Org)
length(test3Org) length(test4Org)];

%evaluating number of grids in the circumferential and axial direction
mm=uint32(length(unwornGrid));
noCir = input('Enter the number of grids in the circumferential
direction: ');
noAxial = mm/noCir;
PipeR = 0.5;
PipeRCurve = 1.5;

[dummy,timeStep] = size(time);
%number of experimental tests

%setting the starts and ends line of region C
yStr = floor((noCir-lines)/2);
yEnd = yStr + lines;

```

```

theta = [unwornGrid(:,1), test1Grid(:,1), test2Grid(:,1),test3Grid(:,1),
test4Grid(:,1)]*(pi/180);
wear = [unwornGrid(:,3), test1Grid(:,3), test2Grid(:,3),test3Grid(:,3),
test4Grid(:,3)];
z = [unwornGrid(:,2), test1Grid(:,2), test2Grid(:,2),test3Grid(:,2),
test4Grid(:,2)];

CartXorg = zeros(max(mmOrg),timeStep);
cartYorg = zeros(max(mmOrg),timeStep);
cartZorg = zeros(max(mmOrg),timeStep);

CartXorg(1:mmOrg(1),1) = unwornOrg(:,1); CartXorg(1:mmOrg(2),2) =
test1Org(:,1);CartXorg(1:mmOrg(3),3) =
test2Org(:,1);CartXorg(1:mmOrg(4),4) =
test3Org(:,1);CartXorg(1:mmOrg(5),5) = test4Org(:,1);
cartYorg(1:mmOrg(1),1) = unwornOrg(:,2); cartYorg(1:mmOrg(2),2) =
test1Org(:,2);cartYorg(1:mmOrg(3),3) =
test2Org(:,2);cartYorg(1:mmOrg(4),4) =
test3Org(:,2);cartYorg(1:mmOrg(5),5) = test4Org(:,2);
cartZorg(1:mmOrg(1),1) = unwornOrg(:,3); cartZorg(1:mmOrg(2),2) =
test1Org(:,3);cartZorg(1:mmOrg(3),3) =
test2Org(:,3);cartZorg(1:mmOrg(4),4) =
test3Org(:,3);cartZorg(1:mmOrg(5),5) = test4Org(:,3);

thetaMatOrg = zeros(max(mmOrg),timeStep);
thetaMatOrg = -atan(cartYorg./CartXorg);

indOrg = find(thetaMatOrg<0);
thetaMatOrg(indOrg) = thetaMatOrg(indOrg)+pi; %update angle

delOrg = zeros(max(mmOrg),timeStep);
delOrg = sqrt(CartXorg.^2 + cartYorg.^2)-PipeR;

zupsPLorg = zeros(1,timeStep);
zBend1storg = zeros(1,timeStep);
zBend2ndorg = zeros(1,timeStep);
zSDorg = zeros(1,timeStep);

%evaluating number of data points in each individual section of the pipe
for j = 1:timeStep
    for i = 1:mmOrg(j)
        if cartZorg(i,j)> -upsPL
            zupsPLorg(j) = zupsPLorg(j)+1;
        end
        if cartZorg(i,j)<= -upsPL && cartZorg(i,j) > -(upsPL+BendL)
            zBend1storg(j) = zBend1storg(j) + 1;
        end
        if cartZorg(i,j)<= -(upsPL+BendL) && cartZorg(i,j) > -
(upsPL+BendL+SD)
            zSDorg(j) = zSDorg(j) + 1;
        end
        if cartZorg(i,j)<= -(upsPL+BendL+SD) && cartZorg(i,j) > -
(upsPL+2*BendL+SD)
            zBend2ndorg(j) = zBend2ndorg(j)+1;
        end
    end
end

```

```

        end
    end
end
zdownsPLorg = mmOrg-zupsPLorg-zBend1storg-zBend2ndorg-zSDorg;
pipeAxialOrg = [ones(1,pipeSec); zupsPLorg; zupsPLorg+zBend1storg;
zupsPLorg+zBend1storg+zSDorg; zupsPLorg+zBend1storg+zBend2ndorg+zSDorg;
mmOrg]

%reshape wear, theta and z vector to three dimensional matrix
for i = 1:timeStep
    wearMat(:, :, i) = reshape(wear(:, i), noCir, noAxial);
    thetaMat(:, :, i) = reshape(theta(:, i), noCir, noAxial);
    zMat(:, :, i) = reshape(z(:, i), noCir, noAxial);
end

%wear deviation from linera bestfit with modified time
for i= 1:noAxial
    for j = 1:noCir
        Dummy(1, :) = wearMat(j, i, :);
        coefWearTime = polyfit(CwModT, Dummy, 1);
        WearTimeFit(j, i, :) = polyval(coefWearTime, CwModT);
    end
end
WearTimeFitDev = wearMat-WearTimeFit;

zupsPL = 0;
zBend1st = 0;
zBend2nd = 0;
zSD = 0;
%evaluating number of axial grids in each individual section of the pipe
for i = 1:noAxial
    if zMat(1, i) > -upsPL
        zupsPL = zupsPL + 1;
    end
    if zMat(1, i) <= -upsPL && zMat(1, i) > -(upsPL+BendL)
        zBend1st = zBend1st + 1;
    end
    if zMat(1, i) <= -(upsPL+BendL) && zMat(1, i) > -(upsPL+BendL+SD)
        zSD = zSD + 1;
    end
    if zMat(1, i) <= -(upsPL+BendL+SD) && zMat(1, i) > -(upsPL+2*BendL+SD)
        zBend2nd = zBend2nd + 1;
    end
end
zdownsPL = noAxial-zupsPL-zBend1st-zBend2nd-zSD;
pipeAxial = [1 zupsPL zupsPL+zBend1st zupsPL+zBend1st+zSD
zupsPL+zBend1st+zBend2nd+zSD noAxial]

%Alignment of wear matrix based on deviation from the best fit line as a
function of modified time
for i = 1:pipeSec
    lineSlopex = barSlope + 0.001; %initiate angleRot Value
    lineShiftx = barShift + 0.001; %initiate shifting Value
    lineSlopey = barSlope + 0.001;
end

```

```

lineShifty = barSlope + 0.001;
counting = 0;
while ((counting < nIter) && ((max(abs(lineSlopex)) > barSlope) || (max(abs(lineShiftx)) > barShift))) | ((counting < nIter) && ((max(abs(lineSlopey)) > barSlope) || (max(abs(lineShifty)) > barShift))))
    counting = counting + 1;
    %calculation of shifting in x
    for k = 1:timeStep
        for n = pipeAxial(i):pipeAxial(i+1)
            sum = 0;
            for m = 1:lines
                sum = sum + (WearTimeFitDev(m,n,k) - WearTimeFitDev(noCir-m+1,n,k))/cos(thetaMat(m,n,k)); %COS 15 = - COS 165
                %Dummy variable for LocalShift
            end
            localShiftx(n,k) = sum/2/lines;
            %Average shift at each z location
        end
    end
    shiftCondX = localShiftx(pipeAxial(i):pipeAxial(i+1),:);
    zCond = zMat(1,pipeAxial(i):pipeAxial(i+1),1)';

    %calculate the slope of the correction by 1st order fit
    for k = 1:timeStep
        px(k,:) = polyfit(zCond, shiftCondX(:,k),1);
    end

    %keeping track of the slope and shift for each iteration
    bestfitX(:, :, counting) = px;

    for k = 1:timeStep
        lineSlopex(k) = px(k,1);
        lineShiftx(k) = px(k,2);
    end

    for k = 1:timeStep
        fitValx(:,k) = polyval(px(k,:),zCond); %calculating the value of shift (y = mx+b) at every z locations.
    end

    for k = 1:timeStep
        rs(:,pipeAxial(i):pipeAxial(i+1),k) = wearMat(:,pipeAxial(i):pipeAxial(i+1),k) + PipeR;
    end
    %Shift the points according to
    for k = 1:timeStep
        cartX(:,pipeAxial(i):pipeAxial(i+1),k) = rs(:,pipeAxial(i):pipeAxial(i+1),k).*cos(thetaMat(:,pipeAxial(i):pipeAxial(i+1),k))-zMat(:,pipeAxial(i):pipeAxial(i+1),k).*lineSlopex(k) - lineShiftx(k);
        cartY(:,pipeAxial(i):pipeAxial(i+1),k) = rs(:,pipeAxial(i):pipeAxial(i+1),k).*sin(thetaMat(:,pipeAxial(i):pipeAxial(i+1),k));
    end

```

```

        %translating cartesian coordinates to curvilinear
coordinates
        %zcurve = -(PipeRCurve - cartY).*sin(Phi);
        %zcurve_updated = zcurve.*(1 +
abs(sin(2*lineSlopex_bend1st*zcurve + lineSlopex_bend2nd)));
        %ycurve = -(PipeRCurve - cartY).*cos(Phi);
        %
        %Phi = atan(zcurve_updated./ycurve); %updating Phi
        %
        %R = sqrt(zcurve.^2 + ycurve.^2 + xcurve.^2);
        %cartZ = -Phi*PipeRCurve;
        %cartZ(:, :, k) = zMat(:, :, k);
        %
        %zCond = zMat(:, 1);
        %
        %transfer back to theta z and deviation matrix form
        thetaMat(:, pipeAxial(i):pipeAxial(i+1), k) = -
atan(cartY(:, pipeAxial(i):pipeAxial(i+1), k)./cartX(:, pipeAxial(i):pipeAxial(i+1), k));
        %
        %angle theta should be positive from 0
to 180
        ind = find(thetaMat<0);
        thetaMat(ind) = thetaMat(ind)+pi; %update angle
        %
        %zMat(:, :, k) = cartZ(:, :, k); %update
Z
        wearMat(:, pipeAxial(i):pipeAxial(i+1), k) =
sqrt(cartX(:, pipeAxial(i):pipeAxial(i+1), k).^2 +
cartY(:, pipeAxial(i):pipeAxial(i+1), k).^2) - PipeR; %update wear

        %alignment of original scanning data
        CartXorg(pipeAxialOrg(i, k):pipeAxialOrg(i+1, k), k) =
CartXorg(pipeAxialOrg(i, k):pipeAxialOrg(i+1, k), k) -
cartZorg(pipeAxialOrg(i, k):pipeAxialOrg(i+1, k), k).*lineSlopex(k) -
lineShiftx(k);
        cartYorg(pipeAxialOrg(i, k):pipeAxialOrg(i+1, k), k) =
cartYorg(pipeAxialOrg(i, k):pipeAxialOrg(i+1, k), k);

        thetaMatOrg(pipeAxialOrg(i, k):pipeAxialOrg(i+1, k), k) = -
atan(cartYorg(pipeAxialOrg(i, k):pipeAxialOrg(i+1, k), k)./CartXorg(pipeAxialOrg(i, k):pipeAxialOrg(i+1, k), k));

        indOrg = find(thetaMatOrg<0);
        thetaMatOrg(indOrg) = thetaMatOrg(indOrg)+pi; %update angle

        delOrg(pipeAxialOrg(i, k):pipeAxialOrg(i+1, k), k) =
sqrt(CartXorg(pipeAxialOrg(i, k):pipeAxialOrg(i+1, k), k).^2 +
cartYorg(pipeAxialOrg(i, k):pipeAxialOrg(i+1, k), k).^2)-PipeR; %update
wear
    end

    for k = 1:timeStep
        figure(k)
    end

```

```

        subplot(5,2,1)
        plot(-
zCond,localShiftx(pipeAxial(i):pipeAxial(i+1),k),'r',-
zCond,fitValx(:,k),'b')
        title('Shift in X direction')
        xlabel('Z/D down stream')
        ylabel('Wear/D')
        set(gcf,'color','white')
    end

    %calculation of shifting in y
    for k = 1:timeStep
        for n = pipeAxial(i):pipeAxial(i+1)
            sum = 0;
            for m = yStr:yEnd
                sum = sum +
(WearTimeFitDev(m,n,k)/sin(thetaMat(m,n,k)));
            end
            localShifty(n,k) = sum/lines;
        end
    end
    shiftCondY = localShifty(pipeAxial(i):pipeAxial(i+1),:);
    zCond = zMat(1,pipeAxial(i):pipeAxial(i+1),1)';
    %calculate the slope of the correction by 1st order fit
    for k = 1:timeStep
        py(k,:) = polyfit(zCond, shiftCondY(:,k),1);
    end
    bestfitY(:,:,counting) = py;
    for k = 1:timeStep
        lineSlopey(k) = py(k,1);
        lineShifty(k) = py(k,2);
    end
    for k = 1:timeStep
        fitValy(:,k) = polyval(py(k,:),zCond);
    end
    %Shift the points according to
    for k = 1:timeStep
        rs(:,pipeAxial(i):pipeAxial(i+1),k) =
wearMat(:,pipeAxial(i):pipeAxial(i+1),k) + PipeR;
    end

    for k = 1:timeStep
        cartX(:,pipeAxial(i):pipeAxial(i+1),k) =
rs(:,pipeAxial(i):pipeAxial(i+1),k).*cos(thetaMat(:,pipeAxial(i):pipeAxial(i+1),k));
        cartY(:,pipeAxial(i):pipeAxial(i+1),k) =
(rs(:,pipeAxial(i):pipeAxial(i+1),k).*sin(thetaMat(:,pipeAxial(i):pipeAxial(i+1),k))-
zMat(:,pipeAxial(i):pipeAxial(i+1),k).*lineSlopey(k) -
lineShifty(k));

    %translating cartesian coordinates to curvilinear
coordinates
    %zcurve = -(PipeRCurve - cartY).*sin(Phi);

```

```

        %zcurve_updated = zcurve.*(1 +
abs(sin(2*lineSlopey_bend1st*zcurve + lineSlopey_bend2nd)));
        %ycurve = -(PipeRCurve - cartY).*cos(Phi);
        %Phi = atan(zcurve_updated./ycurve);
        %
        %R = sqrt(zcurve.^2 + ycurve.^2 + xcurve.^2);
        %cartZ = -Phi*PipeRCurve;
        %cartZ(:, :, k) = zMat(:, :, k);
        %approximately cartZ = zMat
        %
        %zCond = zMat(:, 1);
        %
        %transfer back to theta z and deviation matrix form
        thetaMat(:, pipeAxial(i):pipeAxial(i+1), k) = -
atan(cartY(:, pipeAxial(i):pipeAxial(i+1), k)./cartX(:, pipeAxial(i):pipeAxial(i+1), k));
        %
        %angle theta should be always positive
from 0 to 180
        ind = find(thetaMat<0);
        thetaMat(ind) = thetaMat(ind)+pi; %angle updated
        %
        %zMat(:, :, k) = cartZ(:, :, k);
%z location updated
        wearMat(:, pipeAxial(i):pipeAxial(i+1), k) =
sqrt(cartX(:, pipeAxial(i):pipeAxial(i+1), k).^2 +
cartY(:, pipeAxial(i):pipeAxial(i+1), k).^2) - PipeR; %wear
updated

        %alignment of original scanning data
        CartXorg(pipeAxialOrg(i, k):pipeAxialOrg(i+1, k), k) =
CartXorg(pipeAxialOrg(i, k):pipeAxialOrg(i+1, k), k);
        cartYorg(pipeAxialOrg(i, k):pipeAxialOrg(i+1, k), k) = -(-
cartYorg(pipeAxialOrg(i, k):pipeAxialOrg(i+1, k), k) -
cartZorg(pipeAxialOrg(i, k):pipeAxialOrg(i+1, k), k).*lineSlopey(k) -
lineShifty(k));
        thetaMatOrg(pipeAxialOrg(i, k):pipeAxialOrg(i+1, k), k) = -
atan(cartYorg(pipeAxialOrg(i, k):pipeAxialOrg(i+1, k), k)./CartXorg(pipeAxialOrg(i, k):pipeAxialOrg(i+1, k), k));

        indOrg = find(thetaMatOrg<0);
        thetaMatOrg(indOrg) = thetaMatOrg(indOrg)+pi; %update angle
        delOrg(pipeAxialOrg(i, k):pipeAxialOrg(i+1, k), k) =
sqrt(CartXorg(pipeAxialOrg(i, k):pipeAxialOrg(i+1, k), k).^2 +
cartYorg(pipeAxialOrg(i, k):pipeAxialOrg(i+1, k), k).^2) - PipeR; %update
wear

    end

    for k = 1:timeStep
        figure(k)
        subplot(5, 2, 2)
        plot(-
zCond, localShifty(pipeAxial(i):pipeAxial(i+1), k), 'r', -
zCond, fitValy(:, k), 'b')

```

```

        title('Shift in Y direction')
        xlabel('Z/D down stream')
        ylabel('Wear/D')
    end

    %Updating the best fit wear
    for l = pipeAxial(i):pipeAxial(i+1)
        for j = 1:noCir
            Dummy(1,:) = wearMat(j,l,:);
            coefWearTime = polyfit(CwModT,Dummy, 1);
            WearTimeFit(j,l,:) = polyval(coefWearTime,CwModT);
        end
    end
    end
    WearTimeFitDev = wearMat-WearTimeFit; %updating wear deviation
from best fit

    end

    for k = 1:timeStep
        Dummy = wearMat(:, :, k);
        wear(:, k) = Dummy(1:noAxial*noCir);
    end
end
end

dlmwrite('unworn_devaligned.txt',
[thetaMatOrg(1:mmOrg(1),1)*180/pi, cartZorg(1:mmOrg(1),1), delOrg(1:mmOrg(
1),1)], 'delimiter', '\t', 'newLine', 'pc');
dlmwrite('test1_devaligned.txt',
[thetaMatOrg(1:mmOrg(2),2)*180/pi, cartZorg(1:mmOrg(2),2), delOrg(1:mmOrg(
2),2)], 'delimiter', '\t', 'newLine', 'pc');
dlmwrite('test2_devaligned.txt',
[thetaMatOrg(1:mmOrg(3),3)*180/pi, cartZorg(1:mmOrg(3),3), delOrg(1:mmOrg(
3),3)], 'delimiter', '\t', 'newLine', 'pc');
dlmwrite('test3_devaligned.txt',
[thetaMatOrg(1:mmOrg(4),4)*180/pi, cartZorg(1:mmOrg(4),4), delOrg(1:mmOrg(
4),4)], 'delimiter', '\t', 'newLine', 'pc');
dlmwrite('test4_devaligned.txt',
[thetaMatOrg(1:mmOrg(5),5)*180/pi, cartZorg(1:mmOrg(5),5), delOrg(1:mmOrg(
5),5)], 'delimiter', '\t', 'newLine', 'pc');
toc

%%%%%%%%%%%%%%%%%%%%%%%%%%%%%%%%%%%%%%%%%%%%%%%%%%%%%%%%%%%%%%%%%%%%%%%%SHERWOOD NUMBER%%%%%%%%%%%%%%%%%%%%%%%%%%%%%%%%%%%%%%%%%%%%%%%%%%%%%%%%%%%%%%%%%%%%%%%%
%this program evaluate the mass transfer coefficient, mass removed and
the Sherwood number
%input:
%aligned gridded pipe surface point cloud
%experimental parameters (testing time, number of tests, concentration
of the bulk flowing fluid, etc..)
%output:
%local and total mass removed
%local mass transfer coefficient
%local Sherwood number

clear all

```

```

close all
clc

tic;
%input of experimental parameters
Cw = 2.6;           %saturated concentration of gypsum: 2.6g/l
GypDens = 1580;    %density of gypsum: 1580 kg/m^3
time = [0 30 60 80 100]/60;
conductivity = [0 0.19846951 0.38477311 0.49266551 0.58750991];
Cw_Cb = Cw - conductivity;
%Cw_CbCoef = polyfit(time,Cw_Cb,2);
Cw_CbCoef = [0.03819395 -0.41949312 2.6];
Cw_CbBestFit = polyval(Cw_CbCoef,time);
Cw_CbInt = polyint(Cw_CbCoef);
%calculation of modified time
CwModT = polyval(Cw_CbInt,time);

%CalcOpt= input('1 for linear ; 2 for poly-fit method');
CalcOpt = 2;
pOrder = 2;
%read in aligned gridded pipe surface point cloud
load unworn.txt
load test1.txt
load test2.txt
load test3.txt
load test4.txt

%Enter the total length of the input file
mm=uint32(length(test2));
noCir = input('Enter the number of angle subdivisions: ');
noAxial = mm/noCir;
PipeR = 0.5;
PipeRCur = 1.5;

[dummy,timeStep] = size(time);
%calculate number of experimental test

theta      =      [unworn(:,1),      test1(:,1),      test2(:,1),test3(:,1),
test4(:,1)]*(pi/180);
wear = [unworn(:,3), test1(:,3), test2(:,3),test3(:,3), test4(:,3)];
z = [unworn(:,2), test1(:,2), test2(:,2),test3(:,2), test4(:,2)];
%converting theta, wear and z to matrix of noCir rows and noAxial
columns
for i = 1:timeStep
    wearMat(:, :, i) = reshape(wear(:, i), noCir, noAxial);
    thetaMat(:, :, i) = reshape(theta(:, i), noCir, noAxial);
    zMat(:, :, i) = reshape(z(:, i), noCir, noAxial);
end

%evaluating number of axial grids in each section, upstream pipe, first
elbow, separation pipe, second elbow and downstream pipe
upsPL = 8;
downsPL = 4;
BendL = PipeRCur*pi*0.5;

```

```

SD = 5;

zupsPL = 0;
zBend1st = 0;
zBend2nd = 0;
zSD = 0;
for i = 1:noAxial
    if zMat(1,i) > -upsPL
        zupsPL = zupsPL+1;
    end
    if zMat(1,i) <= -upsPL && zMat(1,i) > -(upsPL+BendL)
        zBend1st = zBend1st+1;
    end
    if zMat(1,i) <= -(upsPL+BendL) && zMat(1,i) > -(upsPL+BendL+SD)
        zSD = zSD+1;
    end
    if zMat(1,i) <= -(upsPL+BendL+SD) && zMat(1,i) > -(upsPL+2*BendL+SD)
        zBend2nd = zBend2nd+1;
    end
end
end
zdownsPL = noAxial-zupsPL-zBend1st-zBend2nd-zSD;

%calculation of local mass removed within each grid cell
dt = (thetaMat(2,1) - thetaMat(1,1))/2; %change in theta (radians)
deltaz = -zMat(1,2) - -zMat(1,1); %change in z at the
centerline

%mass transfer of the 8" upstream straight section
for k = 1:timeStep
    for j = 1:zupsPL
        for i = 1:noCir
            volume_cell(i,j,k) =
deltaz*wearMat(i,j,k)*(2*PipeR+wearMat(i,j,k))/2*(dt*2);
            mass_cell(i,j,k) = GypDens*volume_cell(i,j,k)*0.0254^3;

            areaInstant(i,j,k) =
deltaz*(PipeR+wearMat(i,j,k))*(dt*2)*0.0254^2;
        end
    end
end

%volume_cell calculated as a double integral!
for k = 1:timeStep
    for j = zupsPL+1:zupsPL+zBend1st
        for i = 1:noCir
            polarfun = @(theta,r)r*deltaz*(1+r*sin(theta)/PipeRCur);
            volume_cell(i,j,k) = dblquad(polarfun,thetaMat(i,j,k)-
dt,thetaMat(i,j,k)+dt,PipeR,PipeR+wearMat(i,j,k));
            mass_cell(i,j,k) = GypDens*volume_cell(i,j,k)*0.0254^3;

            F =
@(theta)deltaz*(PipeR+wearMat(i,j,k))*(1+(PipeR+wearMat(i,j,k))*sin(thet
a)/PipeRCur);

```

```

        area_cell(i,j,k) = quad(F,thetaMat(i,j,k)-
dt,thetaMat(i,j,k)+dt); %instantaneous
area calculation
        areaInstant(i,j,k) = area_cell(i,j,k)*0.0254^2;
    end
end
end

%mass removed of the separation pipe
for k = 1:timeStep
    for j = zupsPL+zBend1st+1:zupsPL+zBend1st+zSD
        for i = 1:noCir
            volume_cell(i,j,k) =
deltaz*wearMat(i,j,k)*(2*PipeR+wearMat(i,j,k))/2*(dt^2);
            mass_cell(i,j,k) = GypDens*volume_cell(i,j,k)*0.0254^3;

            areaInstant(i,j,k) =
deltaz*(PipeR+wearMat(i,j,k))*(dt^2)*0.0254^2;
        end
    end
end

%mass removed of the 2nd bend section
for k = 1:timeStep
    for j = zupsPL+zBend1st+zSD+1:zupsPL+zBend1st+zSD+zBend2nd
        for i = 1:noCir
            polarfun = @(theta,r)r*deltaz*(1+r*sin(theta)/PipeRCur);
            volume_cell(i,j,k) = dblquad(polarfun,thetaMat(i,j,k)+pi/2-
dt,thetaMat(i,j,k)+pi/2+dt,PipeR,PipeR+wearMat(i,j,k));
            mass_cell(i,j,k) = GypDens*volume_cell(i,j,k)*0.0254^3;

            F =
@(theta)deltaz*(PipeR+wearMat(i,j,k))*(1+(PipeR+wearMat(i,j,k))*sin(thet
a)/PipeRCur);
            area_cell(i,j,k) = quad(F,thetaMat(i,j,k)+pi/2-
dt,thetaMat(i,j,k)+pi/2+dt);
            areaInstant(i,j,k) = area_cell(i,j,k)*0.0254^2;
        end
    end
end

%mass transfer of the 4" downstream straight pipe
for k = 1:timeStep
    for j = zupsPL+zBend1st+zSD+zBend2nd+1:noAxial
        for i = 1:noCir
            volume_cell(i,j,k) =
deltaz*wearMat(i,j,k)*(2*PipeR+wearMat(i,j,k))/2*(dt^2);
            mass_cell(i,j,k) = GypDens*volume_cell(i,j,k)*0.0254^3;

            areaInstant(i,j,k) =
deltaz*(PipeR+wearMat(i,j,k))*(dt^2)*0.0254^2;
        end
    end
end
end

```

```

%reshaping mass and area matrix to vector form
for j = 1:timeStep
    MRem(:,j) = reshape(mass_cell(:, :, j), noCir*noAxial, 1);
    area(:,j) = reshape(areaInstant(:, :, j), noAxial*noCir, 1);
    areaCw_Cb(:,j) = area(:,j) * (Cw - conductivity(j));
    rhowear(:,j) =
    reshape(wearMat(:, :, j)*GypDens*0.0254, noAxial*noCir, 1);
end

timegap = ones(1, timeStep-1);
timeAve = ones(1, timeStep-1);
for i = 1:timeStep-1
    timegap(i) = (time(i+1) - time(i));
    %time interval between two time steps (in hour)

    timeAve(i) = (time(i)+time(i+1))/2;
    %averaged time between every two subsequent test, where mass
transfer rates are to be evaluated (in hr)
    condAve(i) = (conductivity(i) + conductivity(i+1))/2;
    areaAve(:,i) = (area(:,i) + area(:,i+1))/2;
end

%transfer the deviation matrix from row vectors to column vectors
theta = unworn(:,1);
Z = unworn(:,2);

%evaluating the mass transfer coefficient based on linear fit of
modified
%time and mass removed
if CalcOpt < 1.5
    %Using two point (finite difference) method
    for n = 1: timeStep-1
        MRR(:,n) = (MRem(:,n+1)-MRem(:,n))/(timegap(n));
        %Mass removal rate (kg/hr) calculated by two points
        %CBulk is the averaged bulk concentration between two time steps
        CBulk = condAve(n); %60 mins/hr

        %areaAve is the average area between two time steps
        MTC(:,n) = MRR(:,n)./(areaAve(:,n)*(Cw - CBulk));
        %mass transfer coefficient in m/hour
    end

    for i = 1:mm
        coefMassTran(i,:) = polyfit(time, MRem(i,:), CalcOpt);
        MRem_bestfit(i,:) = polyval(coefMassTran(i,:),time);
    end

    %calculating the deviation of the local wears from the average best
fit line in inches
    for i = 1:timeStep
        wear_ave(:,i) = mean(reshape(wear(:,i), noCir, noAxial));
    end
    for i = 1:noAxial

```

```

        coefwear_ave(i,:) = polyfit(time,wear_ave(i,:),CalcOpt);
        wear_ave_bestfit(i,:) = polyval(coefwear_ave(i,:),time);
    end
    for i = 1:timeStep
        for j = 1:noAxial
            wear_dummy(:, :, i) = reshape(wear(:, i), noCir, noAxial)';
            wear_ave_dev(j, :, i) = wear_dummy(j, :, i)
        wear_ave_bestfit(j, i);
        end
    end
    wearave_dev = zeros(mm,timeStep);
    for i = 1:timeStep
        wearave_dev(:, i) = reshape(wear_ave_dev(:, :, i)', mm, 1);
    end

else
    coefMassTran = zeros(mm, pOrder+1);
    %Coefficients of the 3rd order best fit curve of mass VS time

    coefMassRate = zeros(mm, pOrder);
    %derivative of the 3rd order polynomial curve

    %coefMassRate and radius
    for i = 1:mm
        coefMassTran(i,:) = polyfit(time, MRem(i,:), pOrder);
        coefMassRate(i,:) = polyder(coefMassTran(i,:));
        MRR(i,:) = polyval(coefMassRate(i,:), time);
        MRem_bestfit(i,:) = polyval(coefMassTran(i,:),time);

        MassPerArea(i,:) = MRem(i,:)./area(i,:);
        %MassPerAreaCoef(i,:) = polyfit(CwModT,MassPerArea(i,:),1);
        MassPerAreaCoef(i,:) = polyfit(CwModT,rhowear(i,:),1);
        MassPerAreaRate(i,:) = polyder(MassPerAreaCoef(i,:));

        %bestfit of MRR and Area(Cw-Cb)
        coefMTC(i,:) = polyfit(Cw_Cb,MRR(i,:)./area(i,:),1);
        MRate(i,:) = polyder(coefMTC(i,:));
    end

    for n = 1 : timeStep

        %CBulk is the averaged bulk concentration between two time steps
        CBulk = conductivity(n);

        %MTC mass transfer coefficient (hm) in m/hr
        MTC(:, n) = MRR(:, n)./(area(:, n)*(Cw - CBulk));
        MTC(:, n) = MassPerAreaRate(:, 1);
        %MTC(:, n) = MRate(:, 1);
    end

    %calculating the deviation of the local wears from the average best
    fit line in inches
    for i = 1:timeStep
        wear_ave(:, i) = mean(reshape(wear(:, i), noCir, noAxial));

```

```

end
for i = 1:noAxial
    coefwear_ave(i,:) = polyfit(time,wear_ave(i,:),pOrder);
    wear_ave_bestfit(i,:) = polyval(coefwear_ave(i,:),time);
end
for i = 1:timeStep
    for j = 1:noAxial
        wear_dummy(:, :, i) = reshape(wear(:, i), noCir, noAxial)';
        wear_ave_dev(j, :, i) = wear_dummy(j, :, i) -
wear_ave_bestfit(j, i);
    end
end
wearave_dev = zeros(mm,timeStep);
for i = 1:timeStep
    wearave_dev(:, i) = reshape(wear_ave_dev(:, :, i)', mm, 1);
end

end

wear_dev = (MRem - MRem_bestfit)/GypDens/0.0254;
%deviation of the local mass removed from the best fit line in inches.

LocalSh = MTC*0.0254/6.49e-10/3600;
%Local Sherwood number

LocMRem = [theta, Z, MRem];
%Local mass removal per area

LocMRRMat = [theta, Z, MRR];
%Local Mass transfer rates(timeSteps -1)calculated by the wears of two
adjacent time steps

LocMTCMat = [theta, Z, MTC];
%local mass transfer coefficient

LocShMat = [theta, Z, LocalSh];
%theta, z and Local Sherwood numbers

LocWear_dev = [theta, Z, wear_dev];
%deviation of wears from the best fit line

LocWearave_dev = [theta, Z, wearave_dev];
%deviation of the local wear from the average best fit line

LocArea = [theta, Z, area];
%Local instantaneous area

LocAreaCw_Cb = [theta, Z, areaCw_Cb];
%Local instantaneous area*(Cw - Cb)

dlmwrite('LocArea.txt', LocArea, 'delimiter', '\t', 'newLine', 'pc');
dlmwrite('LocAreaCw_Cb.txt', LocAreaCw_Cb, 'delimiter', '\t', 'newLine',
'pc');
dlmwrite('time.txt', time, 'delimiter', '\t', 'newLine', 'pc');

```

```
dlmwrite('Cw_Cb.txt', Cw_Cb, 'delimiter', '\t', 'newLine', 'pc');
dlmwrite('CwModT.txt', CwModT, 'delimiter', '\t', 'newLine', 'pc');
dlmwrite('LocMRem.txt', LocMRem, 'delimiter', '\t', 'newLine', 'pc');
dlmwrite('LocMRR.txt', LocMRRMat, 'delimiter', '\t', 'newLine', 'pc');
dlmwrite('LocMTC.txt', LocMTCMat, 'delimiter', '\t', 'newLine', 'pc');
dlmwrite('LocSh.txt', LocShMat, 'delimiter', '\t', 'newLine', 'pc');
dlmwrite('LocWear_dev.txt', LocWear_dev, 'delimiter', '\t', 'newLine',
'pc');
dlmwrite('LocWearave_dev.txt', LocWearave_dev, 'delimiter', '\t',
'newLine', 'pc');
toc
```